MAGNETO-OPTIC AND INTEGRATED SI_3N_4 PHOTONIC DEVICES FOR C-BAND AND MID-IR APPLICATIONS

by

Shelbi Lyn Jenkins

Copyright © Shelbi Lyn Jenkins 2021

A Dissertation Submitted to the Faculty of the

JAMES C. WYANT COLLEGE OF OPTICAL SCIENCES

In Partial Fulfillment of the Requirements
For the Degree of

DOCTOR OF PHILOSOPHY
WITH A MAJOR IN OPTICAL SCIENCES

In the Graduate College

THE UNIVERSITY OF ARIZONA

2021

THE UNIVERSITY OF ARIZONA
GRADUATE COLLEGE

As members of the Dissertation Committee, we certify that we have read the dissertation prepared by **Shelbi Lyn Jenkins**, titled ***Magneto-optic and Integrated Si3N4 Photonic Devices for C-band and Mid-IR Applications*** and recommend that it be accepted as fulfilling the dissertation requirement for the Degree of Doctor of Philosophy.

Professor Robert A. Norwood Date: 7/26/2021

Professor Masud Mansuripur Date: 7/26/2021

Professor Lloyd L. LaComb, Jr. Date: 7/26/2021

Final approval and acceptance of this dissertation is contingent upon the candidate's submission of the final copies of the dissertation to the Graduate College.

I hereby certify that I have read this dissertation prepared under my direction and recommend that it be accepted as fulfilling the dissertation requirement.

Professor Robert A. Norwood Date: 7/26/2021
Dissertation Committee Chair
Wyant College of Optical Sciences

ACKNOWLEDGEMENTS

I would like to begin by acknowledging the O'odham Jewe, Tohono O'odham, Yaqui, Sobaipuri and Hohokam people on whose land this university was built and all of this research took place. I am here to acknowledge the actions of the past that harmed and displaced the peoples who stewarded this land from time immemorial. I would like my readers to reflect on how we can move forward in the spirit of support and reconciliation and how we may encourage the sovereignty of these peoples to inhabit, cultivate and connect with this land again.

I'd like to thank my committee members Dr. Masud Mansuripur and Dr. Lloyd LaComb for their support and encouragement in writing and defending my dissertation, and for making the whole process seem manageable. I'd especially like to thank my advisor, Dr. Bob Norwood, for always being supportive, for encouraging me to try new things, for allowing me to make mistakes and my own decisions, and for teaching me that part of being self-sufficient is asking for help when I need it.

I am ever grateful to the staff and students who helped me gain the expertise that I have now. This includes, but is certainly not limited to, Abhinav Nishant, Julie Frish, Spencer Ketchum, Roland Himmelhuber, Kerry Nierenberg, Lindsey Holeman, Kyungjo Kim and Stephanie Arouh.

I'd like to thank my Mom and my siblings for the love and support they have given me throughout my PhD, and through the many meandering paths that led me here. Thank you for being there with me in all walks of my life, even when I wasn't nearly as fun and cool as I am now.

I must state without a doubt that I could not have made it through this experience without the love, encouragement and strength of my pals. Every friendship I've made was a light that brought me warmth and comfort at times when nothing else could. For those who were there when I needed a hug, a rant, a coffee or a beer - those moments mean the world to me, and I hold them much more dearly than I do my new prefix.

Finally, I'd like to give my most special thank you to Sasaan Showghi: for every idea that you shared with me, every solution you gave, and the expertise you lent, for showing me what it means to be driven, optimistic and persistent in the face hardship, for encouraging me and challenging me every day, and for all the help that you knew I needed, whether I had asked for it or not.

DEDICATION

To the family that I chose, and the family that chose me.

TABLE OF CONTENTS

TABLE OF CONTENTS – *Continued*

LIST OF FIGURES

LIST OF FIGURES – *Continued*

LIST OF FIGURES – *Continued*

LIST OF TABLES

ABSTRACT

This dissertation demonstrates Si_3N_4 device designs, resonator tuning techniques and polymer integration for various photonic applications in the C-band and mid-wave infrared (MWIR) regime.

Active integrated silicon photonic devices have been instrumental the advancement of data processing and communications for decades. Fabricating active photonic devices is costly and often involves complex processing methods. We demonstrate the ability to use an external 487 nm laser source to opto-thermally tune passive photonic devices. We explored various methods of tuning these devices using our short-visible wavelength source with tuning capabilities up to 24.4 pm/mW for a passive Si_3N_4 microring resonators with SiO_2 cladding. By removing the cladding material using standard reactive ion etching techniques, we demonstrated an increase in thermal isolation that increased our tuning capabilities to 44.4 pm/mW. With these methods we successfully demonstrated the ability to tune the resonance of microresonators without integrating electrical contacts or by implementing a thermal stage. These methods provide potential alternatives to conventional thermal tuning techniques, especially for quality control in high volume manufacturing.

The use of magneto-optics (MO) in Faraday rotators and other devices has been essential for the use and advancement of photonic devices and systems. The low Verdet constants and structural rigidity of current MO materials limit the potential for advancement in the field through on-chip MO device fabrication. To overcome this, we have synthesized high-Verdet MO polymer materials to integrate with silicon photonic devices; these materials were developed in the Pyun group in the Department of Chemistry/Biochemistry. By integrating these materials with high-Q Si_3N_4 resonators we have successfully shown a preliminary proof-of-concept for a

functional magneto-optic modulator. This initial design integrated polymer-coated magnetic cobalt nanoparticles as the cladding material with a Si_3N_4 resonator with a Q factor of 2.2 million. By applying an external magnetic field of 10 mT to the device, we demonstrated extinction ratios up to 4.75 dB for the on-resonance wavelength position. These results show the potential for creating on-chip magneto-optic devices that can be used as modulators for telecommunications or as sensors for environmental or biomedical applications.

By designing Si_3N_4 waveguides that can operate at both 1.55 μm and 4.6 μm we have demonstrated the possibility of fabricating dual-purpose photonic devices for sensing and communication systems. We have designed, simulated and experimentally measured a triple core Si_3N_4 waveguide that guides a supermode at 4.6 μm as well as single modes at 1.55 μm. The insertion losses for these waveguides are as low as -6.70 dB and -7.04 dB for 4.6 μm and 1.55 μm respectively. This design compares favorably to standard single core Si_3N_4 waveguides which have insertion losses of -9.89 dB at 4.6 μm and -4.94 dB at 1.55 μm. These results show that by creating multi-core waveguides we can successfully guide MWIR modes with low loss as compared to current waveguide designs. The ability to fabricate these devices using standard fabrications techniques demonstrates promise in creating dual-purpose photonic devices for multi-wavelength applications.

This dissertation demonstrates advancement in integrated photonics for use in data communications and processing, as well organic gas and magnetic field sensing. They offer simple, efficient and low-cost alternatives to existing options and surpass barriers to further improvement and developments in the expanding field of silicon photonics.

CHAPTER 1

Introduction and motivations

The field of integrated silicon photonics has been instrumental in enabling the ever increasing demands for high speed data communications and storage. Estimates show that internet traffic is expected to reach nearly 400 exabytes per month by the year 2022 - more than double the amount we saw in 2020.[1,2,3] The low fabrication costs, high performance of electro-optical integration and compatibility with CMOS technology are what make silicon photonics the leading candidate for advancements in optical interconnect technology.[4,5] The recent strides in the field have contributed to improvements in the telecommunication sector in addition to sensing applications such as environmental, biomedical and Lidar systems.[6,7]

A key subset of the field of silicon photonics is the emergence of commercial Si_3N_4 devices. These devices are an attractive candidate for photonic innovation because they are low loss, CMOS compatible, are able to transmit high power signals, and they are instrumental in many of the recent advancements in quantum computation and networking due to their nonlinear optical effects.[8,9,10]

In addition to telecommunications, the development and optimization of Si_3N_4 integrated devices enables to various other applications such as environmental sensing.[11] The ability to fabricate Mid-IR compatible photonic devices from large-scale fabrication techniques and materials broadens the potential to create low-cost and high-performance environmental sensors that can register the spectral characteristics of volatile organic compounds.[12] Our ability to fabricate, characterize and optimize these devices is crucial for meeting the current demands of these fields and any other potential emerging applications.

Another limiting factor in the adoption of photonic devices is the lack of low-cost and fabrication-compatible materials.[13,14] The development of optical polymers offers a low-cost alternative to current device designs and systems. Novel optical polymers can be easily integrated with silicon photonics devices for sensing and data communication systems.[15,16] In particular, magneto-optic polymer materials are a focus of many research groups due to the potential to replace the common use expensive garnet crystals with limited integration capabilities. Polymer-integrated devices are prime candidates for advancing the implementation of high-speed magneto-optic modulators that operate with low power consumption and have the potential to operate at cryogenic and room temperatures.[17]

CHAPTER 2

Waveguides and optical resonators: theory and fundamentals

In order to comprehend the mechanisms and performance of the devices and designs discussed in this work, one must first understand the theory behind the functionality and operation of optical waveguides and resonant microstructures. This chapter examines these concepts at length.

2.1 Waveguides

Waveguides are physical structures that are used to guide and direct light waves with minimal energy loss. These devices can be made of, but are not limited to: glass, semiconductors, polymers, crystals or conducting materials. In this section we will discuss the mechanisms behind waveguides, their relevant parameters, geometries and practical limitations due to loss and fabrication processes. This section will address 2D planar waveguides, but the concepts can be extended further to include more complex 3D designs using the Marcatili or the Effective Index Method.[18]

2.1.1 Ray theory and total internal reflection

When light is incident onto a surface, the light may either be partially reflected from the surface and partially transmitted into the material, or it can be totally reflected from the surface. To determine the angle of refection into a medium, we use Snell's Law:

$$n_1 sin\theta_1 = n_2 sin\theta_2. \tag{2.1}$$

Snell's law relates the refractive indices (RI) of the two media (n_1 and n_2) as well as the incident and transmitted angles (θ_1 and θ_2) relative to the surface normal. When $n_2 > n_1$ there exists an angle such that the refracted angle is 90^o. Any angle above this reduces Snell's law to

$$sin\theta_c = \frac{n_2}{n_1}, \tag{2.2}$$

where no light will be transmitted into the medium and all light will be reflected from the surface. This condition is known as the critical angle.[19]

When we consider a layered structure where the indices of the top and bottom layer are both less than the index of the middle layer, then for incidence angles above the critical angles for both interfaces the light will be repeatedly totally internally reflected and the light will be guided between the two layers. This concept is demonstrated below in Figure 2.1.[19]

There exists a cone of light where if the incident light to a waveguide is within this cone it will be guided by the waveguide.[19,20] This is referred to as the numerical aperture and is defined as

$$NA = n_1 sin\theta_c. \tag{2.3}$$

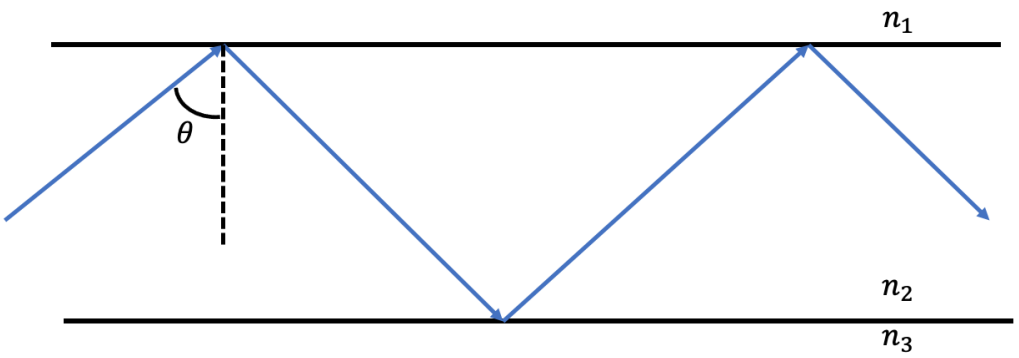

Figure 2.1: TIR within a planar waveguide.

2.1.2 Reflection coefficients

When light is incident on a an interface of two dielectric media of indices n_1 and n_2 with and incident angle of θ_1, part of the light is reflected off the interface at the same angle θ_1 and a portion of the light is transmitted into the second medium at an angle of θ_2. The complex amplitudes of the incident, reflected and transmitted beams are illustrated in Figure 2.2. The relationship between the incident and reflected beams is denoted by

$$E_r = rE_i, \tag{2.4}$$

where r is the wavelength-dependent complex reflection coefficient. The reflection coefficient is dependent both on the incident angle of the light, as well its polarization state.[19] The polarization state is determined by the electric field vector of the electromagnetic wave. When the electric field is perpendicular to the plane of incidence, then the light is said to have TE (transverse electric) polarization. Alternatively, when the magnetic field is perpendicular to the plane of incidence, the light is said to have TM (transverse magnetic) polarization.[19] The Fresnel reflections

coefficients for these two polarization states are expressed as

$$r_{TE} = \frac{n_1 cos\theta_1 - n_2 cos\theta_2}{n_1 cos\theta_1 + n_2 cos\theta_2} \tag{2.5}$$

$$r_{TM} = \frac{n_2 cos\theta_1 - n_1 cos\theta_2}{n_2 cos\theta_1 + n_2 cos\theta_2}. \tag{2.6}$$

By using Snell's Law (2.1), we can rewrite these two equations as

$$r_{TE} = \frac{n_1 cos\theta_1 - \sqrt{n_2^2 - n_1^2 cos\theta_1}}{n_1 cos\theta_1 + \sqrt{n_2^2 - n_1^2 cos\theta_2}} \tag{2.7}$$

$$r_{TM} = \frac{n_2^2 cos\theta_1 - n_1\sqrt{n_2^2 - n_1^2 cos\theta_1}}{n_2^2 cos\theta_1 + n_1\sqrt{n_2^2 - n_1^2 cos\theta_2}}. \tag{2.8}$$

When considering incident angles where $\theta_1 \leq \theta_c$, only part of the incoming ray is reflected, and the reflection coefficients is real. However, when the incident angle exceeds the critical angle (when $\theta_1 > \theta_c$), the value within the square root in (2.7) and (2.8) becomes negative, making the reflection coefficient complex with an imposed phase shift on the reflected wave.[19] These phase shifts for the two polarizations are given by

$$\phi_{TE} = 2tan^{-1}[\sqrt{sin^2\theta_1 - (n_2/n_1)^2}/cos\theta_1] \tag{2.9}$$

$$\phi_{TM} = 2tan^{-1}[\sqrt{(n_2/n_1)^2 sin^2\theta_1 - 1}/(n_2/n_1)cos\theta_1]. \tag{2.10}$$

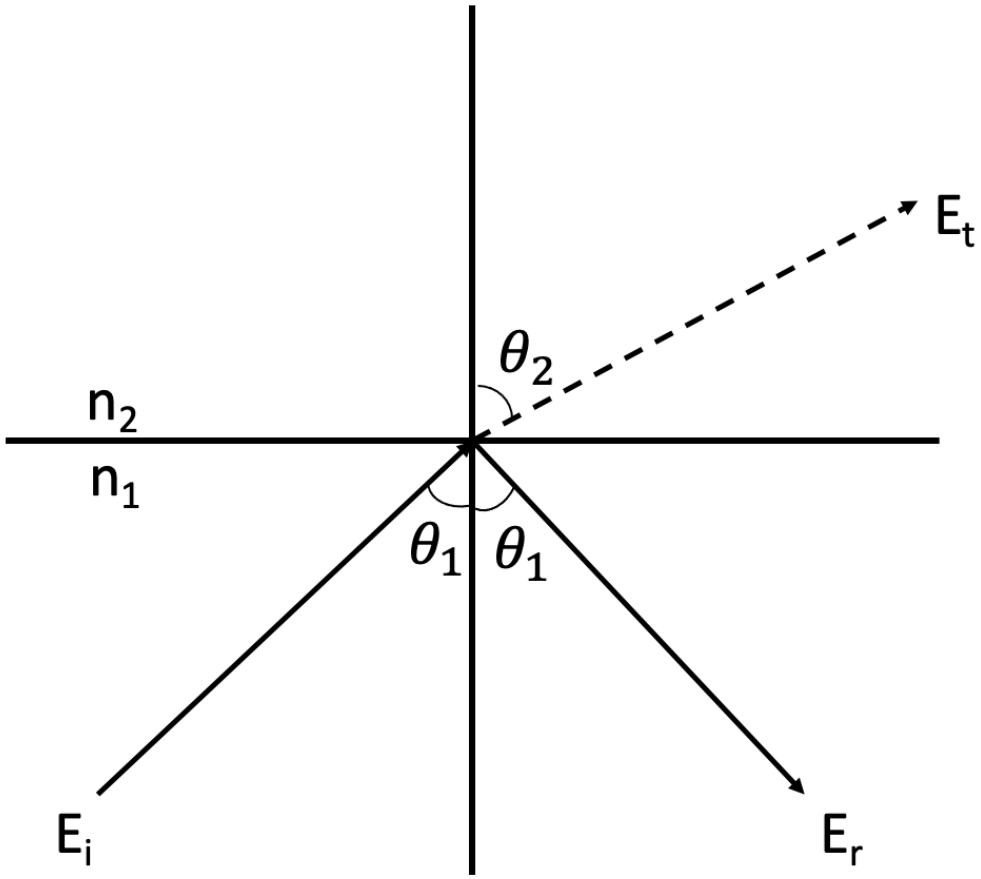

Figure 2.2: Reflection and refraction at an interface between two dielectric media.

The reflections coefficients r_{TE} and r_{TM} are the ratio of the electric fields of the incident and reflected rays.[19,20] Using the definition of the Poynting vector, we can write the power reflection coefficient as

$$R = \frac{S_r}{S_i} = \frac{E_r^2}{E_i^2} = r^2, \tag{2.11}$$

where r is either r_{TE} or r_{TM} depending on the polarization state of the ray in question.

2.1.3 Waveguide modes

When light rays propagate in a waveguide, they can be described as modes of that waveguide.[19] We can derive the conditions for these modes by looking at the geometry of the waveguide and the propagation of a plane wave within the structure. The most basic geometry we will consider for this discussion is that of a planar waveguide, depicted below in Figure 2.3.

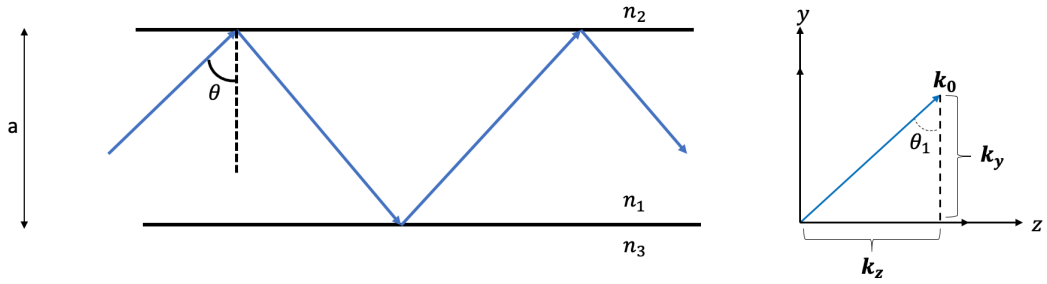

Figure 2.3: Propagation of the k-vector in a planar waveguide.

We define the waveguide thickness as a, and $\boldsymbol{k}$ as the wavevector that defines the direction of propagation of the planewave within the medium.[19] This definition is further broken down as $\boldsymbol{k} = n_1\boldsymbol{k_0}$, where $\boldsymbol{k_0} = \frac{2\pi}{\lambda_0}$, is the free-space wave vector, λ_0 is the free-space wavelength, and n_1 is the refractive index of the waveguide core material. The k-vector in the y and z directions are

$$\boldsymbol{k_z} = n_1 k_0 sin\theta_1 \tag{2.12}$$

$$\boldsymbol{k_y} = n_1 k_0 cos\theta_1. \tag{2.13}$$

The light traveling along the y-direction must create a standing wave in order to be guided by the structure.[19,20] The total phase shift from a round trip length along the y-direction of $2a$ and interaction with both interfaces is

$$\phi_t = 2ak_0 cos\theta_1 - \phi_u - \phi_l, \tag{2.14}$$

where ϕ_u and ϕ_l are the phase shifts due to reflection at the upper and lower interface boundaries respectively. These phase shifts are derived from the reflection coefficients for TE and TM polarization.

The condition for this to form a standing wave sustained along the y-axis is when ϕ_t is an integer multiple of 2π. Therefore

$$2ak_0n_1cos\theta_1 - \phi_u - \phi_l = 2\pi m, \qquad m = 0, 1, 2, 3.... \tag{2.15}$$

Since ϕ_u and ϕ_l are dependent on the reflection coefficients and there for the incident angle θ_1, the equation becomes an implicit equation of θ_1. From this we can see that there are discrete values of theta that satisfy this condition.

Each discrete solution to this condition has its own propagation constants along the y- and z-directions for both TE and TM polarizations. Only these discrete angles of incidence allow propagation along the waveguide with a stable transverse mode profile, and these solutions are what we refer to as the modes of propagation of a waveguide, where the mode number is given by the integer multiple m. Modes are defined by mode number and the polarization type (i.e. TE_0, TM_0, TE_1, TM_1, etc.); each mode has a unique transverse spatial profile.[19,20]

Symmetric planar waveguides

We will begin by considering a symmetric planar waveguide where $n_2 = n_3$. For these waveguides, the phase shifts that occur at the top and bottom interfaces will be equal, so $\phi_u = \phi_l$.[19]

Using this assumption along with (2.15) and (2.9), we can show that

$$2k_0n_1acos\theta_1 - 4tan^{-1}\left[\frac{\sqrt{sin^2\theta_1 - (n_2/n_1)^2}}{cos\theta_1}\right] = 2\pi m. \tag{2.16}$$

By rearranging this equations we see

$$tan\big[(k_0 n_1 a cos\theta_1 - m\pi)/2\big] = \sqrt{sin^2\theta_1 - (n_2/n_1)^2}/cos\theta_1. \tag{2.17}$$

We can see that this equation is entirely dependent on the incident angle θ_1, which can therefore be solved for using this relationship. These values of θ_1 are exclusive to the TE polarization condition. The solutions for the TM condition can be obtained in a similar way using (2.15) and (2.10).

Using this relationship, we can derive the number of maximum modes supported by a waveguide for a given set of parameters. We know from TIR that the minimum supported incident angles is that for which $\theta_1 = \theta_c$. This incident angle will give us the highest order mode that is supported by the waveguide. By setting $\theta_1 = \theta_c$ in (2.17) and using what we know of the critical angle and Snell's law, we can see that the right-hand side of the equation will go to zero, and therefore

$$(k_0 n_1 a cos\theta_c - m_{max}\pi)/2 = 0. \tag{2.18}$$

From here we can see that the maximum allowed number of modes for a waveguide of height a is

$$m_{max} = \frac{k_0 n_1 a cos\theta_c}{\pi}. \tag{2.19}$$

Asymmetric waveguides

For an asymmetric waveguide $n_2 \neq n_3$, so the phase changes at the two interfaces will not be equal. For TE modes, this changes (2.16) to

$$\begin{aligned}[k_0 n_1 a sin\theta_1 - m\pi] = tan^{-1}\Big[\sqrt{sin^2\theta_1 - (n_2/n_1)^2}/cos\theta_1\Big] \\ + tan^{-1}\Big[\sqrt{sin^2\theta_1 - (n_3/n_1)^2}/cos\theta_1\Big].\end{aligned} \tag{2.20}$$

This equation can be solved numerically or graphically to find allowable solutions of θ_1. It should be noted that since the indices are different for the two cladding

layers, TIR requires that the incident angle must exceed the critical angles for both interfaces. When the thickness of the waveguide becomes too small, an asymmetric waveguide will typically no longer support any modes.[19,20]

Single-mode condition

Some waveguides of a certain thickness and refractive indices may only support a single mode.[4,20] We can derive this condition using our understanding of a symmetric waveguide. Let us consider the second mode where $m = 1$ and an incident angle of $\theta_1 = \theta_c$. Since we know that the incident angle for the second mode must be smaller than that for the fundamental mode, we can conclude that for all angles greater than the critical angle, the waveguide will be only support the singular fundamental mode. We may show this by inserting these conditions into (2.16) to get

$$tan\big[(k_o n_1 a cos\theta_c - \pi)\big] = 0. \tag{2.21}$$

From this we can derive

$$cos\theta_c = \frac{\pi}{k_0 n_1 a} = \frac{\lambda_0}{2n_1 a}. \tag{2.22}$$

Here we can see the explicit single mode condition is

$$\theta_c \leq cos^{-1}\left(\frac{\lambda_0}{2n_1 a}\right). \tag{2.23}$$

2.1.4 Effective index

We use the previously defined propagation constant, k_z, often denoted by the variable β to define the effective index of a waveguide. We define the effective index, N as

$$N = n_1 sin\theta_1. \tag{2.24}$$

From this we can rewrite the equation for k_z, as

$$k_z = \beta = N k_0. \tag{2.25}$$

As stated previously, in order for the mode to propagate within an asymmetric waveguide, the angle of incidence must be larger than the angle of incidence for all interfaces and is limited by the interface with the larger refractive index. This critical angle condition determines the lower bound of the propagation constant β, defined by

$$\beta \geq n_1 sin\theta_1 = k_0 n_2. \tag{2.26}$$

Since the upper bound of β is determined by the maximum angle of θ_1 which is 90^o, it follows that $\beta = k = n_1 k_0$. The final result here is

$$k_0 n_1 \geq \beta \geq k_0 n_2. \tag{2.27}$$

By dividing out k_0 from the equation we find that the effective index boundaries are

$$n_1 \geq N \geq n_2. \tag{2.28}$$

2.1.5 Confinement factor of a waveguide

By examining the electric field distribution of modes within a waveguide, we see that for the fundamental mode the intensity distribution is maximum at the center of the waveguide and decreases following a cosine distribution. As the electric field reaches the interfaces, the field does not decay to zero, but it instead penetrates into the upper and lower cladding materials and decays exponentially. For higher order modes, the number of nodes in the standing wave correspond to the mode number. These higher order modes follow the same trend of exponential decay in the cladding material.[19]

By viewing the field distributions in this way, we can see that the field power propagating along the waveguide is not totally confined within the core material, and instead some of the electric field power leaks into the cladding layers. The mode confinement factor is a parameter used to describe the light-guiding property of the

waveguide and is determined by the equation

$$\Gamma = \frac{\int_0^a E_0^2(y)dy}{\int_{-\infty}^{\infty} E_0^2(y)dy}. \tag{2.29}$$

This equation determines which fraction of the electric field power is confined to the guide layer with a height of a. The confinement factor is function of polarization, the refractive indices of the materials, the waveguide thickness and the mode number.[19] The portion of the field that propagates along the waveguide outside of the core layer is known as the evanescent field.[21] This will be discussed in later sections and in regard to ring resonators and similarly coupled devices.

2.1.6 Waveguide parameters and BV diagrams

By solving Maxwell's time-harmonic equations in dielectric media, we can come to understand how electromagnetic waves behave in a three-layer waveguide. These waveguides are defined by a substrate, a guide-layer and a cladding layer with indices of n_3, n_1 and n_2 respectively. Solving these equations gives us generalized parameters that allow us to describe all TE and TM modes that are supported by these waveguides.[19,18] With these generalized parameters we are able to determine the effective index and the dispersion relations of the waveguides which was previously very difficult to do using numerical methods.

For TE modes, the three generalized parameters are the asymmetry measure α, the generalized frequency V, and the generalized guide index b. These parameters are defined by

$$V = k_0 a\sqrt{n_1^2 - n_3^2}, \tag{2.30}$$

$$\alpha = \frac{n_3^2 - n_2^2}{n_1^2 - n_3^2}, \tag{2.31}$$

$$b = \frac{N^2 - n_3^2}{n_1^2 - n_3^2}. \tag{2.32}$$

By using the dispersion relation for TE modes, we can derive the expression

$$V\sqrt{1-b} = (m+1)\pi - tan^{-1}\sqrt{(1-b)/b} - tan^{-1}\sqrt{(1-b)/(b+\alpha)}. \tag{2.33}$$

This equation can be solved numerically and plotted to show a normalized dispersion curve for various modes (values of m) and values of α. From this curve one can determine the effective index of a waveguide from the given indices and the guide thickness.[18]

By following similar methods for TM modes, we can derive two more generalized parameters in addition to the three from before, as seen here:

$$c = \frac{n_3^2}{n_1^2}, \tag{2.34}$$

$$d = \frac{n_2^2}{n_1^2} = c - \alpha(1-c). \tag{2.35}$$

We can then extend the dispersion relation for TM modes to be

$$V\sqrt{1-b} = (m+1)\pi - tan^{-1}\frac{1}{d}\sqrt{(1-b)/b} - tan^{-1}\frac{1}{c}\sqrt{(1-b)/(b+\alpha)}. \tag{2.36}$$

These equations are illustrated in Figure 2.4 as what are commonly referred to a bv-diagrams.

In a waveguide, when the incident angle is equal to the critical angle between the substrate and the guide layer, the light will no longer be confined to the guide layer and will instead begin to propagate in the substrate layer. This conditions is called the cutoff of the guided mode.[18,19,20] For this condition, the parameter $b = 0$ and the effective index is $N = n_3$. Inserting these values into (2.33), we can determine the cutoff condition to be give by

$$V_m = m\pi + tan^{-1}\sqrt{\alpha}. \tag{2.37}$$

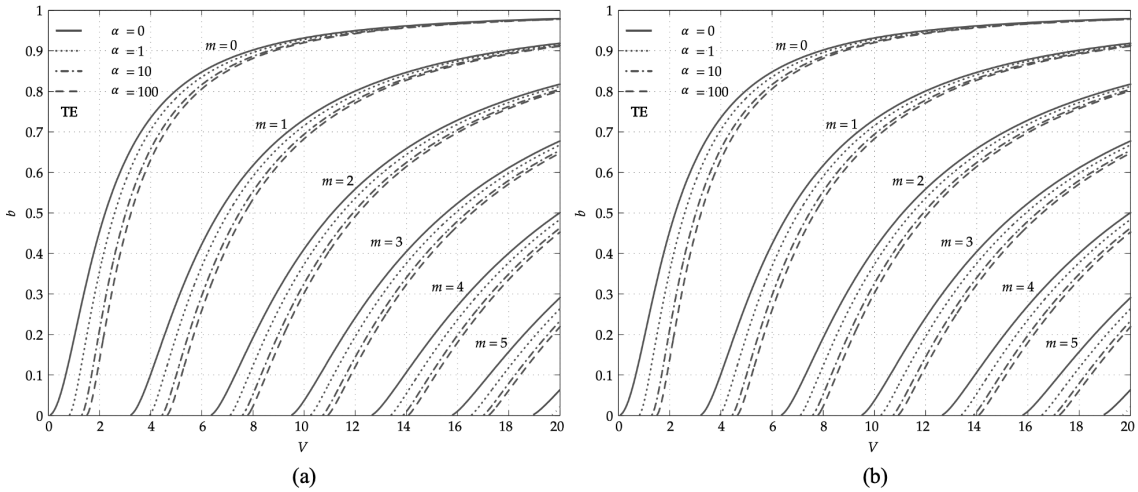

Figure 2.4: bV diagrams for TE (a) and TM (b) modes for step-index thin-film waveguides.[18]

In other words, the cutoff thickness for a guide layer that will allow a mode to be guided is

$$a = \frac{m\pi + tan^{-1}\sqrt{\alpha}}{2\pi\sqrt{n_1^2 - n_3^2}}\lambda_0. \tag{2.38}$$

By a similar derivation, the cutoff frequency for TM modes is given by

$$V_m = m\pi + tan^{-1}\frac{\sqrt{\alpha}}{d} = m\pi + tan^{-1}\left(\frac{n_1^2}{n_2^2}\sqrt{\alpha}\right). \tag{2.39}$$

Since we know that n_2 must be smaller than n_1, we can see that the cutoff for TE modes is slightly smaller than for TM modes of the same mode number m.[18,19]

2.1.7 Waveguide geometries

Although up until this point we have been describing planar slab waveguides, these principles can be extended to various waveguide geometries where the confinement occurs along both the x- and y-directions and not only the y-direction as before. This new confinement is due to the refractive index steps along the x- and y-directions since the electric field must be considered in all three directions, instead of previous cases when we only considered the y- and z-directions.[18,19] For this reason, these

waveguides are referred to as three-dimensional waveguides. Some geometries are summarized in Figure 2.5.

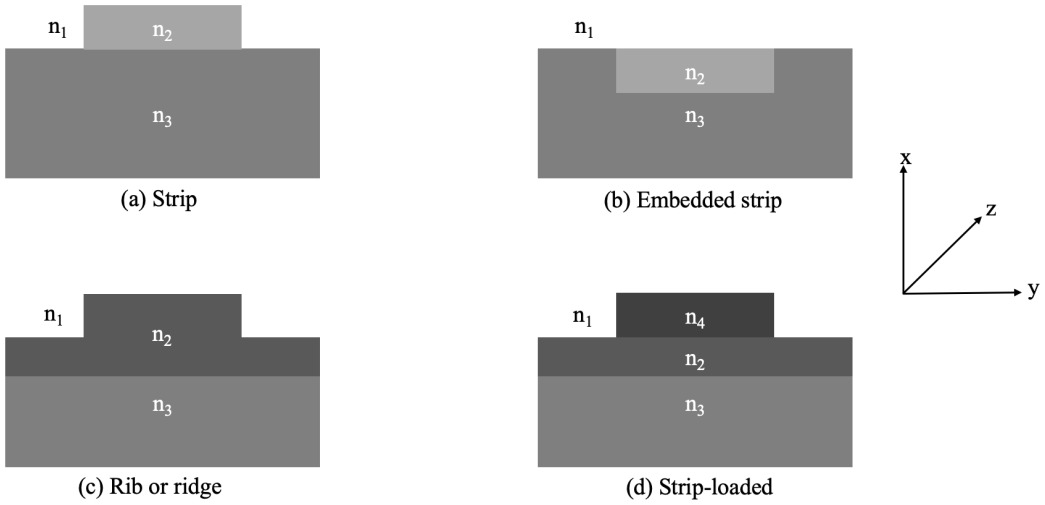

Figure 2.5: Common waveguide geometries.

A strip waveguide (Figure 2.5.a) is a waveguide formed by growing or depositing a core layer on top of a substrate material and then surrounded by air or an alternative cladding material. Similarly, an embedded strip or buried channel waveguide (Figure 2.5.b) is made by altering the substrate material in order to obtain a localized region with a higher RI. These waveguides are typically fabricated using diffusion and used to fabricate lithium niobate waveguides. More information on this fabrication method can be found in Pantchev and Zhang.[22,23]

Ridge waveguides are the types most typically used in this dissertation and are shown in Figure 2.5.c. For this waveguide, a pattern is deposited and then etched away to leave a ridge. With this design total internal reflection occurs at the top and bottom, as well as both sides of the waveguide. Often times, additional material is regrown around the sides of the ridge to better control the mode confinement through index contrast.[18,19] By controlling the confinement in this way, one can achieve tighter bends than with alternative waveguide geometries. Depending on

their intended use, these waveguides can be made out of various materials including crystals, semiconductor materials and polymers. These fabrication processes will be discussed in more depth in later sections.

The final relevant 3D waveguide structure is a strip-loaded waveguide as seen in Figure 2.5.d. This structure consists of a substrate, a planar layer and a ridge. The planar layer is arranged as the cutoff guide layer. The high index material works to guide the mode in a localized region near the ridge. Confinement in the y-direction is possible because the average RI in the x-direction in higher in the region that contains the ridge. This ridge can have a different refractive index than the planar guide material, or the same index as demonstrated in Figures 2.5(c-d).[18,19]

2.1.8 Waveguide loss mechanisms

When working with waveguides it is important to note the most common loss mechanisms within the waveguide. The three sources of loss within the waveguide are absorption, scattering, and radiation loss. Scattering and absorption loss are determined by the fabrication, system parameters and materials of the waveguide, while radiation loss is most important when the waveguides encounter a curve. One additional source of loss is that which comes from coupling in and out of the waveguide via lenses, fibers or other photonic chip components. Each of these sources of loss will be discussed at length below.

Scattering loss

The two main sources of scattering loss in a waveguide are volume scattering, and surface scattering.

Volume scattering occurs when then are imperfections or impurities in the guide material such as defects, voids, impurities. The more imperfections for a given unit volume, the higher the loss per unit length of the waveguide medium. The size of the imperfections relative to the wavelength of the light propagating in the waveguide

also determine the loss of the system. Loss mechanisms with λ^{-4} dependence are known as Rayleigh scattering, while mechanism with a λ^{-3} dependence are known as Mie scattering. Managing the density of imperfections of the material is important in mitigating the overall volume loss of the waveguide.[19]

Surface scattering occurs in a waveguide due to inherent limitations in the technology used in photonic devices. The interface between the substrate, core and cladding materials will always have minor deviations from a perfect atomically smooth surface. These slight deviations contribute to roughness and surface scattering that can be described using the theory derived by Tien that is based on the ray optic theory. Tien's theory allows us to draw a number of conclusions about surface scattering. The two main conclusions are that the loss is proportional to the ratio of roughness of the material to the wavelength, and that the loss of the waveguide will be reduced if the index contrast is reduced. Finally, from Tien's theory, we know that higher order modes will suffer greater scattering loss due to the larger number of reflections that occur on the surfaces for a given distance than with lower order modes[19].[24]

The second variation of surface scattering is sidewall loss. This loss causes imperfections on a smaller order than that described by Tien and are generally due to roughness that occurs in the etching step (dry or wet) of the fabrication process. Payne and Lacey have derived an equation to determine the upper bound of the scattering loss coefficient that is used to show that that loss of a waveguide decreases as the width of the waveguide increases.[19]

Volume and surface scatterings in waveguides are impossible to avoid in any real-world photonic systems, but they should be reduced wherever possible. Regardless, it is necessary to understand these sources and how to account for them when building real systems off ideal simulations or designs.[19]

Radiation loss

Radiation loss is important to consider when studying photonic integrated circuits that connect various optical devices on a single chip. These connections are typically made by bending waveguides to redirect them to other areas on the chip, where power is radiated out of the waveguide bends and contributes to the overall loss of the system. This type of loss is particularly important for the work in this report due to our heavy reliance on optical interconnects and ring resonators.[19,25,26]

Figure 2.6 shows us the top-view geometry of a waveguide bend with refractive indices n_1 and n_2 and how the propagating light radiates evanescently out from the waveguide core and away from cladding material.

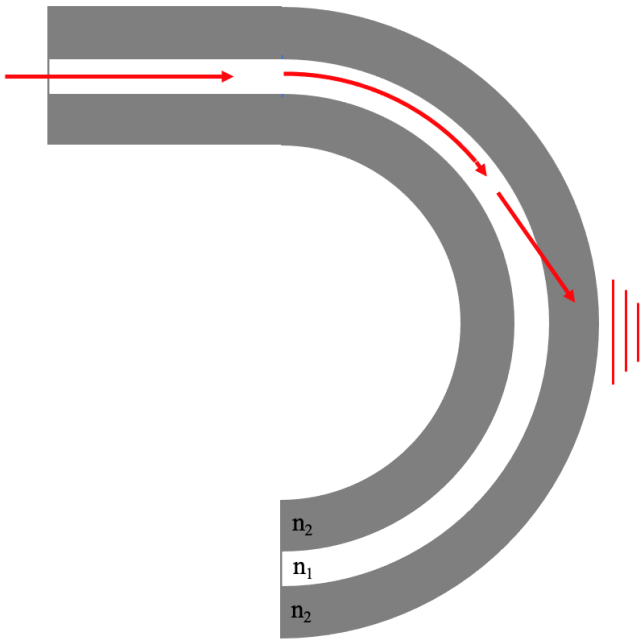

Figure 2.6: Waveguide bend loss.

The mechanisms behind radiation loss of a ring can be explained simply in the following terms. As a mode propagates along the length of a bend of a certain radius of curvature R, then the photons traveling along the outer edge of the curve cannot keep up with the propagation of the rest of the mode. As a result, these photons

split away from the mode and are radiated into the cladding layer. If the radius of the bend is large then it can be approximated as a straight waveguide (where $R \to \infty$) and the mode would behave as described in the previous section.[19]

There have been some approximations of the attenuation coefficients that describe this radiation loss mechanism, but their derivations are beyond the scope of this dissertation. One example can be found in Nishihara et al., which demonstrates that this loss mechanism is dependent exponentially on the radius of curvature of the bend.[27] These reports also demonstrate that the radiation loss become increasingly significant when then difference between the refractive indices of the two layers becomes very small.

This particular loss mechanism will become relevant in further chapters as we discuss ring and disk resonators and their applications.

Coupling loss

The final major source of loss worth considering for the scope of this work is coupling loss. While this type of loss does not come from the waveguides itself, it is important when considering photonic chips in their entirety, especially when they are integrated into functional systems.[25,26]

One of the major obstacles in building optical systems is the difficulty in coupling light in and out of a waveguide via an optical fiber. Optical fibers typically have larger core diameters and lower refractive induces than Si or Si_3N_4 waveguides. Fibers also have symmetric modes while many waveguides on photonic chips are asymmetric. There are many techniques to compensate for these differences in core sizes, indices and symmetries. The most common methods of efficient coupling are prism coupling, grating coupling, butt coupling and end-fire coupling.[19]

Which method is most efficient depends on the overall design and structure of the photonic system. In the following chapters, each system was most simply coupled

using the butt coupling technique where the optical fiber was aligned as closely as possible to the waveguide end at the edge of the photonic chip.

2.1.9 Evanescent fields

As previously discussed, when a ray of light is incident on a core-cladding interface, the light can experience total internal reflection and be guided along the core. Various sources also suggest that when light is incident on this kind of surface, there is a portion of the light that penetrates into the cladding material.[21] Although these statements seem to be at odds, there is consistency between them.

When light is totally internally reflected at an interface, it experiences a phase shift and a lateral shift, together known as the Goos-Hänchen shift. It is possible for this shift to exceed the length of the guide layer thickness and thus penetrate into the cladding layer. The field in the guide layer is known as the evanescent field.[21]

Evanescent fields do not propagate along the direction of the waveguide as the kinds of fields previously discussed do. Instead these field's energy is concentrated and localized. These fields are exceedingly useful in coupling a mode from a waveguide into other photonic devices, as we will see in following sections.[21]

2.1.10 Fabrication

The fabrication of intricate and active photonic chips can become very complicated, very quickly. However, the fabrication of simple devices such as single-layer strip or ridge waveguides is straight-forward. For this work, a basic understanding of the process is sufficient.

Many photonic device designs can be fabricated on commercially available Si or Si_3N_4 wafers using standard photolithographic techniques. However, various other materials can be used in place of Si or Si_3N_4 including semiconductor materials, polymers or glasses.[28] After depositing a photoresist material onto the wafer and

exposing the resist in a pattern of light, applying a developer solvent will cause the resist to either dissolve or strengthen, depending on the type of resit used.[29,30] The pattern of light exposure will create a "mask" for the wafer that leaves only a select region of the wafer exposed and leaves the rest shielded. These patterns can resemble straight waveguides, resonators, couplers or various other devices.

Having sufficiently masked the wafer with resist, the next step is to etch away the uncovered material using either dry reactive ion etching (RIE), or wet etching techniques. The type of etching depends on the material and the devices being fabricated.[31] Post-etching, there remains a pattern of the wafer material that follows the mask pattern. Any excess resist will then be dissolved and a cladding material can be deposited, or air can serve as the waveguide cladding. This process is summarized below in Figure 2.7.

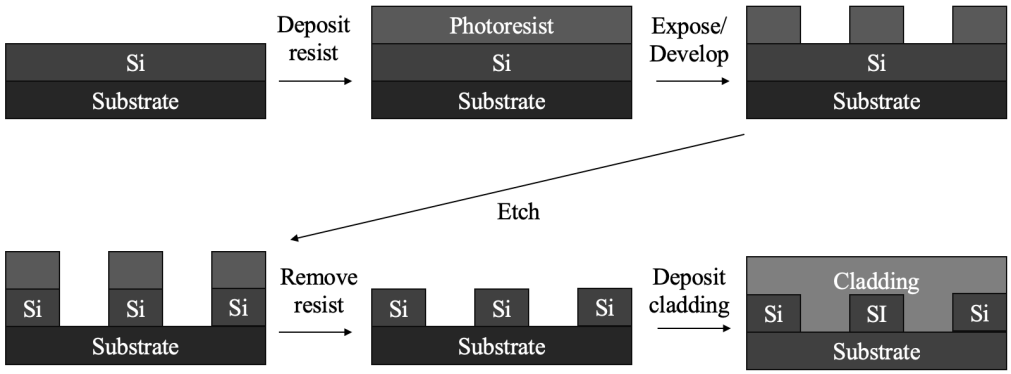

Figure 2.7: Fabrication process for simple, passive photonic devices.

By controlling the fabrications process, we can control the functionality and usefulness of our devices for different optical or electro-optical systems. Control over the fabrication process allows us to fine-tune the device designs, geometries and fabrication materials which is essential for creating optimized devices for specific research or industrial applications.

As shown in previous sections, the design of a waveguide determines all of its fun-

damental characteristics. By changing the height or width of the waveguides, we can control the number and types of modes supported, as well as how efficiently we can couple light into the devices via optical fibers or the other coupling techniques previously discussed. Fabricating these devices with different types of materials allows us to choose materials with appropriate indices and absorption coefficients. This can change the effective index of the waveguides and subsequently the supported modes, the mode confinement, and the radiation loss where applicable.

2.2 Ring and disk resonators

An optical resonator is a cavity in which light can form a standing wave. There are many types of geometries that function as optical resonators, but for this work we will focus only on ring and disk resonators.

2.2.1 Resonator geometry and fabrication

There are many design options when creating microresonators for silicon photonics. Common design options include, but are not limited to, the coupling waveguides, resonator sizes, coupling gap distance, and even their shape.[32] These various designs are summarized below in Figure 2.8.

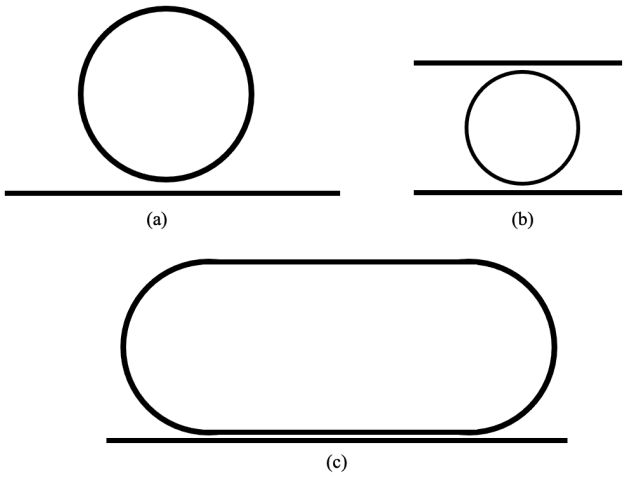

Figure 2.8: Common resonator device designs. (a) A standard ring with one through port waveguide, (b) a ring resonator with a through port and a drop port waveguide and (c) a racetrack resonator design.

The fabrication for basic resonant structures on a photonic chip is the same as that for waveguides discussed in Section 2.1.10.

2.2.2 Microresonator mechanisms

As show in Figure 2.9, light is coupled into the resonator via a waveguide commonly referred to as the through port. As discussed in previous sections, we know that as light propagates along a waveguide, there exists an evanescent field just outside of the waveguide core. Typically this evanescent field is inconsequential on its own, but these fields are what allow us to couple light into a resonant structure. The evanescent wave holds energy that can be transferred into a ring resonator or another optical device such as a directional coupler.[25]

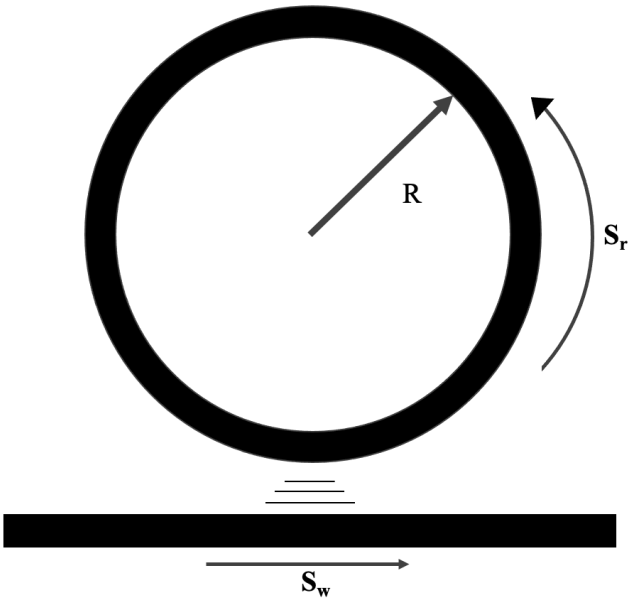

Figure 2.9: Evanescent fields from a waveguide generated by the wave S_w couple into the resonator and propagate along the circumference as S_r.

Once the energy is coupled into the resonator, it can propagate in a similar fashion to our previously discussed waveguide structures. As with the simple waveguide design, the light is totally internally reflected off the interfaces as it travels along the circumference of the resonator. The light will continue along this path until it is radiated out or evanescently coupled back into the bus waveguide by the same mechanism it was coupled in. Alternatively, a second waveguide could serve as a drop port for the light to couple out of, rather than back into the bus waveguide, but for our discussion, one waveguide is sufficient.[25]

By the nature of a resonator, only select wavelengths can couple into and propagate inside the resonant structure. In order to form standing waves, only wavelengths that are integer multiples of the round trip optical path length of the resonator will be supported. These supported wavelengths are given by the equation

$$n\lambda_n = 2\pi R, \tag{2.40}$$

where R is the radius of the ring, and n is a positive integer. All other wavelengths will not form standing modes and will instead destructively interfere within the waveguide and not contribute to the build up of energy within the cavity.[19,32]

2.2.3 Resonator characteristics

Perhaps the most defining characteristic of a resonator is its quality factor, or simply the Q factor. This parameter is used to indicate the energy loss within the resonator. For an optical ring resonator, the Q factor is defined as the energy stored in the resonator per optical cycle, divided by power coupled or scattered out of the resonator per optical cycle. For typical resonators, this dimensionless parameter is often on the order of 10^3 or 10^4.[32] For high quality resonators however, the Q factor can reach as high as the millions or even billions. In terms of parameters of the resonator system, the Q factor is defined as

$$Q = \frac{2\pi^2 R n_e}{\lambda_0 \kappa^2}, \tag{2.41}$$

where R is the radius of the resonator, n_e is the effective index of the resonator determined by its guide materials, substrate and cladding materials and the operating wavelength, λ_0 is the resonant wavelength, and κ is the coupling constant defined as the fraction of power that is coupled out of the ring due to coupling to the bus and waveguide losses.[25] The Q factor can be tuned by changing the device geometry, optimizing the fabrications processes and the coupling efficiency, as well as material selection.

The Q factor of a resonator can be determined experimentally using standard photonic chip testing techniques. When a broadband or tunable laser source is directed into a ring resonator, only certain wavelengths of light will resonate in the structure, as discussed previously. Therefore, the output spectrum of will resemble a Lorentzian shape about the resonant wavelength. The Q factor can be calculated

using

$$Q = \frac{\lambda_0}{\sigma_\lambda}, \tag{2.42}$$

where σ_λ is the full width half max of the Lorentzian.[20]

Two other useful characterization of a microresonator are the resonant wavelengths and the free spectral range (FSR). The FSR is the separation between wavelengths or frequencies that will be resonate within the structure.[32] It is defined mathematically as

$$\nu_F = \frac{c}{2\pi R}. \tag{2.43}$$

Each of these parameters can be affected by the device design, its dimensions, the materials used, and for some parameters such as the resonant wavelength, the temperature of the device. A schematic of a basic measurement setup used to characterize resonator devices can be seen in Figure 4.2. The measurements and alterations of these parameters will be discussed further in the following section.

2.2.4 Resonator tuning

As discussed previously, there are many methods of changing the characteristic parameters of a resonator through the device design, or external manipulations. In this section we will explore the most common and relevant methods which include affecting the absorption of the material, the polarization, and the temperature of the device.

Material absorption

As we can see from (2.41), the Q factor is inversely proportional to the coupling constant of the device, which can be broadly defined to describe the loss of the resonator system, whether that be from the light coupling out of the ring, radiation loss, or absorption of light by the device materials.[19] From this we can deduce that by altering the materials to absorb more or less light in the device, we can affect the spectrum of the resonator determined by the Q factor.

Polarization

As noted previously, whether or not a mode is supported by a waveguide, and subsequently a resonator structure, is dependent on the polarization of the light. For any given system, it is likely that the system will better support either TE or TM polarization modes, depending on the design and materials of the devices. For these cases, the polarization can be tuned to optimize the performance of the waveguides as well as the resonator structures. Additionally, if the polarization of the light changes along the path of the device, it can introduce losses to the system reducing the overall output, and the Q factor of the resonator.[19] We will see in later chapters how the polarization can be altered within the device to modulate the signal of a resonator structure.

Temperature

One very common method of tuning a resonator is through using temperature to affect its effective index - this is known as thermal tuning. The thermo-optic effect describes how a change in temperature can change the index of refraction of an optical material. How greatly the change in temperature affects the indices is determined by the thermo-optic coefficient of the material, dn/dT. This change in the refractive indices induces a change in the effective index of the waveguide and the resonator.[18,19,25] The shift in wavelength with temperature is described by the equation

$$\frac{1}{\lambda_r}\frac{\lambda_r}{dT}(\lambda) = \frac{1}{n_g}\frac{dn_{eff}}{dT}(\lambda), \tag{2.44}$$

where λ_r is the resonance wavelength, n_{eff} is the effective index, n_g is the group index and T is the temperature.[33,25] This phenomenon can be used to tune the resonators to specific operating wavelengths so that their effective use can be optimized in various systems and applications.

CHAPTER 3

Dual-band Si_3N_4 waveguides

Here we explore a novel concept for dual-band Si_3N_4 waveguides that operate at C-band and mid-IR wavelengths for telecom and gas sensing applications respectively.

3.1 Introduction and Mid-IR applications

The ability to detect and transmit light in the mid-wave infrared (MWIR) has significant implications for applications in organic gas sensing.[11] Many volatiles such as carbon monoxide, methane, nitrous oxide have spectral signatures in the MWIR regime.[12,34] The ability to transmit information from these wavelengths is essential for detection systems that can be used to manage the amount of these potentially harmful gasses and maintain adequate safety measures. The ability to integrate these senors into systems with the dual capacity to operate at C-band wavelengths could increase the efficiency of these system through commercial fabrication techniques.

The current limitations for these systems come from inefficient devices used to collect and guide light at MWIR wavelengths. In order to guide modes of longer wavelengths, the resulting larger mode diameter needs to be well-confined to a waveguide structure. The simplest method of overcoming this is to make the core of the waveguide larger to accommodate the increase in mode size. Unfortunately, although fabricating wide waveguide structures is relatively simple, fabricating waveguide with large thicknesses is more difficult. It is difficult to grow thick wafer layers used in current fabrication processes, and to spin-coat thick layers of alternative materials, so achieving the potential for thick waveguide material is already diffi-

cult.[35,36] Additionally, another barrier is that even if there were larger structures in place, etching smooth sidewalls require intricate deep reactive ion etching techniques which can be complicated and difficult to optimize.[31]

In this work we have simulated, fabricated and tested a waveguide structure designed to operate at 1.55 μm and 4.6 μm. These are fabricated using standard fabrication techniques and materials available though the AIM foundry.[37] The waveguide design consists of three Si_3N_4 waveguides in parallel. Each waveguide is 220 nm in height and 1.5 μm wide, spaced 2.5 μm apart with a SiO_2 cladding. These are standard waveguide dimensions used to guide single-mode light at 1.55 μm. At 4.6 μm the area covered by the three waveguides allows them to guide a single supermode created by the modes confined to each individual waveguide.[38,39] Through this design we can show a dual-band waveguide for both telecommunications and MWIR applications.

3.2 Dual-band waveguide simulations for 4.6 μm

We began this work by simulating the triple waveguide design versus a single Si_3N_4 waveguide design of the same dimensions to learn more about the mode confinement and how well we could expect the light to be guided in both designs. The initial mode simulations for the two designs are show in Figure 3.1.

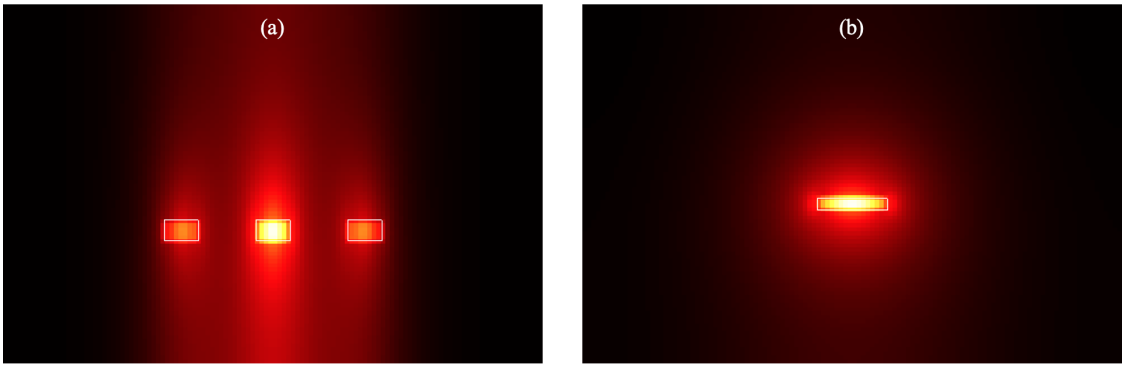

Figure 3.1: Mode confinement simulation done in FIMMWAVE for the triple (a) and single (b) waveguide designs.

From these simulations we can see clearly the single-mode behavior for the 1.55 μm light. For the 4.6 μm light we observe each individual waveguide shows mode behavior, that when superimposed together act as a single supermode. To better understand the energy distribution from these simulations we calculated the confinement factor in the core of the single waveguide, and the total confinement to the three cores of the triple waveguide design. These results show that the triple waveguide design confines approximately 1.5x more light than the single waveguide. We suspect the reduction in confinement for the single waveguide will cause more radiation loss and a higher insertion loss when compared to the triple waveguide structure.

These simulations show the mode behavior that we were expecting to see for each of these designs, where the triple waveguide design better confines and guides light at 4.6 μm as compared to the single waveguide.

3.3 Characterization setup

3.3.1 MWIR fiber characterization

Before characterizing the insertion loss of the waveguides, we investigated the alignment tolerance of MWIR IR flex IRF-S-9 optical fiber at 4.6 μm. The fiber has a core diameter of 9 μm, and index of 2.4 and an NA of 0.3.[40] For these measurements we directed a Arroyo 6310-QCL laser into our optical fiber and aligned two fibers to the maximum coupling value and shifted them horizontally, vertically and longitudinally while tracking the reduction in coupled power between the two fibers. The setup for these measurements is depicted in Figure 3.2.

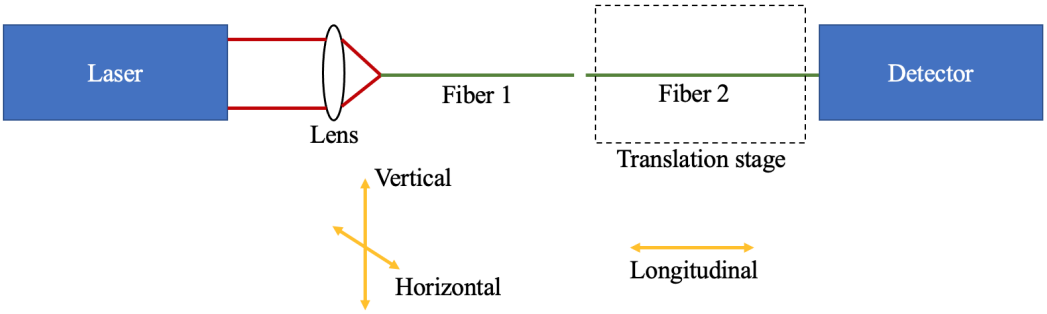

Figure 3.2: Schematic of the IR flex fiber tolerance measurements at 4.6 μm.

The horizontal and vertical tolerance measurements are shown in Figures 3.3 and 3.4. These curves were fitted to the equation

$$Loss = \frac{4w_1^2 w_2^2}{(w_1 + w_2)^2} exp\left[-\frac{2(\Delta x)^2}{w_1^2 + w_2^2}\right], \tag{3.1}$$

where w_1 and w_2 are the two fiber core diameters, and Δx is the the alignment offset.[41] These results here show that there is ± 5 μm offset tolerance in the horizontal direction and ± 7 μm in the vertical direction before 3 dB of the light is lost.

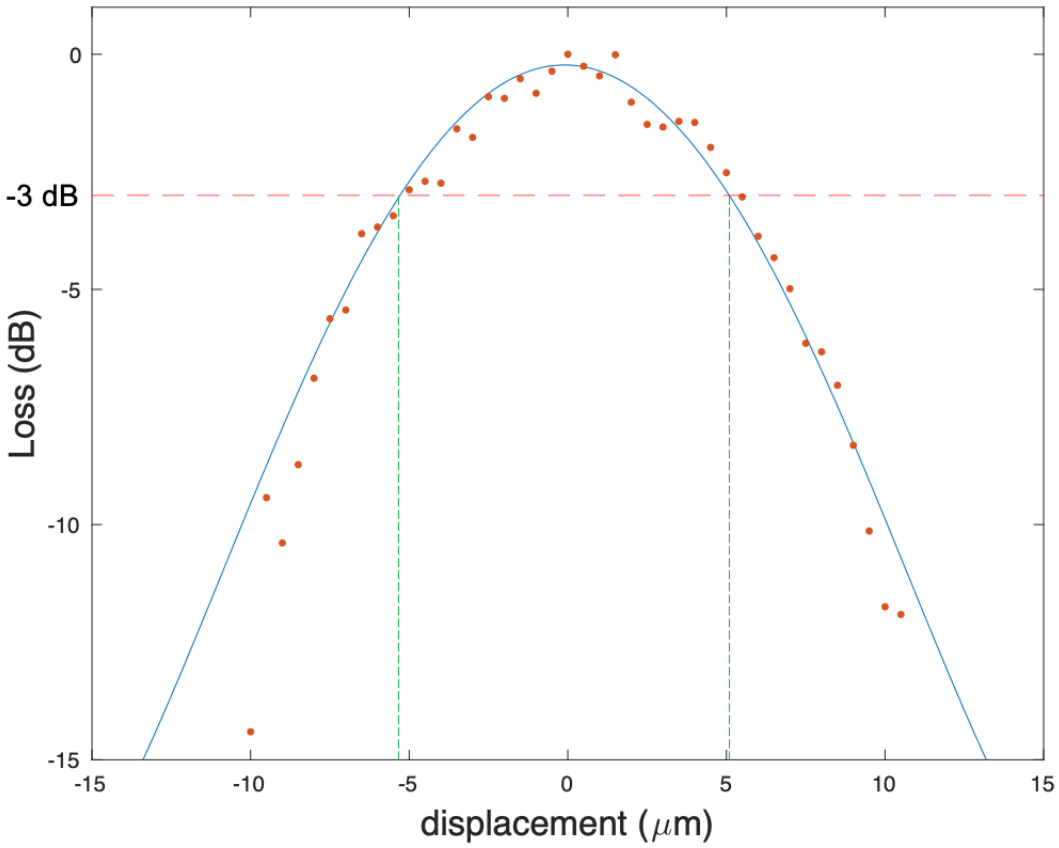

Figure 3.3: Horizontal alignment tolerance for and IR flex fiber at 4.6 μm and optimum lateral displacement.

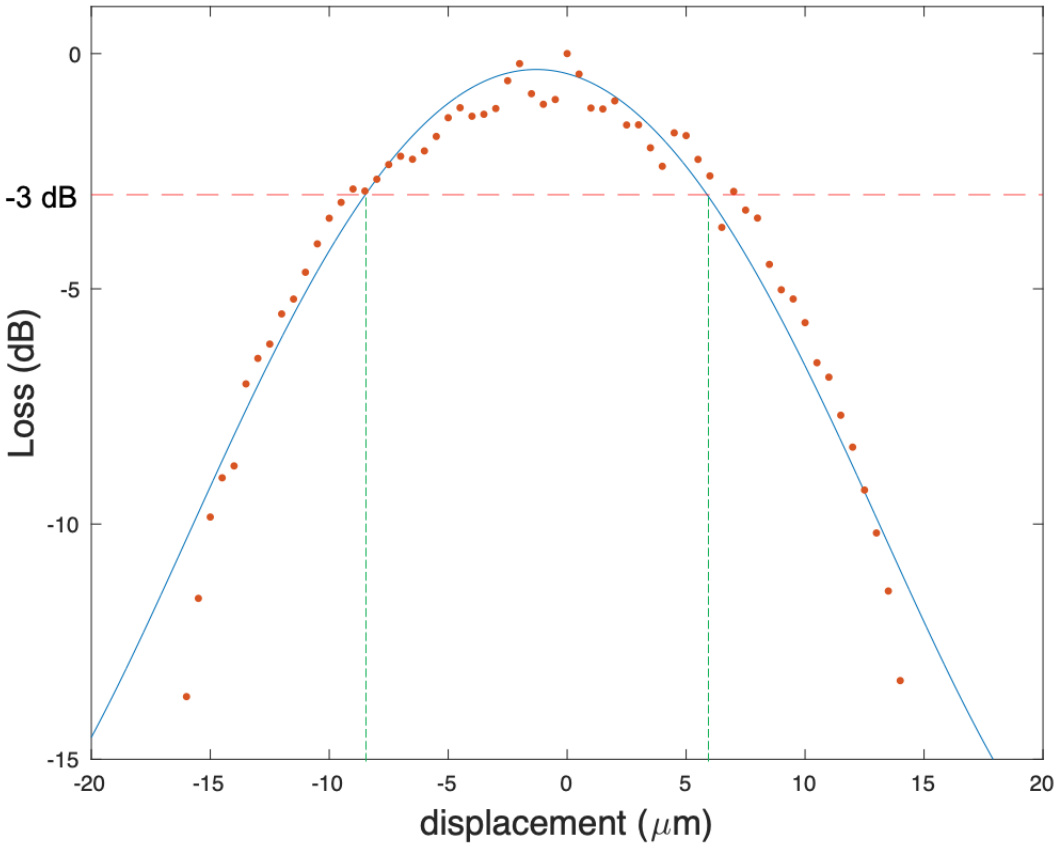

Figure 3.4: Vertical alignment tolerance for and IR flex fiber at 4.6 μm and optimum lateral displacement.

For the longitudinal misalignment the coupling was maximized and the separation between the fibers was increased and the coupled power was recorded. These results are shown in Figure 3.5 and are fitted using the equation

$$Loss = \frac{1}{1 + \left(\frac{z}{z_0}\right)^2}, \qquad z_0 = \frac{2n_0a^2}{\lambda}, \tag{3.2}$$

where λ is the wavelength, n_0 is the index of the material between the fibers, and a is the fiber core diameter.[42]

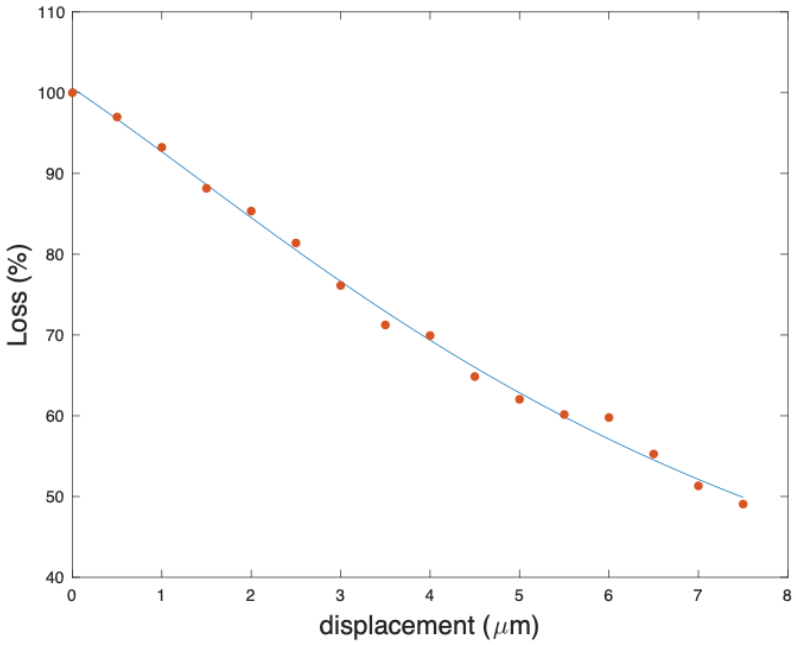

Figure 3.5: Longitudinal alignment tolerance for an IR flex fiber at 4.6 μm.

These results show that there is approximately 7 μm of tolerance before half of the light is no longer coupled into the second fiber.

These results indicate that we should have greater alignment tolerance than we see with standard single-mode fibers at shorter wavelengths.

3.3.2 MWIR insertion loss measurement setup

To measure the insertion loss, a 4.6 μm laser was coupled into MWIR fiber and butt-coupled into the chip. After the baseline power from the fiber was measured, the output power was focused onto a detector through an objective lens. A schematic of this setup can be seen in Figure 3.6.

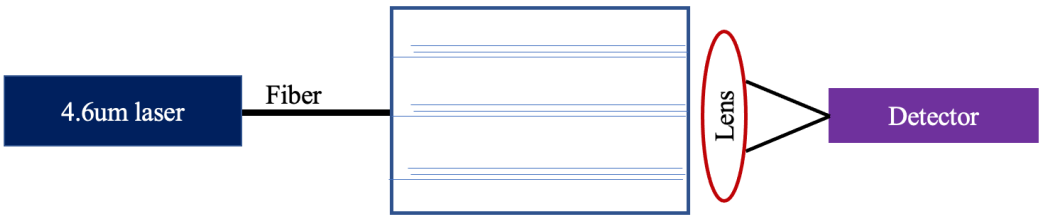

Figure 3.6: Schematic of the setup used to measure the insertion loss at 4.6 μm.

Although our initial setup and fiber considerations used an IR flex chalcogenide fiber, coupling into our chip with this fiber led to a significant amount of light in the substrate and cladding material. A camera image of this mode is shown in Figure 3.7. In an attempt to decrease the light in the material surrounding the waveguide structure, we decided to use an InF_3 fiber in our setup. The core diameter of the INF_3 fiber is 9.5 μm, the NA is 0.3 and the core index is 1.49.[43,44] These specifications are comparable to the IR flex fiber and we can assume it will work similarly with our setup without and significant changes in alignment tolerance.

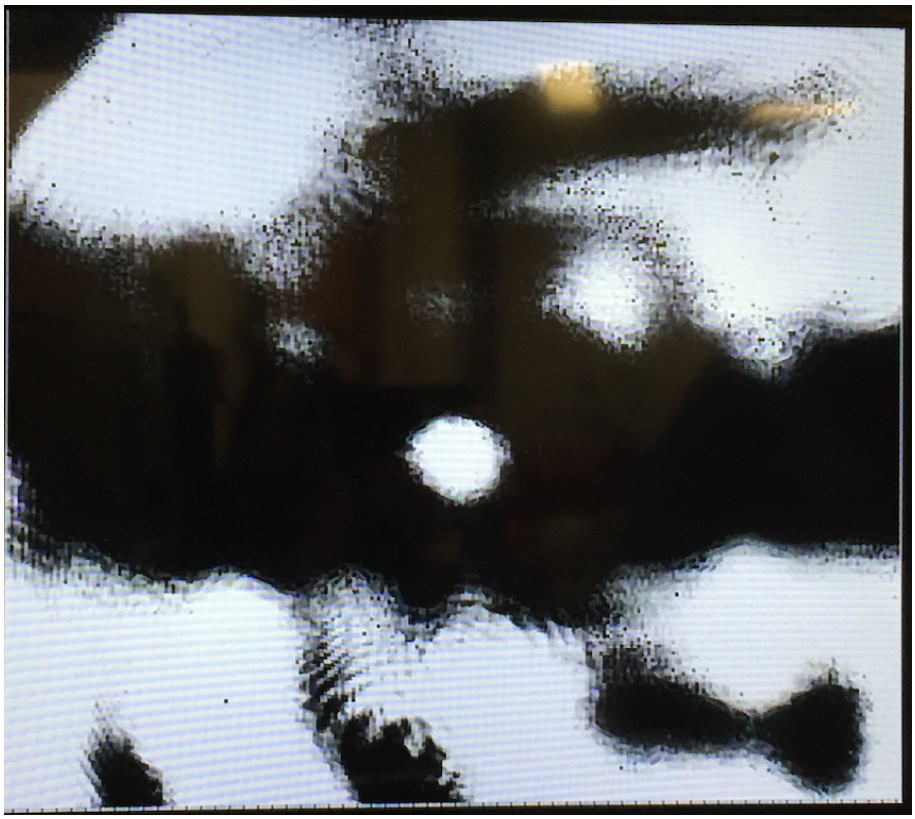

Figure 3.7: The mode guided by the triple waveguide structure and couple with an IR Flex fiber.

The edge couplers are still not sufficiently aligned to direct all of the light from the fiber into the waveguide structure. As a result, a portion of the light was transmitted through the cladding and substrate material, although this was still significant improvement from the substrate light seen with the IR flex fiber. When calculating insertion loss, the ambient substrate and cladding light was not included in the guided wave power measurements.

This same method and measurement setup was used to measure the insertion loss at 1.55 μm and 4.6 μm.

3.4 Insertion loss measurements

The guided modes out of the triple and single waveguide imaged by our camera are seen in Figure 3.8. Both images were taken at the same distance with the same objective lens to maintain a consistent cross-sectional area. These modes behave was we expected from our previous simulations. The larger mode area guided by the single waveguide does not confine the mode to the waveguide dimensions as well as the triple waveguide design.

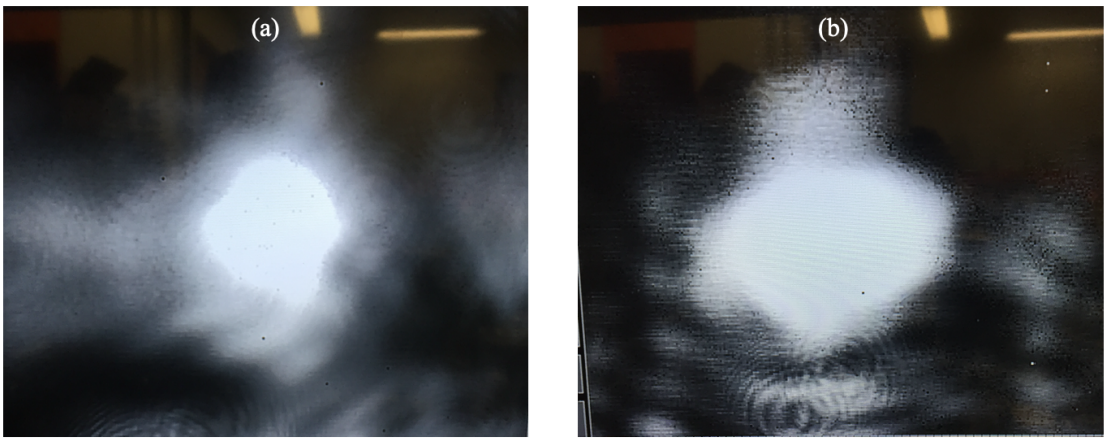

Figure 3.8: Camera images of the modes guided by the triple (a) and single (b) waveguide designs.

The insertion loss measurements for our four single waveguide structures at both wavelengths are summarized below in table 3.1. The insertion loss at 4.6μm is much higher than for 1.55μm, which is consistent with our simulations. These results, paired with our mode geometry, support our hypothesis that the reduction in output power is likely caused by increased losses resulting from the poor mode confinement.

Waveguide	1.55 μm insertion loss	4.6 μm insertion loss
1	-5.64 dB	-10.56 dB
2	-4.94 dB	-9.92 dB
3	-6.08 dB	-10.05 dB
4	-5.09 dB	-9.89 dB

Table 3.1: Insertion losses at 1.55 and 4.6 μm through the single Si_3N_4 waveguide design.

The insertion losses for the triple dual-band waveguide in table 3.2 show comparable insertion losses at both wavelengths. The increase in loss at 1.55 μm is caused by directional coupling effects where some of the light is coupled into neighboring waveguides as it propagates along the chip.[45] The results at 4.6 μm indicate that the triple waveguide structure guides MWIR modes with approximately 2 times better insertion loss than the single waveguide design. These discrepancies with the previous confinement factor simulations that predicted the triple core design would have 1.5 times better insertion losses can be attributed to propagation losses from the increase in propagation length for the single waveguide design.

Waveguide	1.55 μm insertion loss	4.6 μm insertion loss
1	-7.98 dB	-7.08 dB
2	-7.53 dB	-7.00 dB
3	-7.51 dB	-6.70 dB
4	-7.04 dB	-6.98 dB
5	-8.51 dB	-7.24 dB
6	-8.02 dB	-7.65 dB

Table 3.2: Insertion losses at 1.55 and 4.6 μm through the triple Si_3N_4 waveguide design.

3.5 Conclusions

We have successfully demonstrated functional dual-band waveguide designs that operate at 1.55 μm and 4.6 μm with insertion losses as low as -7.04 dB and -6.70 db for the respective wavelengths. Simulations indicate that there is successful guiding of a single supermode in the MWIR regime. These results are encouraging for applications in organic sensing. The ability to fabricate functional devices for MWIR operation using large-scale fabrication techniques and materials overcomes many of the current barriers to MWIR photonic device production and development. Future work in this field includes further characterization of propagation losses in the current device structures, as well as characterization of vertically stacked waveguide designs that include a Si layer. Additional work includes investigating the validity of integrating these devices with alternative materials such as MWIR compatible polymers for lower loss applications.

CHAPTER 4

Si_3N_4 resonator tuning using an external 478 nm laser source

In this chapter we explore the validity of using an external short-wavelength visible laser source to thermally tune optical resonators for performance optimization.

4.1 Introduction

Photonic integrated circuits (PICs) and microresonators used in data processing, collection, and storage applications are instrumental in meeting the increasingly high demands of internet traffic and data communications.[46] Although exceedingly useful in these areas, PICs can be complicated in their fabrication and operation within optical systems. The tuning of optical resonators to meet specific operational parameters is crucial to the functionality of these systems, although current methods of thermally tuning the resonance wavelength of these resonators require either bulky thermal stages that operate with high power consumption and require considerable time to stabilize or intricate fabrication techniques to place heaters directly onto or within PICs.[47] By using an external short wavelength light source, we can thermally tune passive PICs without the need for complex heating systems, significantly reducing power consumption.

A further advantage is the ability to focus our laser onto specific areas of our integrated photonic chip, thereby allowing us to isolate which passive devices can be optically tuned in a manner not possible with a thermal stage and much more difficult with on-chip heater systems.

4.2 Experimental setup and design

As stated previously in Section 2.2.4, by changing the temperature of a ring resonator we can change the resonant wavelength supported by device. The temperature affects the indices of refraction of the materials according to their thermo-optic coefficient, dn/dT.[19] Changing the indices subsequently changes the effective index of the resonators, thus shifting the resonant wavelength.[18] This resonance shift is described by the equation

$$\frac{1}{\lambda_r}\frac{\lambda_r}{dT}(\lambda) = \frac{1}{n_g}\frac{dn_{eff}}{dT}(\lambda), \tag{4.1}$$

where λ_r is the resonance wavelength, n_{eff} is the effective index, n_g is the group index and T is the temperature.[33,25] By using a short visible wavelength laser to heat the device through absorption mechanisms, we can tune the rings without need for a thermal stage or integrated electronic heaters.[48,49]

To demonstrate this phenomenon, we began with a silicon substrate passive photonic chip with Si_3N_4 ring resonators with a cladding material fabricated by the AIM Photonics foundry. A single bus waveguide is used to butt-couple light into four different resonators, the spectra of which were analyzed through their individual drop ports. The full chip dimensions were 8.5mm x 6mm, and the ring diameters measured 300 μm. The layout design of the ring devices used can be seen in Figure 4.1. To measure the Q factor and resonant wavelengths of the device, we fiber coupled a PriTel Inc FA model optical fiber amplifier laser source into the input facets of the through port waveguide of the device, and then fiber coupled the light through the drop ports' end facets and into a Yokogawa AQ6370B optical spectrum analyzer. With this basic design setup we were able to measure the resonance peaks of each of the rings and determine the resonant shifts as a function of tuning parameters. The resonant peak was measured as the most prominent extrema for the four resonator drop ports and the through port where applicable.

Figure 4.1: Si_3N_4 chip design with microring resonators.

To measure the resonator tuning as a function of temperature, we used the same setup described previously, with the chip secured on a thermal stage. The temperature of the chip was reasonably assumed to be the same temperature as the stage.

We explored two methods of opto-thermal tuning using an external laser diode source: full-chip tuning, and targeted tuning. Both of these methods used a 478 nm laser diode source from Nichia. For the full-chip method, the chip was fiber coupled to an SMF-28 optical fiber in the same manner described previously, and a 478 nm source was mounted beside the chip and used to illuminate the photonic chip directly. The laser spot size was measured to be 6.5mm x 7mm along its principle axis, comparable in size to the full chip dimensions. The resonant wavelength as a function of external laser power was measured using the OSA, as before. The temperature of the chip was assumed to be proportional to the laser power. The second method - focused tuning - involved mounting another 478 nm diode source onto a microscope and directing the laser beam onto the individual microrings where the resonance shift could be measured as a function of laser power. The spot size of the second laser diode after it passed through the microscope was elliptical and roughly 300 μm x 600 μm along the principal beam axes. The beam was oriented so that the longer axis extended vertically in relation to the rings. This orientation was chosen so that the beam's interaction with neighboring rings would be minimized. Schematics of the measurement setup and the three methods of tuning these resonators are depicted in Figure 4.2.

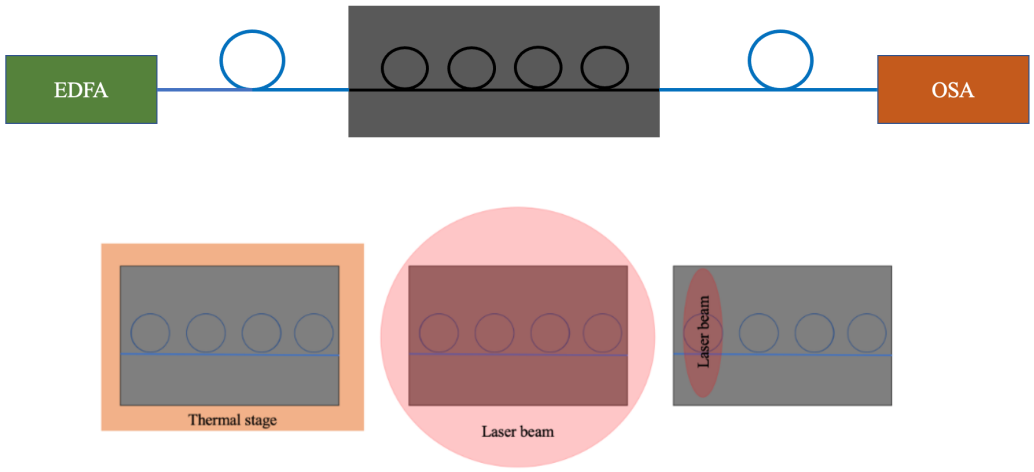

Figure 4.2: Schematic of the resonator characterization setup and depictions of the three tuning methods explored: thermal tuning (left), full-chip laser beam tuning (middle) and targeted laser beam tuning (right).

In addition to measuring the resonant shift with laser power, we also measured the shift of one resonator as a result of directing the laser on to each of its neighboring resonators. With this information, we were able to demonstrate the extent of thermal isolation across the chip and how the separation distance between the external laser beam and the resonator affected the shift in the resonant wavelengths.

To further explore the effect of chip design and material in the resonator's thermal isolation and the tuning capabilities of the external laser method, the SiO_2 cladding material between each resonator was etched away to create a thermal barrier and reduce the thermal cross talk between the rings during the targeted laser tuning. This etching process was done using standard techniques and a Plasmatherm Versaline DSE III reactive ion etcher with a reliable SiO_2 etch recipe. Post-etching, we measured the resonant shifts of each of the rings with laser power in the same manner as before. We measured this for the individual rings illuminated by the external source, as well as the the shift that resulted from illuminating each of its

neighbors. From this we determined the viability of increasing the tuning capabilities as well as the thermal isolation of the rings across the chip as compared to our results before etching the cladding layer.

4.3 Results

Thermal Tuning

Before testing the tuning capabilities of an external laser source, we measured the thermal characteristics of the chip with standard thermal tuning methods. From this we found that the resonance position shifted by an average of 16.1 pm/^{o}C for the five drop ports. These results are shown below in Figure 4.3. This result is consistent with the relatively low thermal-optic coefficients of silicon nitride and silicon dioxide which are $2.45 \times 10^{-5}/^oC$ and $0.86 \times 10^{-5}/^oC$ respectively.[50,51]

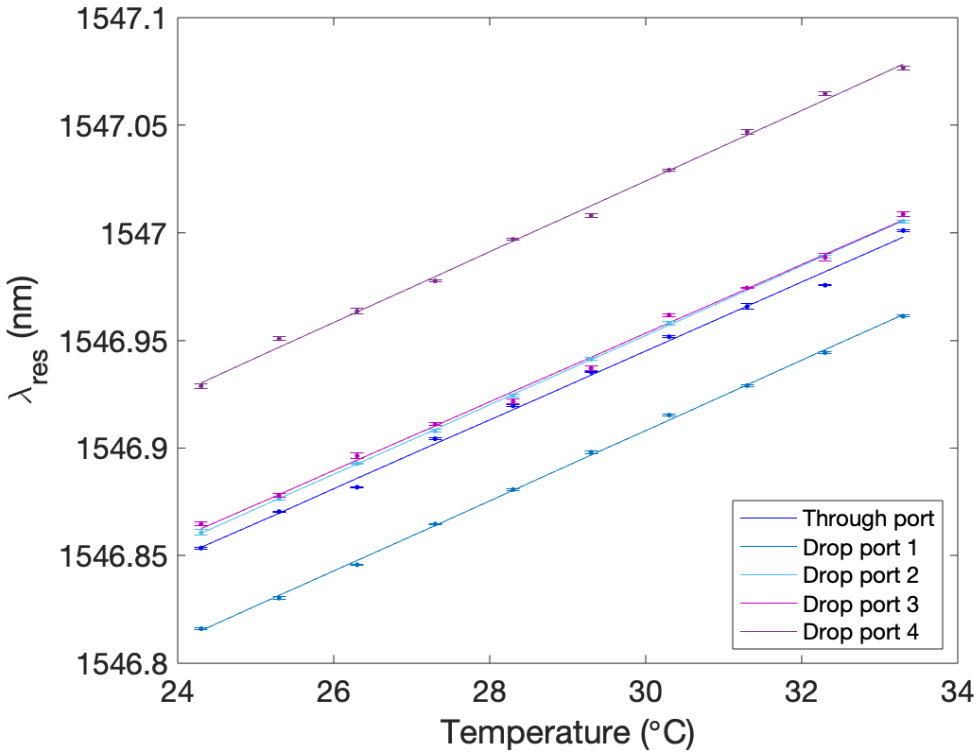

Figure 4.3: Shift in λ_{res} as a function of thermal stage temperature.

Full laser tuning

With the method of full-chip laser tuning, we demonstrated an average shift of 16.6 pm/mW. These results can be seen in Figure 4.4. Comparisons with our thermal tuning results indicate that one milliwatt of power resulted in an increase in temperature of approximately 1^oC. The power of our laser was one limitation we saw with this alternative tuning method. The power we could safely create with our laser diode and direct onto the chip did not offer a very high temperature or overall shift in wavelength as compared to the standard methods of thermal tuning. These limitations can be bypassed in future experiments by implementing a more powerful laser source which would likely show a comparable shift in wavelength while still operating with comparable power consumption to that of a thermal stage.

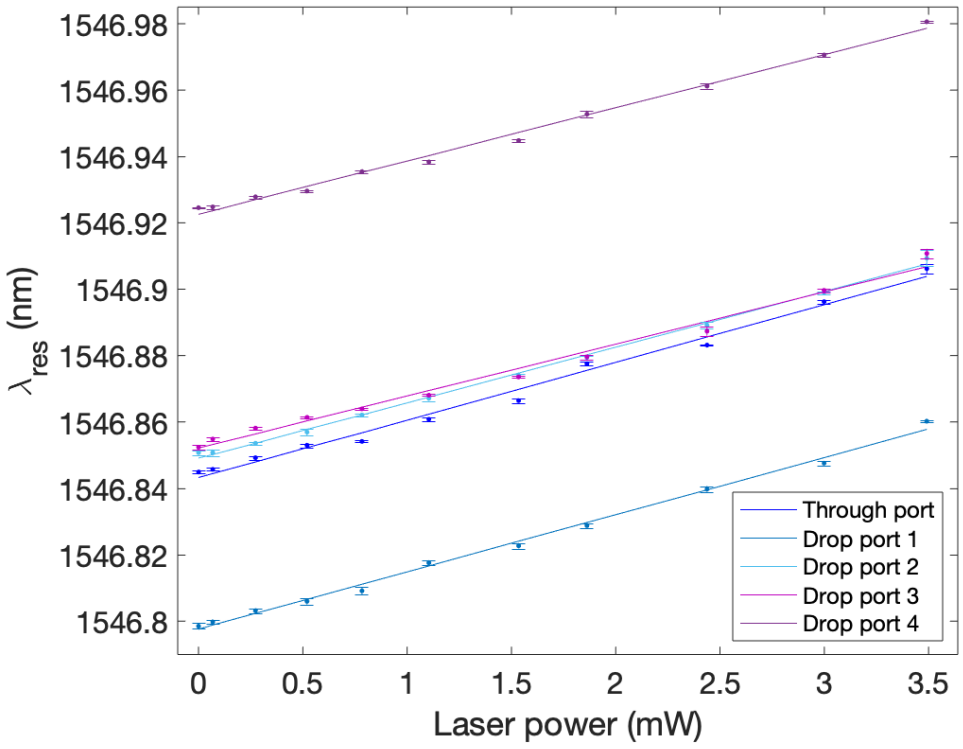

Figure 4.4: Full-chip laser tuning of λ_{res} as a function of laser power.

Focused laser tuning: pre-etch

An average wavelength shift of 24.4 pm/mW was demonstrated with the targeted laser tuning method, which can be seen in Figure 4.6. It should be noted that there was a considerable amount of optical loss through the microscope setup when compared to the available power of the full-chip method - about an 80% reduction in power. This decrease in laser power directed on to the ring resulted in a smaller absolute shift in wavelength. However, even at these lower total powers, this method still demonstrated a larger shift in the wavelength as a function of laser power when compared to the full-chip illumination method.

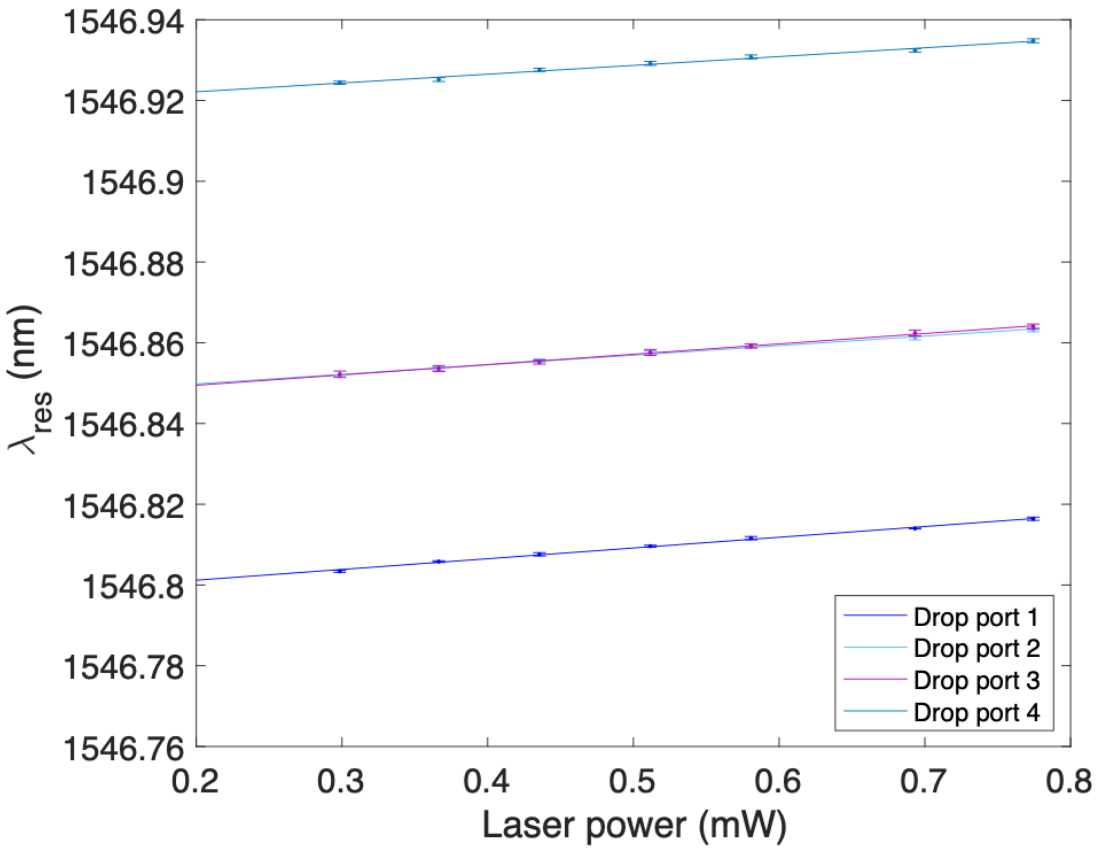

Figure 4.5: Targeted tuning of λ_{res} vs. laser power.

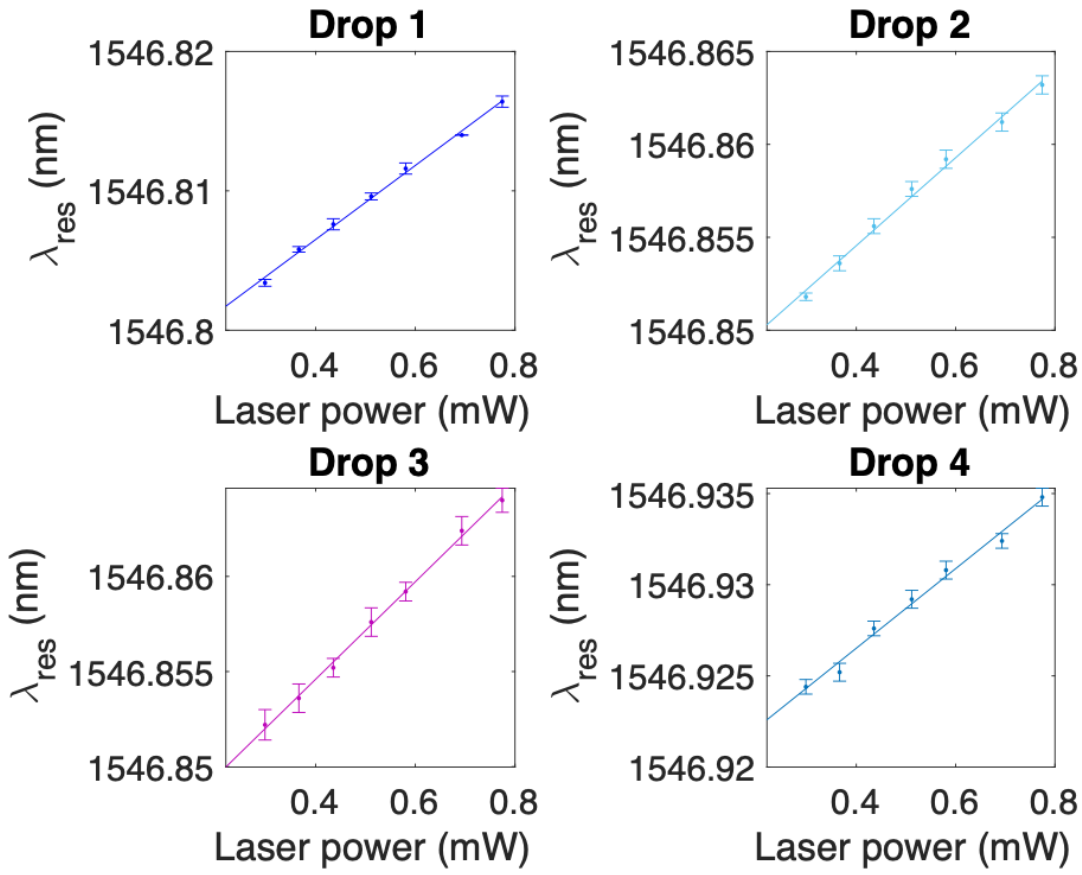

Figure 4.6: Zoomed in plots of λ_{res} vs. laser power for each drop port using the targeted tuning method.

Focused laser tuning: post-etch

After removing approximately 5.36 μm of the SiO_2 cladding using a Plasmatherm RIE etcher, we used a Veeco Dektak 150 surface profilometer to measure the exposed waveguide height which we found to be 100 nm. We then measured the shift for each of the resonators using the same targeted laser tuning method as before. From the results shown in Figure 4.7 we can see that in removing the cladding layer we were able to increase the resonant shift significantly. The average shift for each drop port was found to be 43.3 pm/mW. This increase is likely caused by an increase in the temperature within the target area cause by the decreased ability for heat to

dissipate across the chip without the cladding material. This is due to the reduction in thermal conductivity of an air cladding compared to an oxide cladding which are reported to be 0.0262 W/mK and 1.4 W/mK for the two respective materials.[52,53] The higher thermal conductivities of Si and Si_3N_4 indicate that there will still be some heat dissipation across the chip, largely via the substrate material, but less than is demonstrated before etching the oxide top cladding layer.[54,55]

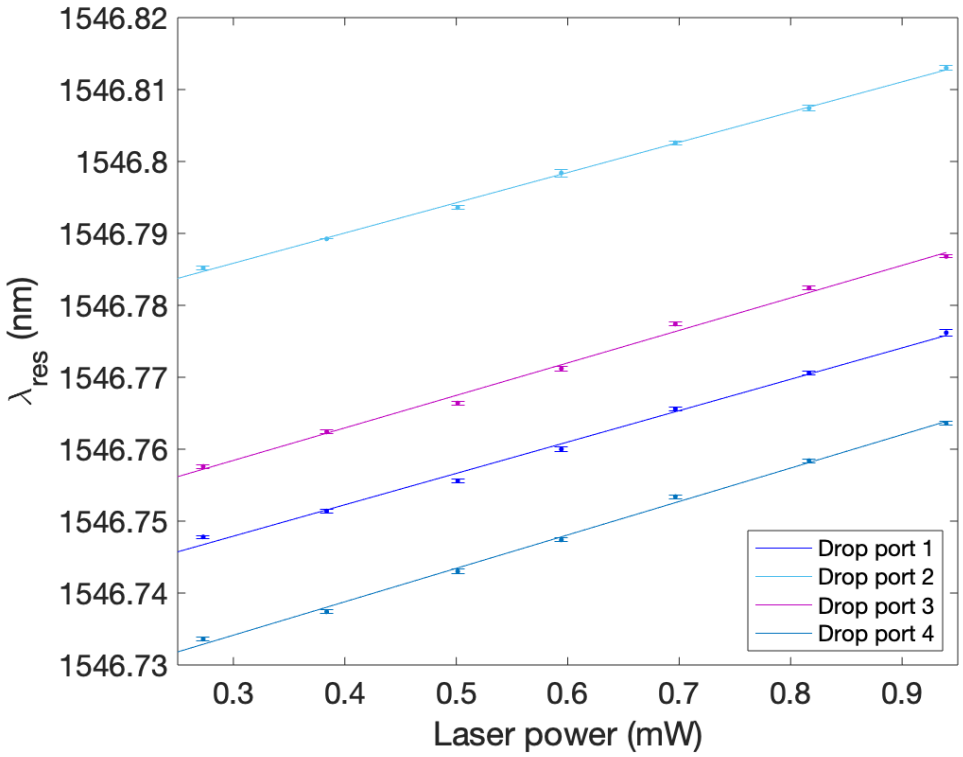

Figure 4.7: Targeted laser tuning of λ_{res} post-oxide etch.

A summary of result for the various tuning methods, both pre- and post-oxide etching can be found in Table 4.1.

Port	Thermal Shift	Laser Shift	Targeted Shift (pre-etch)	Targeted shift (post-etch)
Through port	16 pm/^oC	17.4 pm/mW	NA	NA
Drop port 1	16.3 pm/^oC	17.2 pm/mW	26.6 pm/mW	43.6 pm/mW
Drop port 2	16.1 pm/^oC	6.7 pm/mW	23.7 pm/mW	42.0 pm/mW
Drop port 3	15.9 pm/^oC	15.7 pm/mW	25.6 pm/mW	45.2 pm/mW
Drop port 4	6.4 pm/^oC	16.0 pm/mW	21.8 pm/mW	46.5pm/mW
Chip average	16.1 ± 0.20 pm/^oC	16.6 ± 0.74 pm/mW	24.2 ± 2.1 pm/mW	44.3 ± 1.9 mW

Table 4.1: Summary of the different tuning methods

We measured the Q factor of the rings both before and after etching the cladding layer to show how much this process affected the overall performance of our device. The average initial Q factor for all four of the resonators before etching were measured to be around 2.05×10^4. After etching the Q factor increased slightly to 2.62×10^4. This was not a significant change in Q factor, so we can conclude that the etch process was effective without damaging our device performance. The slight increase that we saw was likely due to smoother side walls created during the etch resulting in lower scattering losses, or a reduction in the bend loss of the rings which can be attributed to larger contrast in indices between the guide and cladding layer.[25]

Thermal isolation

Before etching, the thermal isolation of the chip was demonstrated by measuring the thermal shift in one resonator that resulted from illuminating each of its neighboring resonators with the targeted tuning method at maximum power. These initial measurements indicated that there was very little thermal isolation across the chip owing to the minimal variation in absolute shift when the laser was moved further away from the reference resonator. This is as we expected to see with the oxide cladding layer since it will more easily facilitates the dissipation of heat across a chip than an air cladding will. Since the beam diameter of our laser beam was slightly larger than our ring diameters, it is to be expected that some of the chip will be heated outside just the area of the ring, which will contribute to less thermal isolation. The small area between the resonators, and the efficiency of heat dissipation across the chip is likely the cause of the resonance shift caused by the illumination of neighboring

rings.

After the oxide layer was removed via RIE etching, these measurements were repeated to show the shift in a reference ring from illuminating its neighbors at maximum power. Without the cladding, we measured a notable decrease in the absolute shift in resonance as the beam target was moved away from the reference resonator. The normalization of these pre- and post- etch absolute wavelength shifts with the reference ring's initial absolute shift can be seen below is Figure 4.8.

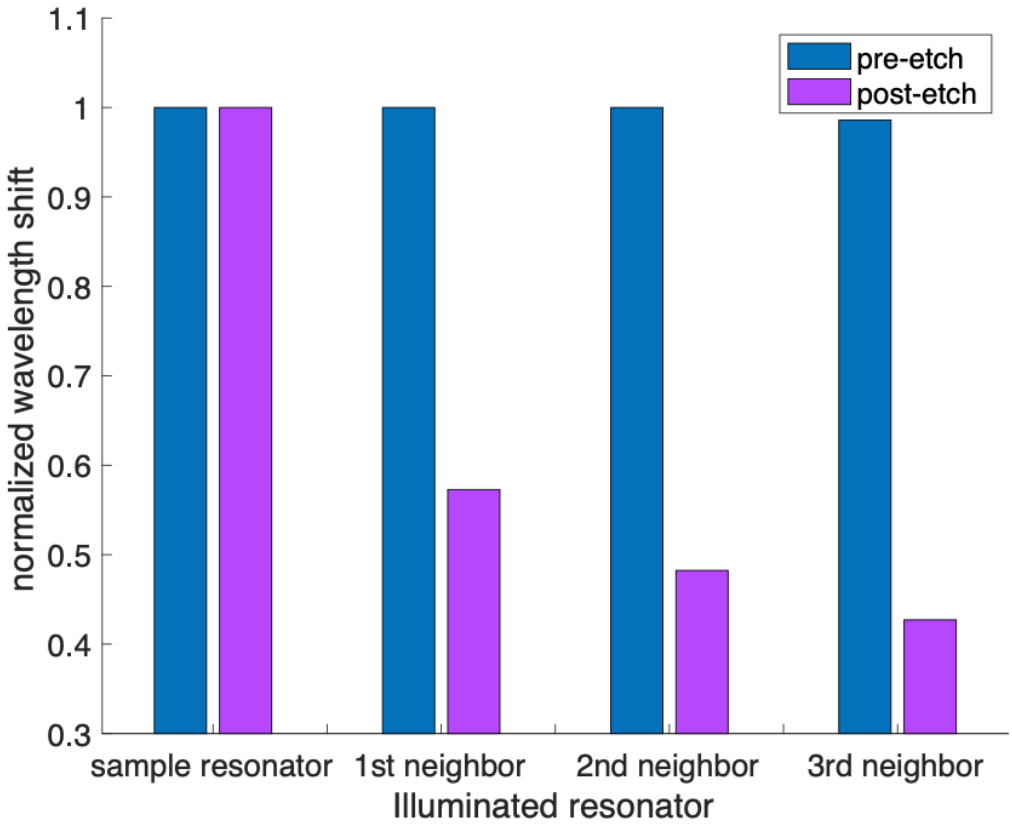

Figure 4.8: Pre- and post-etching λ_{res} shift that occurs relative to the position of the tuning laser.

From this data we can conclude that the thermal isolation of the ring was increased after the oxide material was removed. This data follows the same trend as we would expect to see from a temperature distribution curve in a solid material.[56]

This convinces us further of the impacts of isolating the rings through alternative cladding materials and our ability to thermally isolate and tune a single resonant device on a chip without affecting the performance of nearby devices. These results are consistent with previously demonstrated techniques of etching thermal trenches between on-chip photonic devices as a means to isolate passive components from any heat generated by neighboring active components within the same chip.[57,58,59]

4.4 Conclusion

We have successfully demonstrated the validity of using external short visible wavelength sources to tune integrated microresonator photonic devices. We have shown capabilities of 16.6 pm/mW and up to 44.4 pm/mW with full chip and targeted laser beam tuning methods respectively. We were able to increase the tuning capabilities by etching away the cladding layer and increasing the thermal isolation across the chip while using the targeted tuning method, as well as increasing the overall resonant shift. With these methods, passive photonic devices can be used in active photonic systems without the need for power-inefficient and bulky thermal stages, or intricate fabrication processes of integrating heaters directly onto the chips. The ability to selectively tune devices without need for active components or wire bonding can also improve the economics of large-scale chip manufacturing and characterization.[60]

CHAPTER 5

Magneto-optic materials

In this chapter we will discuss the Faraday effect and the methods of characterizing magneto-optic materials as well as how we have synthesized various nanoparticle composites with tunable magneto-optic responses.

5.1 The Faraday Effect

The magneto-optic Faraday effect, otherwise known as magnetic circular birefringence (MCB), is the rotation of the polarization of linearly polarized light in a medium in the presence of a magnetic field.[61] This is demonstrated below in Figure 5.1. In order to better understand the mechanisms behind this phenomenon, one must first understand the principles of light polarization, dielectric tensors, and indices of refraction. This section covers these concepts as they pertain to this work in their entirety.

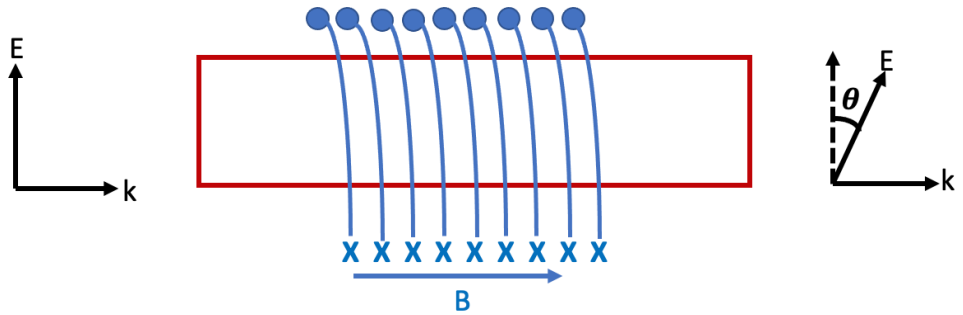

Figure 5.1: The Faraday effect.

5.1.1 Polarization

Light is radiation that takes the form of an electromagnetic wave. The electric and magnetic field components oscillate perpendicular to each other in space.[62] There are many parameters used to describe these waves, such as the amplitude or frequency of oscillation, the direction of propagation defined by the k-vector, and the polarization. The parameter most relevant to understanding the Faraday effect is the polarization.

The polarization of light is defined as the oscillation orientation of the electric field component of an electromagnetic wave.[62] These oscillations are typically described as linear, right-hand circular (RHC), left-hand circular (LHC), elliptically polarized, or unpolarized.[63] For the purposes of this discussion, we will only focus on the linear, RHC and LHC definitions which are represented below in Figure 5.2. These polarization states can be expressed as their own respective Jones vectors as follows:

$$RHC = \frac{1}{\sqrt{2}} \begin{pmatrix} 1 \\ -i \end{pmatrix}, LHC = \frac{1}{\sqrt{2}} \begin{pmatrix} 1 \\ i \end{pmatrix}, Linear = \begin{pmatrix} 1 \\ 0 \end{pmatrix}. \tag{5.1}$$

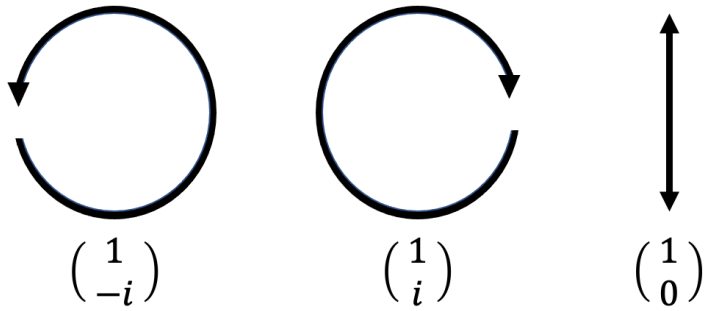

Figure 5.2: RHC, LHC and linear polarization states with their corresponding Jones vectors.

The Faraday effect describes the rotation of linear polarization in a medium that results from applying an external magnetic field to the system that is either

parallel or anti-parallel to the direction of propagation of the light.[61,64] Linearly polarized light can be deconstructed and written as a superposition of RHC and LHC polarized light, as we can see from the Jones vectors in (5.1). When the electric field is oscillating in a circular direction, we know from Maxwell's equations that this will induce a magnetic field either parallel or anti-parallel to the plane of propagation based on the right-hand-rule.[62] When the linearly polarized light passes through a medium where a magnetic field is present, the external magnetic field will either enhance or diminish the initial magnetic field of the two polarizations. This combination of magnetic fields induces a change in the index of refraction with which the two respective polarization states interact. This equal but opposite change in index induces a phase difference between the two polarization states that translates to a rotation of linear polarization when the RHC and LHC polarizations are superimposed. This process can be more thoroughly understood by considering the effects of magnetic fields on the dielectric tensor of a medium.

5.1.2 The dielectric tensor

The dielectric tensor is used to describe how electromagnetic radiation and an external magnetic field will interact within a certain medium.[61] The most generalized dielectric tensor takes the form of

$$\epsilon = \begin{pmatrix} \epsilon_{xx} & \epsilon_{xy} & \epsilon_{xz} \\ \epsilon_{yx} & \epsilon_{yy} & \epsilon_{yz} \\ \epsilon_{zx} & \epsilon_{zy} & \epsilon_{zz} \end{pmatrix}. \tag{5.2}$$

For isotropic media the diagonal elements will be identical, while the rest of the elements will be zero. The application of an external magnetic field induces off diagonal elements $\pm\epsilon'$, so the resulting dielectric tensor in the presence of an external

magnetic field along the z-axis is as follows:

$$\epsilon = \begin{pmatrix} \epsilon_{xx} & \epsilon' & 0 \\ -\epsilon' & \epsilon_{yy} & 0 \\ 0 & 0 & \epsilon_{zz} \end{pmatrix}. \tag{5.3}$$

The induced off-diagonal elements, $\pm\epsilon'$, are directly proportional the applied magnetic field and correspond to changes in the refractive index of the material for LHC and RHC polarizations.[61] This mechanism will be discussed further in the following section.

5.1.3 The refractive index

The complex RI of a material describes how light will pass through a material, if at all.[62,65] The RI is defined by its real and imaginary components:

$$n = n_\epsilon + i\kappa. \tag{5.4}$$

For this definition the real part, n_ϵ, describes the velocity of light as it passes through the medium while the imaginary component κ, determines the absorption of light in the medium.[62,65] For MCB, we exclusively look at the effect the magnetic field has on the real part of the RI. Magnetic circular dichroism (MCD) is the effect of the magnetic field on the imaginary part of the RI which causes the beam to become elliptically polarized beyond just a rotation, though this effect is beyond the scope of this work.[61]

The relationship between the off-diagonal tensor elements and the refractive index is

$$n^\pm = \sqrt{\epsilon \pm i\epsilon'}, \tag{5.5}$$

where the plus and minus correspond to the RHC and LHC polarizations.[61]

The difference in the RI of the two polarizations causes them to propagate at

different velocities through the material which induces a phase difference between the two. This phase change is what accounts for the rotation of linear polarization in the material.[63]

The total amount of rotation is given by the equation

$$\Theta = vBd, \tag{5.6}$$

where d is the length of the material interaction the light experiences, B is the magnitude of the external magnetic field applied along the direction of propagation of light and v is the Verdet constant of the material with units of ^{o}/Tm.[61] The Verdet constant, which can be positive or negative, is wavelength and temperature dependent and intrinsic to the material in question.[66,67]

5.2 Verdet constant characterization methods

The usefulness of integrating our magneto-optic materials with photonic integrated circuits and similar optical systems is dependent on the strength and practicality of their magneto-optic response. In order to reliably develop materials with high performance, we need to ensure we have accurate and dependable methods of characterizing their Verdet constant.

For materials with high Verdet or long interactions lengths, the Verdet constant can be measured by placing the material in a solenoid or a permanent magnet, directing light through crossed polarizers on each end of the material, and then using a power meter to measure the light through the system.[68] This setup can be see below in Figure 5.3. This method works by aligning the polarizers without a magnetic field to ensure both that there is linear polarization in the material and to note the orientation that maximizes the output onto the detector - this orientation will be when the polarizers have the same orientation. When the solenoid or magnet is used to create a magnetic field, the polarization through the second polarizer will

be rotated relative to the off-state and will reduce the transmission as detected by the power meter. The second polarizer can then be rotated until the output is maximized, and this degree of rotation describes the rotation of polarization induced by the magnetic field. Alternatively, instead of maximizing the transmission, it could also be minimized in the on- and off-states, where the degree of difference between the two states still describes the rotation from the magnetic field, or inbetween the maximum and minimum where the intensity is more sensitive to polarization rotation. The equation (5.6) can then be used to determine the Verdet constant from the other known parameters.

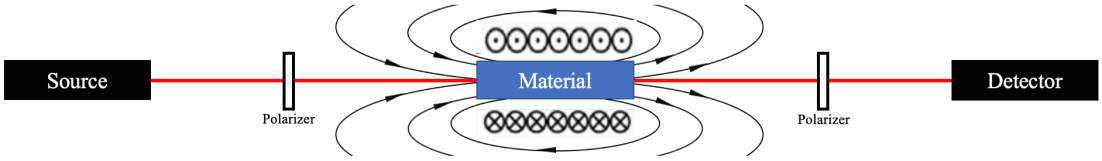

Figure 5.3: Schematic of a cross-polarizer Verdet measurement setup.

Although this method is common and used to characterize the Verdet constant of many materials, it is not reliable when measuring materials with low Verdet constant or small interaction length. At reasonably attainable magnetic fields the degree of rotation from these materials is not long enough to detect using cross polarizers. To solve this problem, we have constructed a differential detection system to measure the Verdet constant of our materials.[69] A schematic of this system is depicted below in Figure 5.4.

The optical path from the laser source passes through a half-wave plate and polarizer to ensure the light is equal parts s and p polarization. This polarized light then reaches a non polarizing beam-splitter (NPBS) where half of the light passes through and the other half is reflected away at 90^o. The transmitted light continues on to the material within the solenoid. A mirror is placed at the back of the material so that the light will be reflected back through the material a second time. This "double-pass" system allows us to double the interaction length of the material, and reduce any reciprocal polarization effects across our measurement system. Since the

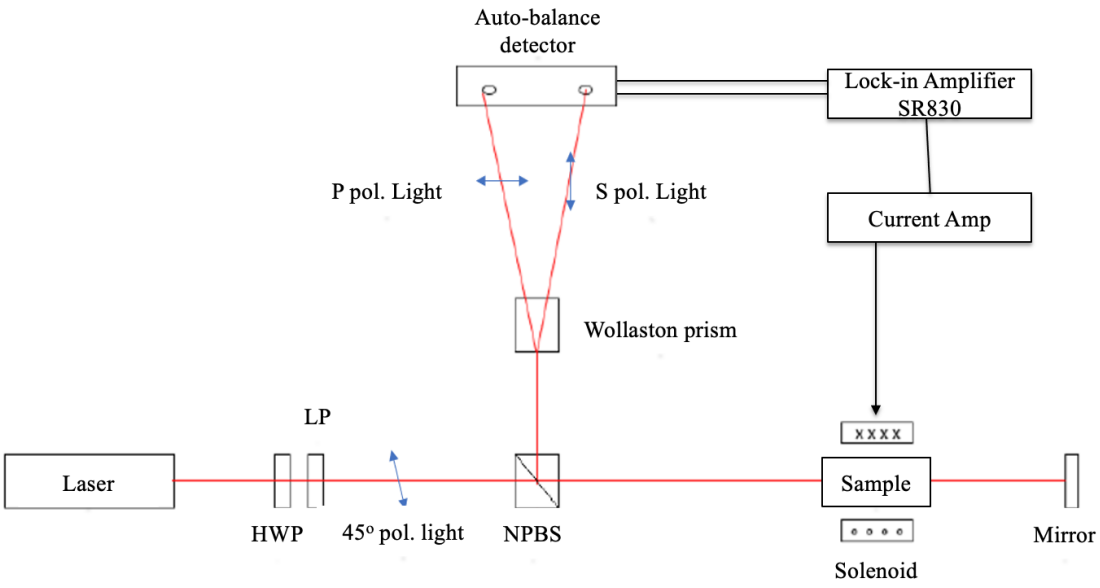

Figure 5.4: Schematic of the differential detection setup used to measure Verdet constants.

Faraday effect is a non-reciprocal optical effect, the light will not be rotated back the same direction, but instead will be rotated twice as much with the second pass. This allows us to detect even smaller Faraday rotations.[61] Once the light has passed through the material and back, it reaches the beam splitter a second time where half of the light is transmitted through, and the other half is reflected at 90^o. The reflected light then passes through a Wollaston prism where the s and p polarizations are separated and guided into the Newport Nirvana 2017 auto-balance detector.[63]

To drive the magnetic field, we used an Stanford research systems SR830 lock-in amplifier paired with a current amplifier and connected it to our solenoid to create an sinusoidal AC magnetic field with adjustable frequency and amplitude. The lock-in amplifier was also connected to the auto-balance detector to ensure the detected signals were driven at the same frequency as the magnetic field. The auto-balance detector's common mode noise cancellation allowed us to detect very small changes ($<1\ \mu^o$) in the difference between our two signals.[70]

When there was no magnetic field present, the s and p polarizations separated

by the Wollaston prism were of equal power since we had set the polarization to be at 45^o, thus creating equal-strength horizontal and vertical polarizations. When a magnetic field was applied and the polarization was rotated, the ratio of s and p polarization changed. This change was detected by the auto-balance detector. As the strength of the magnetic field increased, the ratio between the two polarizations also increased.

The information from the detector was then collected from the lock-in amplifier and analyzed with a script written in MATLAB to calculate the rotation in the polarization. The baseline equation used to calculate this rotation derived from polarmetric math using Jones or Mueller matrices was

$$\theta = \left| \frac{AC}{2DC} \right|, \tag{5.7}$$

where the AC and DC signals are taken from the Nirvana detector, and the absolute value is there to counter the negative sign in the DC voltage that comes from the internal biasing of the detector.[70] However, for our setup this equation is not complete. We must also account for a factor of 2 in the denominator that comes from the s- and p-polarization induced differential detection, as well as another factor of 2 to account for the double-pass nature of our setup. The detector can also be set to increase the signal by either a factor of 10 or 100 which must also be taken in to account. For most of our measurements we only increased the signal by a factor of 10. Finally, we also added in a factor of $\frac{180}{\pi}$ to convert radians to degrees. With all of these considerations our final equation becomes

$$\theta = \frac{180}{\pi} \left| \frac{AC}{80DC} \right|. \tag{5.8}$$

Using (5.8), we used a MATLAB script to plot the rotation of the polarization as a function of the magnetic field strength. The entire MATLAB source code used to calculate these values can be found in Appendix A. By dividing the slope of this plot by the interaction length d from (5.6), we obtained the Verdet constant of the

material.

This method allowed us a reliable and accurate method for characterizing the magneto-optic response of our materials. We used this method to improve the synthesis processes of our materials and target Verdet constant values by controlling material-specific synthesis parameters.

5.3 Magneto-optic material synthesis and optical characterization

Conventional magneto-optic materials such as the ones used in optical isolators are traditionally inorganic garnet materials such as terbium gallium garnet.[71] Although these materials are known for being robust and consistent, they possess fairly low Verdet constants (on the order of 10^3 ^{o}/Tm), and thus require longer interaction lengths to provide adequate extinction ratios for practical applications.[68,72,73] Fabricating these crystals with appropriate thicknesses accounts for much of the manufacturing costs of these magneto-optics devices. In addition, these materials often limit the processing options available and therefore prevent the integration of these materials into fiber-based or integrated phonic devices.

In this work we have developed new methods for fabricating polymer-based materials with cobalt nanoparticles with ultra-high Verdet constant on the order of 10^5 - 10^6 ^{o}/Tm). In the following sections we discuss two methods of high-Verdet constant polymer-based materials with long-term magnetic stability: polymer and magnetic nanoparticle composites, and polymer-coated magnetic nanoparticles.[74,75]

The most common issue in synthesizing high-quality magneto-optic composite materials is in the propensity of aggregation between the nanoparticles. Cobalt nanoparticles are expected to have high magneto-optic responses at C-band wavelengths, but only when they are isolated as nanoparticles. Aggregation of the

nanoparticles in synthesis prevents them from responding as particles, and instead they act as a bulk material, which significantly reduces the Verdet constant of the optical films and increases the scattering and absorption losses.[76] Through novel synthesis methods we attempted to increase and tune the Verdet constant of the materials through particle loading, nanoparticle size, and polymer-coatings.

5.3.1 Cobalt-ferrites

The first synthesis method explored in this research involved exchanging native surface lignands of active OA-$CoFe_2O_4$ nanocrystals with compatible low-molecular weight polymer ligands which are then dispersed in a high molecular weight polymer. The cobalt nanocrystals are synthesised with an oleic acid host polymer. The weight and size of oleic acid prevents quality dispersion of the nanoparticles when processed into optical films. Through ligand exchange, we replaced the oleic acid molecules with low-molecular weight polystyrene-based PS-COOH ligands. The PS ligands are lower in molecular weight, but are also larger molecules than the original oleic acid. These differences allow for better processing of the polymer-based films and better dispersion of nanoparticles into quality optical films. It also allows for higher weight percent loadings of nanoparticles into the high molecular weight host-polymer solution. The details of this material synthesis can be found in Pavlopulous et. al.[74]

Multi-layer film fabrication

The fabrication process for these materials and their resulting magneto-optical characterizations are as follows:

Once the material solutions have been synthesized and formulated (a procedure detailed in N. Pavlopolous et. al.), they can then be fabricated into multi-layer stacks for optical characterization. In order to achieve uniform film thickness, we used the spin-coating method for its simplicity and fast results. Although there are benefits to this method, one drawback is the final film thickness of the materials. Spin-coating typically results in film thicknesses on the order of a few hundred nanometers, up

to a few microns.[35] Although our differential detection offers greater sensitivity in Verdet measurements when compared to alternative methods, the Faraday rotation from a few micron film is not enough to exceed the noise floor of our instrument. For this reason, we created multi-layer stacks of the materials to compound the rotation by increasing the path length.

The samples were spun onto a square cm gold-coated glass slide that served as a mirror. This was to reduce the Faraday rotation that would be measured if we passed the beam through a piece of glass. Even with a low Verdet constant, the thickness of glass as compared to our samples makes it very difficult to reliably account for the additional rotation. The first layer was spun from a stock solution of cellulose acetate at 2700 RPM with an acceleration of 250 RPM/s for 60 seconds. This layer was then dried on a hot plate at 100^{o}C for 2 minutes. Next, the composite was spun at 2000 RPM with an acceleration for 250 RPM/s for 60 seconds, then dried on a hot plate at 100^{o}C for 2 minutes. The cellulose acetate and composite ink were then alternately spun at 2300 RPM and 2000 RPM respectively until the desired number of layers were achieved.[74]

Magneto-optic characterization

Once the films were fabricated, we measured them using the same differential setup described in Section 5.2. The resulting Faraday rotation with nanoparticle weight percent is described in Figure 5.5.

We can see from Figure 5.5, that as we increase the inorganic particle loading, the Faraday rotation increases. This demonstrates our ability to tune the Verdet constant of a material though the loading of magnetic nanoparticles.

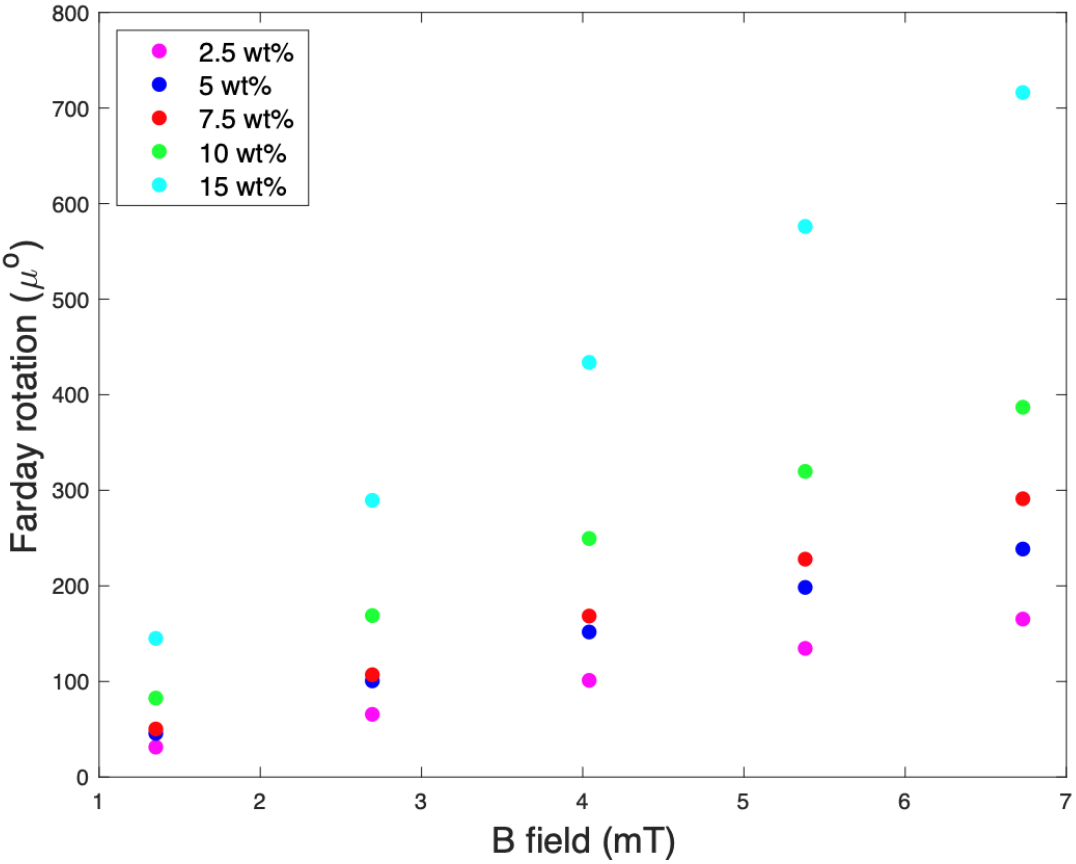

Figure 5.5: Faraday rotation as a function of the magnetic flux density for PS-$CoFe_2O_4$ based materials with varying wt% loadings of $CoFe_2O_4$.

In addition to our ability to tune the magnetic response of materials, we demonstrated the ability to increase the Verdet constant through the ligand exchange of various host polymers. This is demonstrated in Figure 5.6, which shows that by increasing the weight percent loading for nanoparticles with an oleic acid host polymer, the changes in Verdet constant are not as linear, not are they as high in absolute value when compared to the nanoparticles that have been ligand-exchanged with polystyrene.

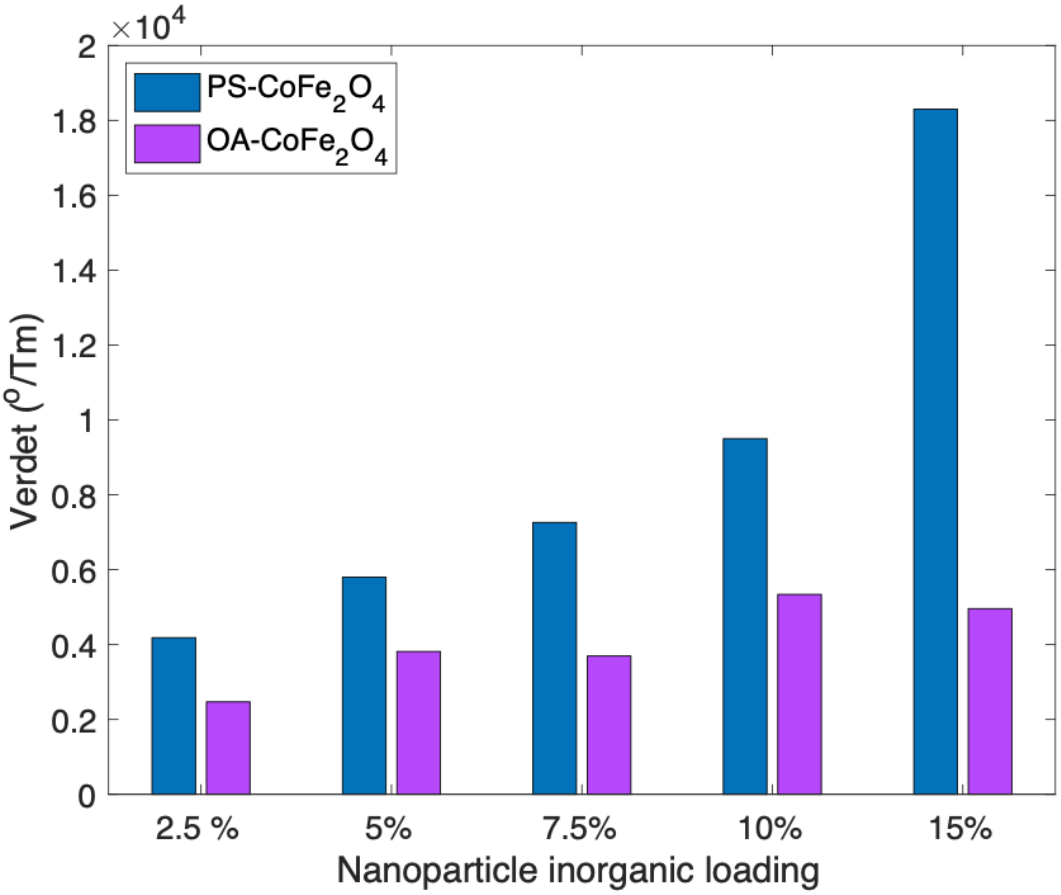

Figure 5.6: Verdet constant values for PS-$CoFe_3O_4$ and oleic acid $CoFe_3O_4$ based composites at the various wt% loadings.

In addition to increasing the Verdet constant by exchanging host polymers and increasing the nanoparticle loadings, we demonstrated the ability to increase the net Faraday rotation by increasing the number of bilayers for our sample. By increasing the number of bilayers of a sample from 5 to 30, we were able to increase the total thickness of the sample by a factor of 5. This is slightly thinner than we would expect from the 6 times increase in bilayers, but we attribute this to the curvature of the spin-coated samples. With this increase in thickness we saw the total Faraday rotation was 1722 μ^o at 740 mT, which was approximately five times greater than we saw for the 5 bilayer sample. These results can be seen in Figure 5.7 This results confirms what we know about the influence interaction length has on the

Faraday effect, and our ability to manipulate our device fabrication to optimize their performance. The trade-off with this technique is that as the number of bilayers is increased, the transmission of the sample decreases which limits out ability to make a sample with thickness larger than tens of microns.

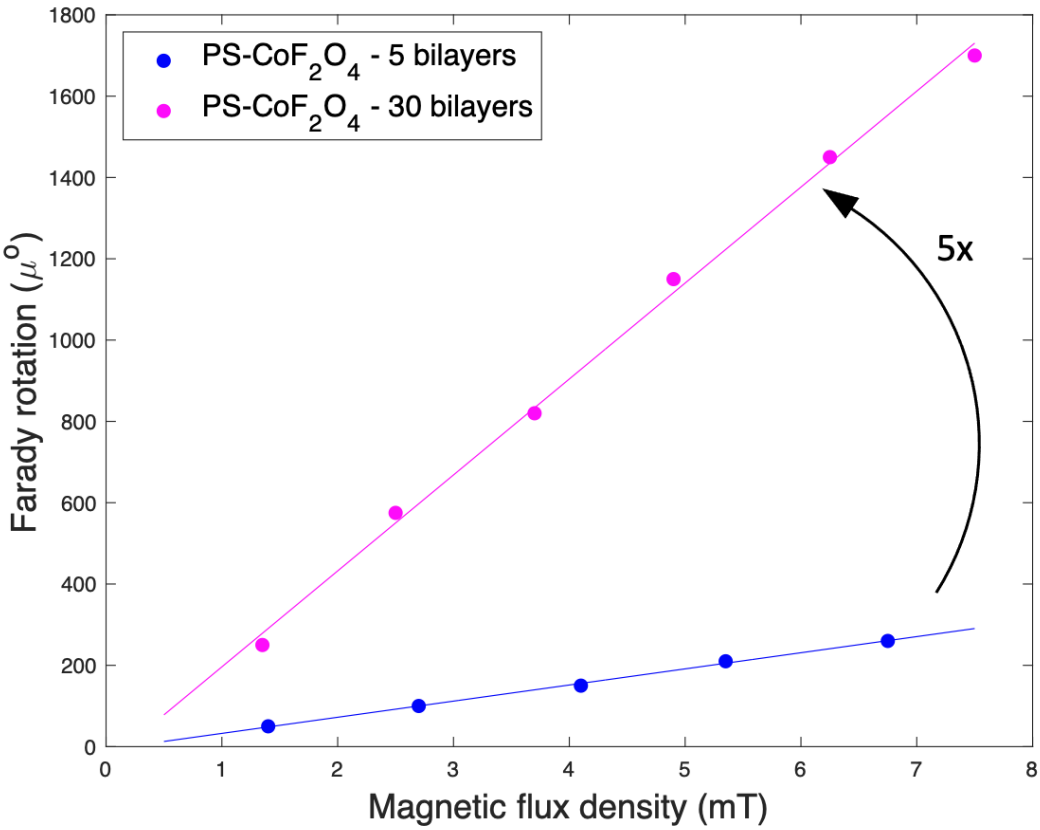

Figure 5.7: Faraday rotation for a 5 and 30 bilayer stacked PS-CoF_2O_4.

Although these results showed progress in our ability to create high-Verdet constant materials with tuneable magnetic response, their Verdet constants were not yet high enough to integrate into optical devices. The low transparency of these materials also hindered their viability to function in optical isolators and other devices that require high optical output in a single direction. Advancing on this method, we discuss in the next section a new generation of materials that work to chip away at these limitations.

5.3.2 Cobalt nanoparticles

The second generation of materials was made from polymer-coated magnetic cobalt nanopartcles. The cobalt nanoparticles were synthesized with a polystyrene host polymer. By starting this synthesis with a polystyrene polymer instead of oleic acid as we had previously done, we reduced the number of processing steps required to achieve good particle dispersion and low aggregation. These polymer-coated nanoparticels were then dispersed in a high molecular weight PS-COOH solution. The larger size of the polystyrene as compared to oleic acid allowed us to disperse the particles into thin films as well as bulk pellets for free-standing applications. The synthesis with polystyrene also allows us to synthesize larger nanoparticles than our previous materials which dramatically increased the magneto-optic response without sacrificing as much transparency due to the decrease in particle aggregation. The previous $CoFe_2$ materials were limited in size to about 5 nm, where the Cobalt nanoparticles in polystyrene have tunable size from 9 nm to 17 nm and greater. These syntehsis processes are detailed in Carothers et al.[75]

With these new nanoparticles, we are able to tune the magnetic response by controlling the particle loading, as well as the nanoparticle size. We have explored loading of 5, 10, 15, 30 and 50 %, and nanoparticle sizes of 9 nm, 14 nm, and 17 nm. The fabrication and characterization of these materials are discussed below.

Multi-layer film and free-standing pellet fabrication

The layered structures were fabricated in a manner similar to the previous materials where a polyvinyl alcohol solution and the composite inks were alternately spun on a gold-coated glass slide at 2000 RPM for 2 minutes and then dried on a hot plate at 150^{o}C for 2 minutes. This was repeated until there were 6 layers of polyvinyl alcohol and 5 layers of nanoparticle composite ink layers.

Following the procedure detailed in Carothers et al, a homogeneous solution of free polystyrene and PS-Co nanoparticles was synthesized and dried to be pressed

into pellet samples for free-standing characterization of a bulk material. The dried polymer-nanoparticle composite was then broke into pellets. These smaller samples were then hot-pressed between two Kapton film release layers. The samples was pressed at 150^{o}C for several minutes before the pressure was increased to 1T and held at this pressure for 10 minutes. The resulting pellets were approximately 0.1 mm in thickness. The sample was then released and ready for characterization.

Magneto-optic characterization

In addition to determining the Verdet constants of these materials, we used a Cary 5000 UV-Vis spectrometer to measure the transmission of the samples at 1310 nm for various weight percent loadings for the three different particle sizes. These results are shown in Figure 5.8 for films nominally 3 μm thick. These values indicate that the transmission of our samples is inversely proportional to particle loading.

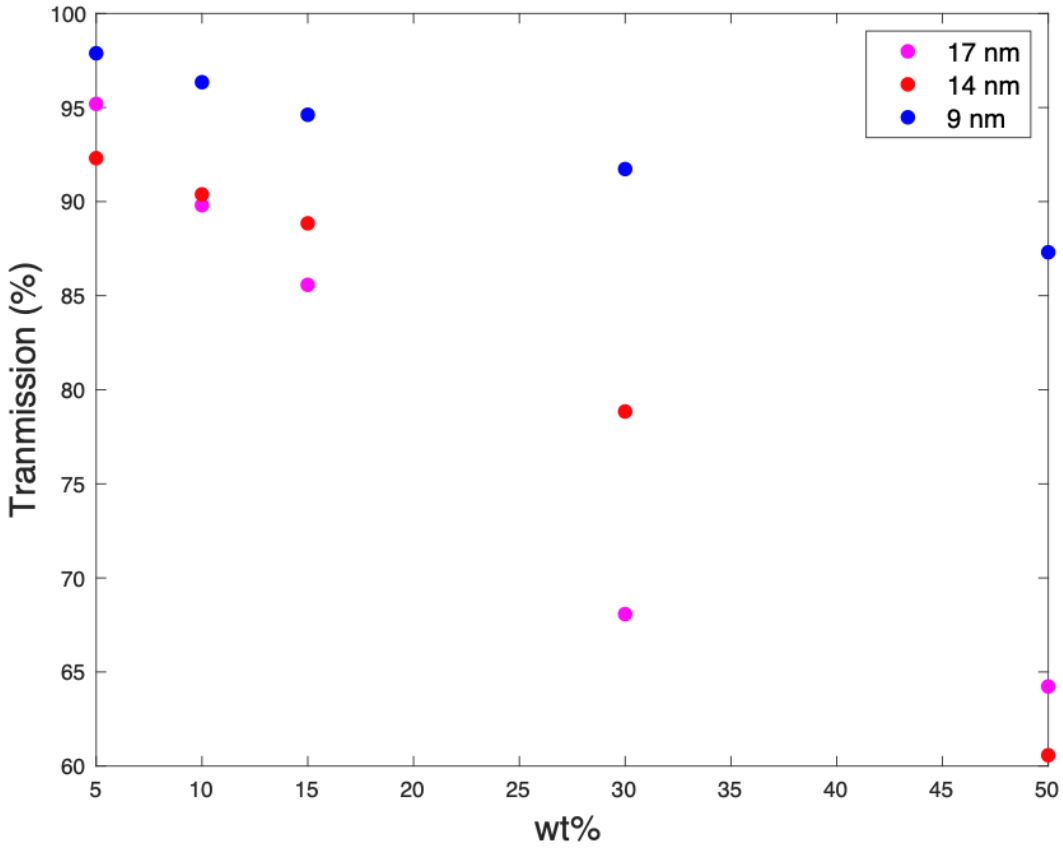

Figure 5.8: Transmission of 1310 nm light for the 9 nm, 14 nm, and 17 nm particle sizes at various wt% loadings with nominal thicknesses of 3 μm.

The Verdet constant of these materials was characterized by the same differential detection method described in Section 5.2. The Faraday rotation for increasing particle loadings is summarized in Figures 5.9, 5.10 and 5.11 for the 9 nm, 14 nm and 17 nm particle sizes respectively, where the error in each measurement is negligible.

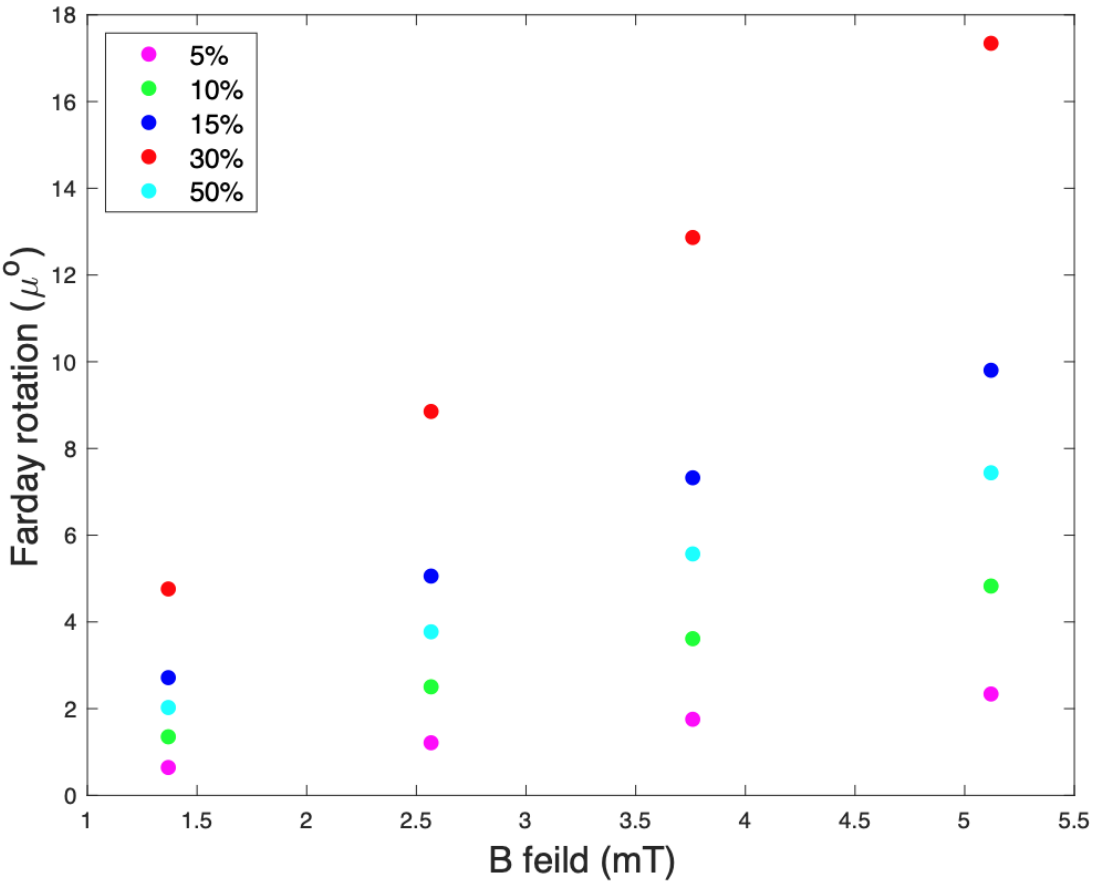

Figure 5.9: Faraday rotation measurements for the 9 nm particle size at 5, 10, 15, 30 and 50 percent particle loadings.

As we can see from these results, there is a direct effect on the Verdet constant by increasing the particle loading of our materials, although this effect is not always linear. In Figure 5.12 we can see that the Verdet constant increases with particle loading, but only to a certain point. We believe that the reduction of Verdet constant beyond 40% results from aggregation of nanoparticles that caused Mie scattering effects in the materials. The aggregations of nanoparticles made it such that the increase in scattering reduced the area within the materials that could contribute to the overall Faraday rotation, thus reducing the Verdet constant.

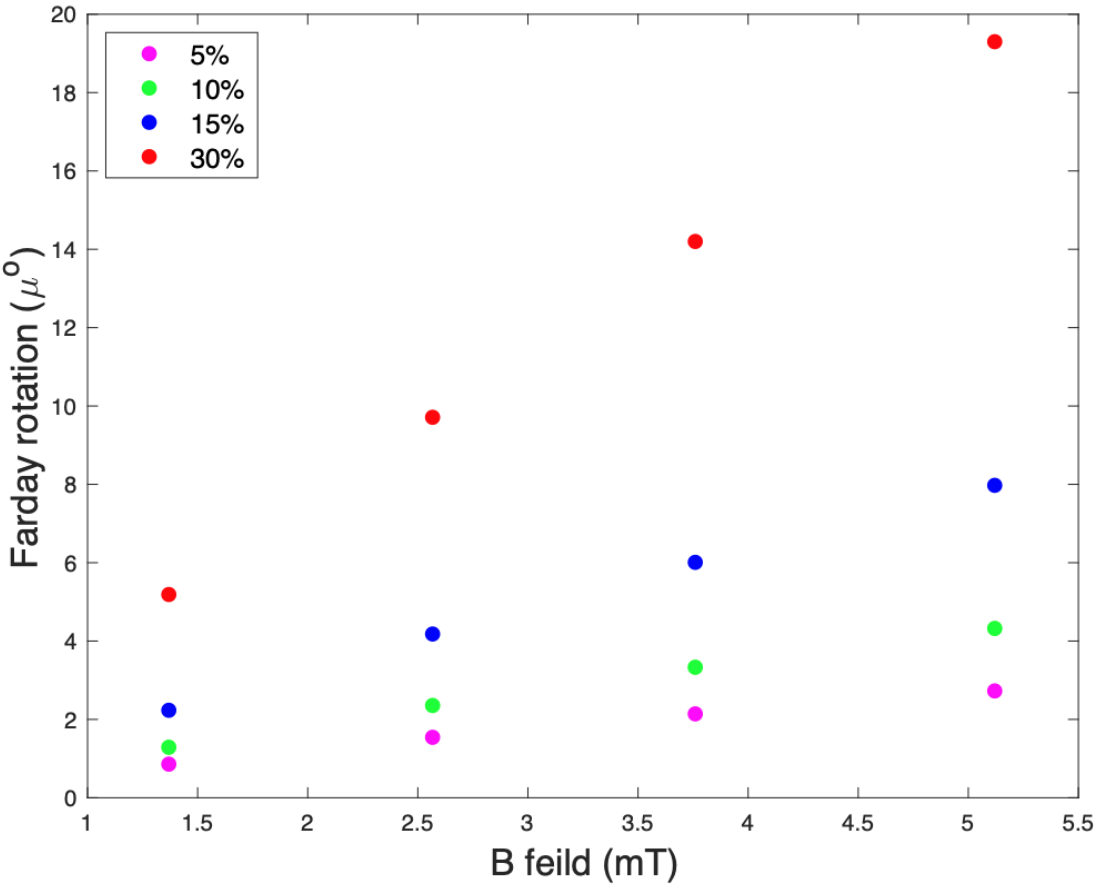

Figure 5.10: Faraday rotation measurements for the 14 nm particle size at 5, 10, 15, and 30 percent particle loadings.

In addition to multilayered films meant for optical characterization purposes, we also characterized the viability of fabricating these materials into bulk devices that could be used in optical isolators. To test this, we used a setup similar to that depicted in Figure 5.3 found in Section 5.2. These pellet samples were made from nanoparticle composite inks of 2.3, 5.3 and 12.3 weight percent. The transmission of these samples for wavelengths ranging from 600 nm to 1800 nm are depicted below in Figure 5.13. From this we can see that the 2.3 wt% samples has a transmission at 1310 nm of about 10%, and the higher loadings have even lower transmission at the same wavelength. This limits their viability to operate in a functional isolator, but it is hopeful in demonstrating our ability to dramatically increase the total Faraday

rotation of our devices.

This measurement method was the same as depicted in Figure 5.3 using a 0.1 T permanent magnet and two Glan-Thompson polarizers. It demonstrated optical rotations of -0.67^o and -1.08^o for the 2.3 wt% and 5.3 wt% respectively. The 12.3wt% sample did not offer high enough transmission to be able to accurately detect the Faraday rotation.

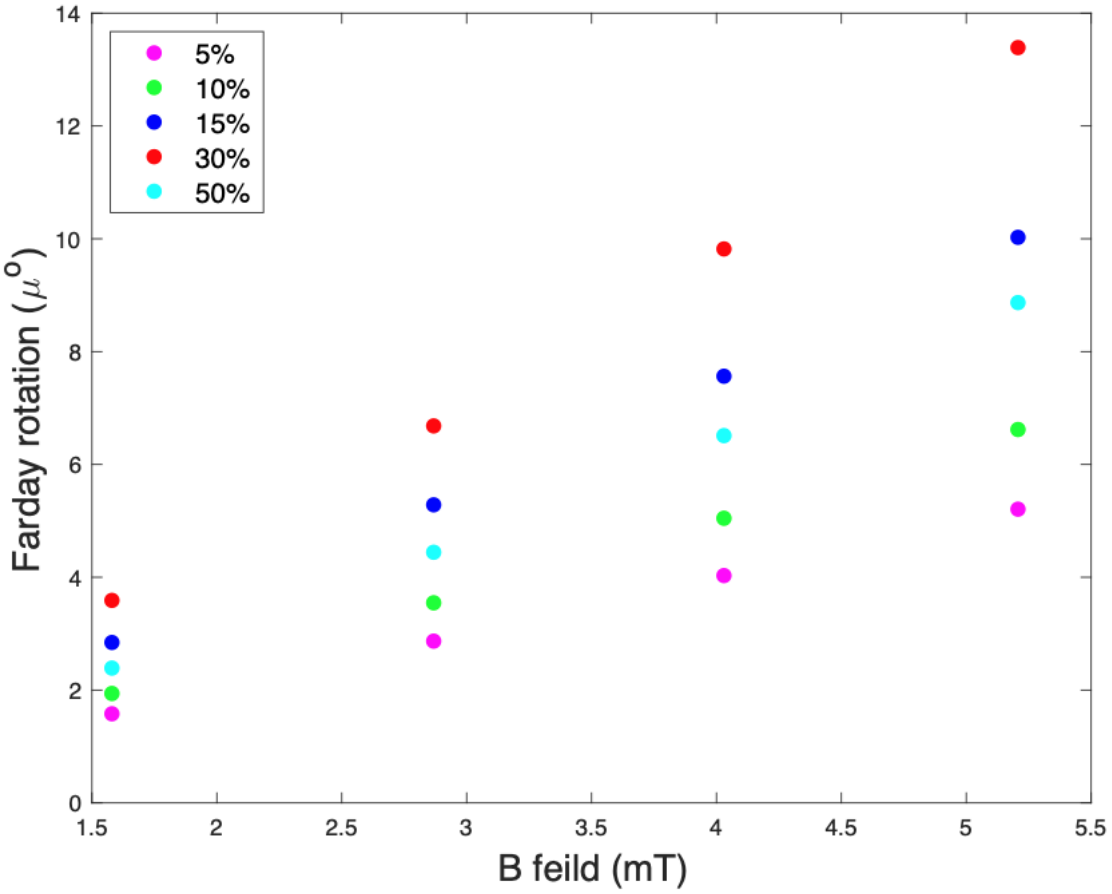

Figure 5.11: Faraday rotation measurements for the 17 nm particle size at 5, 10, 15, and 30 percent particle loadings.

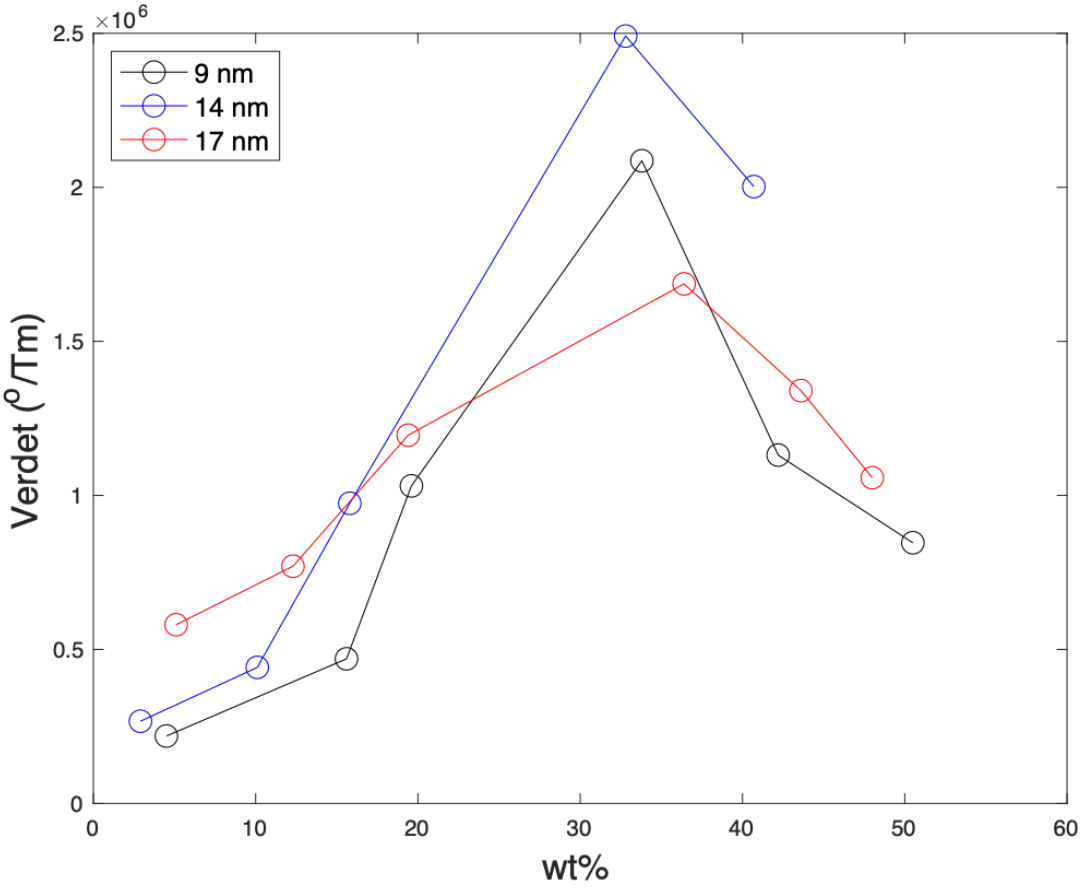

Figure 5.12: The Verdet constant of the three nanoparticle sizes at increasing wt% loadings.

Since the magnetic field, the Faraday rotation and the sample thicknesses are known, we can calculate the Verdet constant of these samples using (5.6). For these free-standing films, the Verdet constant was calculated to be 6.9×10^4 and 1.2×10^5 ^{o}/Tm for the 2.3 and 5.3 wt% loadings respectively. These values are lower than what we would extrapolate from the layered films based on sample thickness. We attribute this lower Verdet to likely aggregation that occurred when blending PS-Co nanoparticles with linear PS.[76]

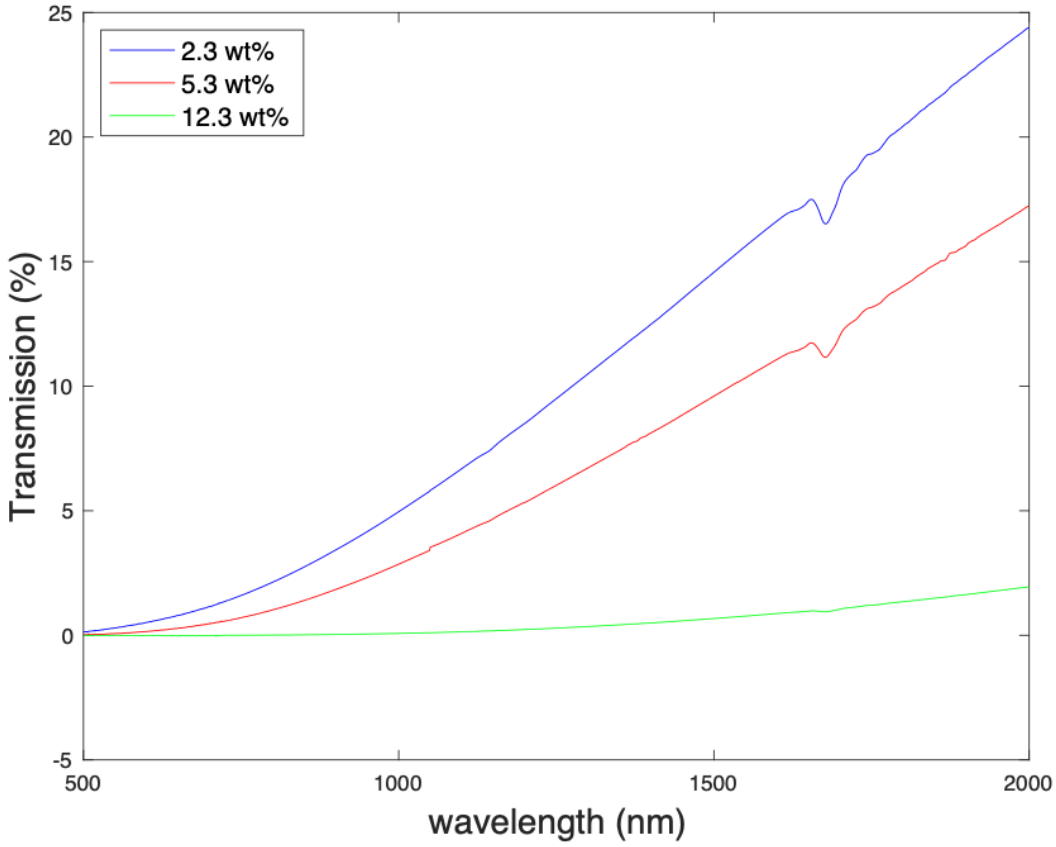

Figure 5.13: Optical transmission of the free-standing polymer-coated cobalt nanoparticle pellet samples for 2.3, 5.3 and 12.3 wt% particle loadings.

5.4 Conclusion

Although there are limitations to these materials, we have successfully demonstrated ultra-high Verdet constants for polymer based thin films, and demonstrated single-digit degree rotation for bulk polymer-coated nanoparticle composite materials. With Verdet constants easily attainable on the order of 10^6 ^{o}/Tm that have low synthesizing costs and large interacting lengths, these materials introduce new pathways for integrated magneto-optic devices and low-cost optical isolators and high-frequency modulators.[77,78]

CHAPTER 6

Magneto-optic modulator

6.1 Optical modulators

To understand more about the applications and performance of our magneto-optic modulators, it is best to understand current electro-optic amplitude modulator designs and performance measures so that we can compare our current and future devices to their industry competitors.

Silicon photonics is one of the leading candidates for meeting the required performance metrics necessary to accommodate the increasing use of network interconnects.[79] Two of the main electro-optic (EO) modulator designs are the Mach-Zehnder EO modulators and active ring resonator modulators.[80,81,82]

6.1.1 Current modulator device concepts

Both of these modulator designs operate through electro-optics effects that either change the real or imaginary components of the refractive index of the EO material.[83] Recall from (5.4) that the real and imaginary components of the refractive index correspond to the refraction and absorption of the material[65]. For these reasons, when an applied electric field changes the real part of the RI, this device is classified as an electro-refractive device, and when it affects the imaginary component it is classified as an electro-absorptive device. These changes are typically caused by changing the concentration of free-charges in the silicon, a mechanism known as the plasma dispersion effect. Soref and Bennett experimentally determined the relationship between the concentration of electrons and holes in silicon and the

resulting changes in refractive index and absorption at 1.55 μm. These relationships are denoted by the equations:

$$\Delta n = -5.4 \times 10^{-22}(\Delta N)^{1.011} - 1.53 \times 10^{-18} \times (\Delta P)^{0.838)} \tag{6.1}$$

$$\Delta\alpha = 10log_{10}exp^{-8.88\times10^{-21}(\Delta N)^{1.167}-5.84\times10^{-20}(\Delta P)^{1.109}}, \tag{6.2}$$

where Δn and $\Delta\alpha$ are the changes in refractive index and absorption that result from changes in the free-electron and free-hole concentrations, denoted by ΔN and ΔP respectively.[83,84]

The modulation of an optical signal via EO-induced absorption is simple in that if the absorption increases, the output signal of the device decreases.[85] This mechanism can be used to effectively modulate the signal with high enough extinction ratio to produce binary code to transfer data.

Modulation of an optical signal via changes in the refractive index is less straightforward, but still relatively simple. The two main options for modulation via refractive index changes are Mach-Zehnder and resonators modulators.[86] A Mach-Zehnder interferometer can be used to achieve EO modulation by changing the relative phase shift of an optical signal propagating in one arm versus the other such that the two waves destructively interfere when superimposed and diminish the optical output signal[87]. In the second modulator design, using a resonant structure, the resonant wavelength of the device shifts with a change in the refractive index of the resonator. This allows us to shift between an on- and off-resonance states for a given wavelength position.[88] These Mach-Zehnder and resonator device design mechanisms are illustrated in Figures 6.1 and 6.2 respectively.

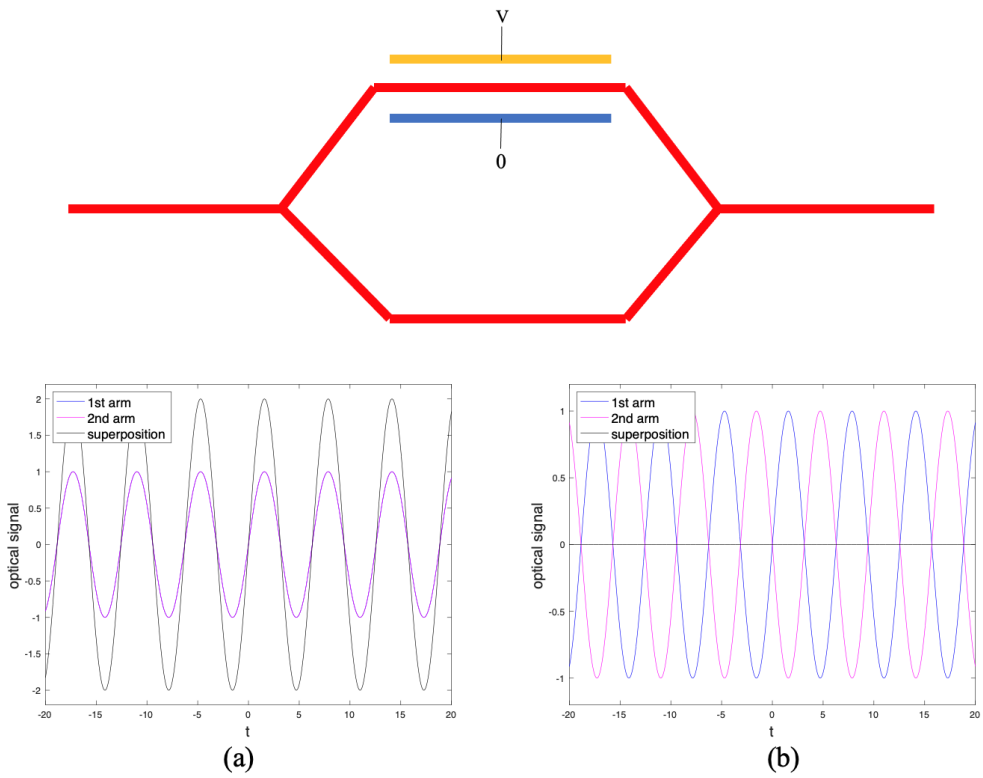

Figure 6.1: Mach-Zehnder EO modulator in the (a) on- and (b) off-state.

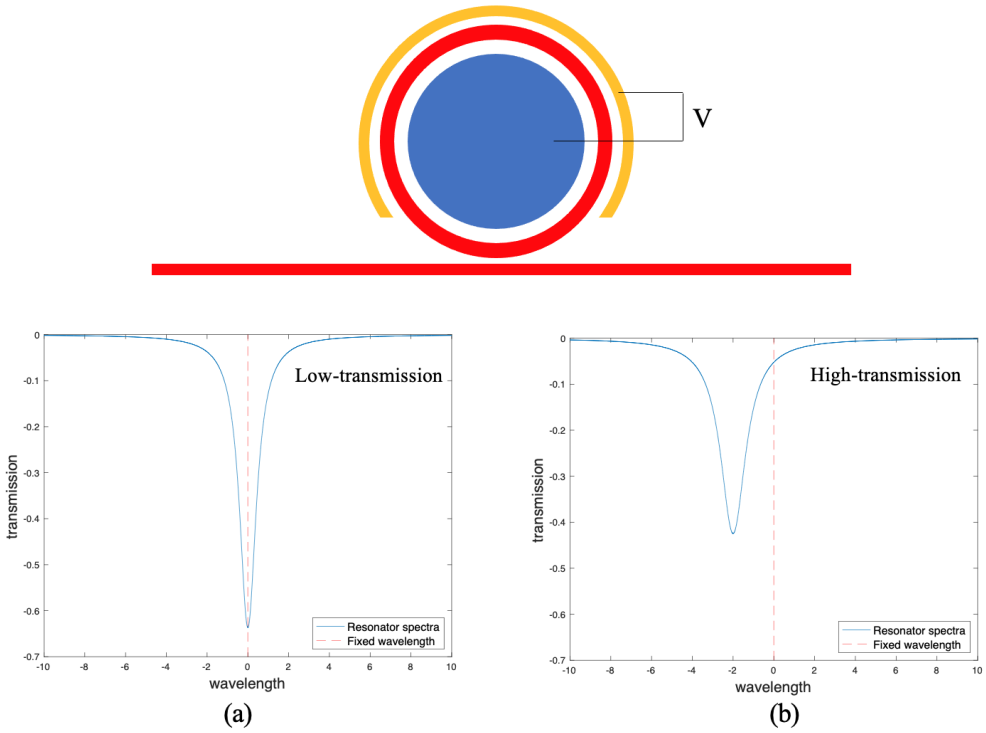

Figure 6.2: Resonator EO modulator mechanism for the (a) off- and (b) on-state.

6.1.2 Modulator characteristics

There are several characteristics used to determine the efficacy and efficiency of optical modulators including speed, extinction ratio and power consumption. Other parameters are used to characterize modulators, but for this work we will focus on just these metrics.

The modulation speed is one of the most important metrics used to determine the potential of applications for a modulator. The bandwidth is defined as the frequency at which the modulation contrast is half of its maximum value.[89] The higher the frequency of operation, the more data a modulator can transmit in a system in a given time period. For telecommunication applications, speeds in the multi gigahertz are required, but for other applications such as sensing, moderate modulation speeds are sufficient.

The extinction ratio (ER), otherwise known as the modulation depth, of a modulator is the ratio between the maximum intensity output (I_{max}) and the minimum intensity output (I_{min}) of the modulated signal.[90] This ratio is generally expressed in units of dB via the equation

$$ER = 10 * log_{10}(I_{max}/I_{min}). \tag{6.3}$$

A higher ER corresponds to lower bit error rates and higher receiver sensitivity. For these reasons a larger ER is more useful for long distance data transmission applications. Generally an ER of >7 is preferred, although ERs from 4-5 are often sufficient for most telecommunication applications.[79,91]

The power consumption of a modulator is one of the most important metrics in determining the usability of a modulation circuit. The power consumption, sometimes expressed as the energy per bit, is the energy used to produce a single bit of data. This metric includes the energy required to operate the optical and electrical components of the modulator.[79] The obvious trade-off with many emerging modulator designs is the increase in power consumption that comes with an increase in the speed and ER of the modulator. These must be balanced in order to justify any increase in power consumption with a compensating increase in bit rates. This is perhaps one the greatest limiting factors in current modulator innovations.

Our magneto-optic modulator design functions as an amplitude modulator that we hope can soon operate at high speeds with large ER for applications ranging from data communications to field sensing.

6.2 Magneto-optic modulator design

This modulator design integrates magneto-optic polymers with silicon nitride photonic devices. As covered previously in Section 5.1, the Faraday effect is the rotation of light polarization in the presence of a magnetic field. Additionally, in Subsection

2.2.4 we noted that a change in polarization can change the resonance and Q factor of a resonator. Through use of these two mechanisms we have demonstrated preliminary operation of a magneto-optic amplitude modulator. This device was fabricated using a low-loss silicon nitride microring resonator purchased from the Ligentech foundry. The SiO_2 cladding material was etched away and replaced with a magneto-optic polymer, such as those described in Chapter 5. The resonant nature of the device increases the path length of our light interacting with the material, and the MO polymer rotates the light to a polarization state that is not supported by the resonator. This rotation then translates to loss in the device which can be modulated to produce binary signals for telecommunications. The basic concept of this design is illustrated in Figures 6.3 and 6.4. The resonance spectrum is deep when the modulator is in the off-state and there is no magnetic field applied. When the magnetic field is present, the Q factor is reduced and the transmission at the resonant wavelength increases due to the shortening and broadening of the resonant spectrum.

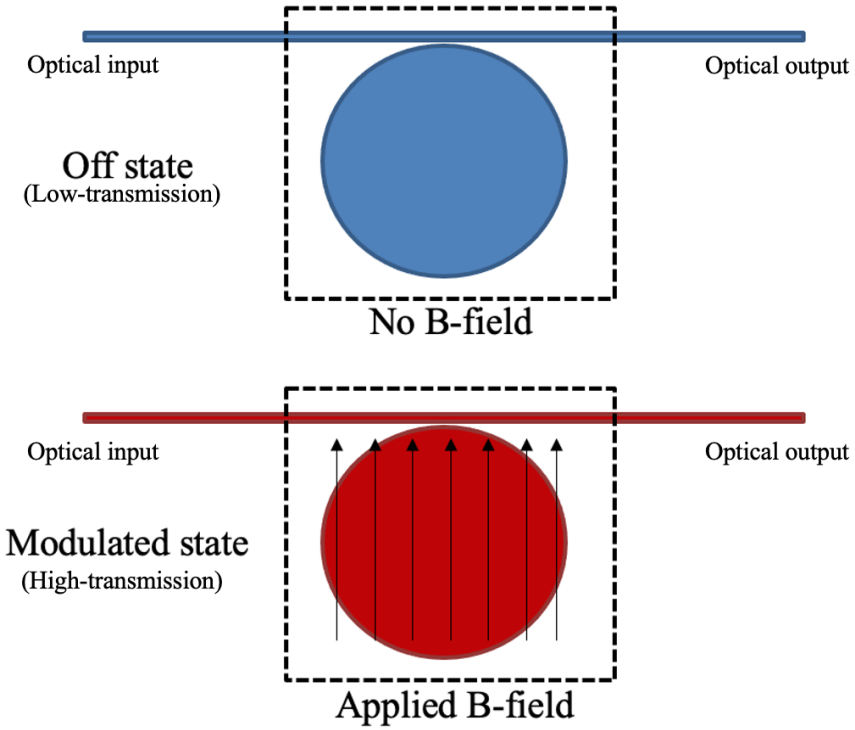

Figure 6.3: Demonstration of the off and on state of the magneto optic modulator.

The performance of this device is dependent on the quality of the resonator, and the materials used. The higher the Q factor of the resonator, the more time the light will spend traveling along the length of the ring.[26] Longer interaction lengths mean greater Faraday rotation, as we have seen from (5.6). Thus we can conclude that the contrasts in our modulated signals will be directly related to the resonator quality.

Additionally, the materials used for the device greatly affect its performance depending on the indices, absorption and magneto-optic response of the materials. Since we know from Section 2.1.4 that the core, cladding and substrate materials directly affect the effective index, and subsequently the mode confinement of a waveguide or resonator, we know that we must choose our materials and dimensions very carefully. If we choose materials that offer a high effective index and greater mode confinement, then we know that the mode interaction with the cladding materials

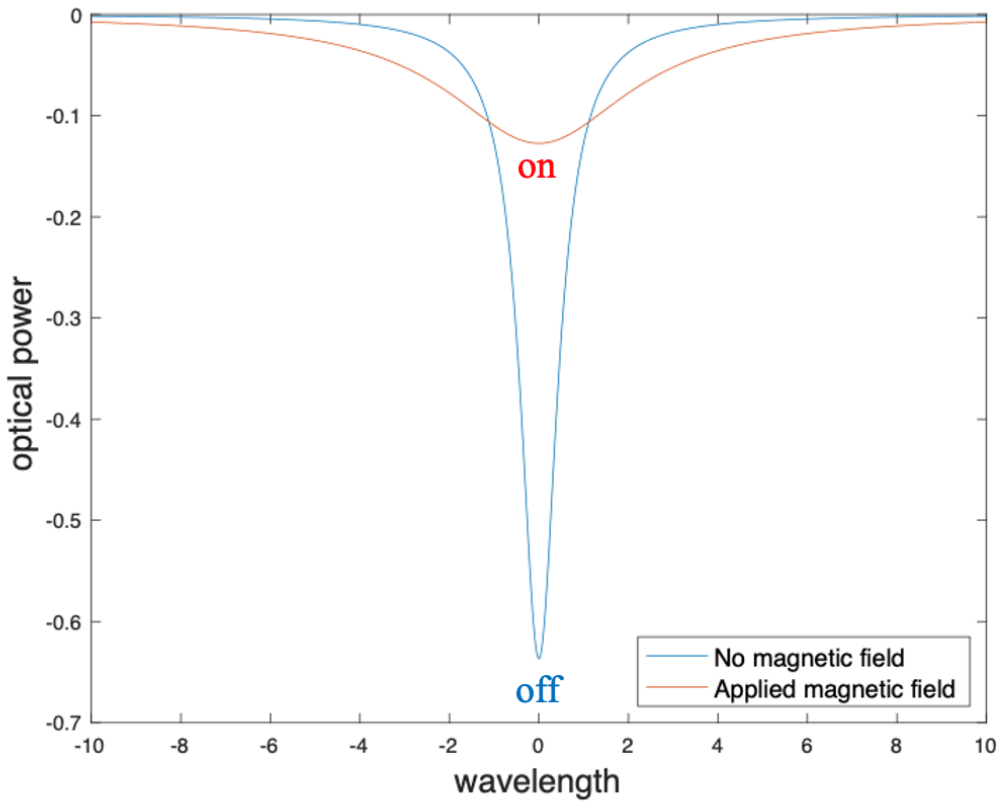

Figure 6.4: Representation of the resonant spectra of our MO modulator in the on- and off-state. These axis values are not representative of real optical resonator spectra.

will be reduced, resulting in less Faraday rotation and lower extinction capabilities of the modulated signal. However, if the effective index is too low then the mode will not be well-guided and will suffer high loss, especially radiation loss as it propagates along the circumference of the microring. This increase in baseline loss could be enough to reduce the efficacy of the modulator when interacting with a magnetic field.

For the same reason we want to limit mode loss from radiation, the material absorption of our core and cladding materials is crucial for fabricating a useful device. Most commercially available or easily manufactured waveguides and resonators will have either Si or Si_3N_4 core materials. Both of these materials are low-loss for tele-

com wavelengths, so our main concern is the material absorption from our cladding. We have shown is Section 5.3.2 that as we increase the particle loadings in our materials, we also increase the optical absorption. Since increasing the particle loading is also how we increase the Verdet constant of the material, we need to balance the two to optimize the magneto-optic response of the device as well as the strength of the signal output.

A complete preliminary analysis of this MO modulator concept design can be found in Appendix B. The device fabrication including the most appropriate material choice are discussed in the following section.

6.3 Device fabrication

In its original state, this device had a Q factor of 2.2 million - far greater than we were able to achieve in-house. The high Q factor and nitride material made this device a great candidate for our modulator. High Q factors allow us longer lengths to interact with our magneto-optic materials, and the lower index of Si_3N_4 as opposed to Si decreases the effective index of the device and results in more mode interaction with the cladding materials.[19,4]

Simulations were conducted in FIMMWAVE to show the percentage of mode confinement in the MO cladding material for varying cladding thicknesses. For these simulations we assumed the index of the MO material to be 1.58. The cladding was simulated from 0 to 1300 nm where the increase in thickness corresponds to further etching of the SiO_2 material from the top of the device. Since the Si_3N_4 waveguides and rings are 800 nm, the cladding thickness touches the top of the waveguide at 500 nm. A schematic of the varying cladding thickness with respect to the waveguide structure is shown in Figure 6.5.

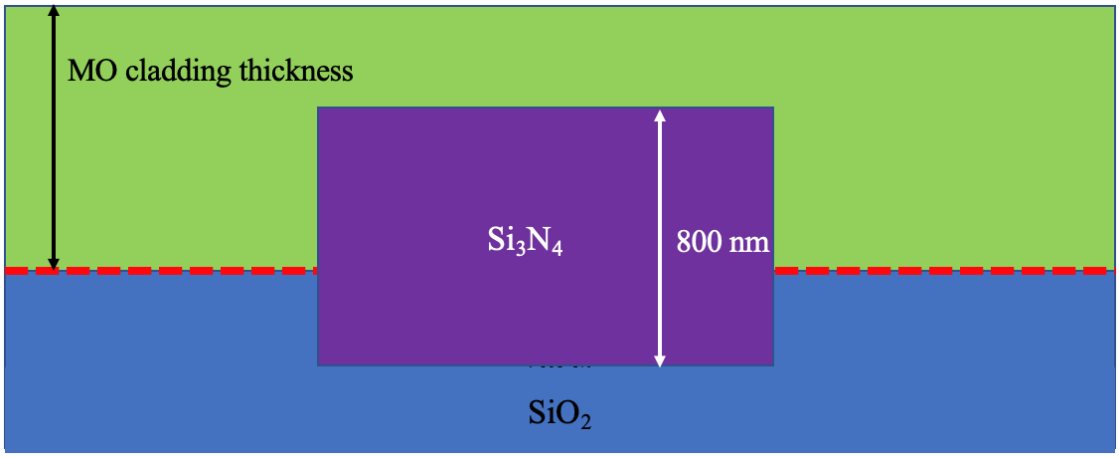

Figure 6.5: Waveguide and cladding dimensions used in our FIMMWAVE simulations.

The simulations results in Figure 6.6 show that the percentage of mode confinement exponentially increases as the cladding material approaches the top of the waveguide structure, increases more as the SiO_2 sidewalls are reduced and begins to level off as the cladding fully surrounds the waveguide core. This assures us that even without etching past the surface of the waveguide, we can still achieve almost 10% mode interaction with the cladding material.

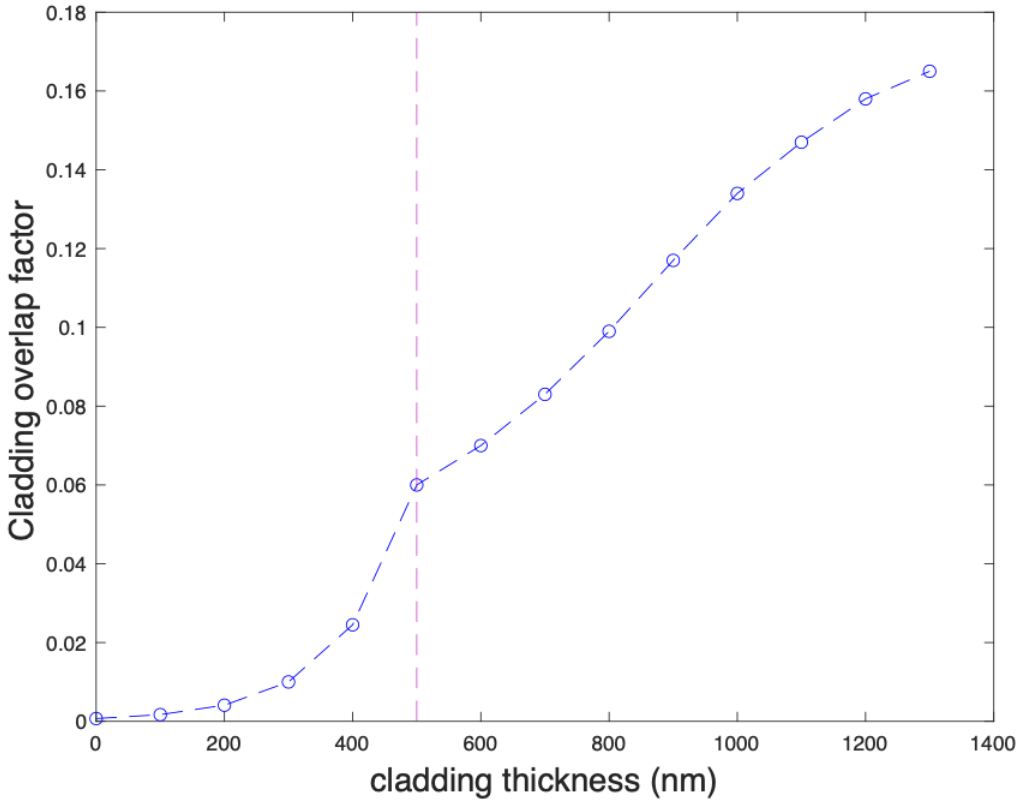

Figure 6.6: Simulated overlap factor in the cladding material for varying cladding thicknesses.

After etching away the initial SiO_2 cladding material using a Plasmatherm Versaline DSE III reactive ion etcher, we were able to deposit the magneto-optic cladding. Through this process we removed enough cladding to expose 100 nm at the top of the nitride resonator to air, which as we have seen from Figure 6.6, allows us to assume roughly 7% mode interaction with the cladding material.

After removing the top cladding, a layer of our polymer-coated magnetic nanoparticle film was spin coated onto the exposed resonator. The samples synthesized and documented here we fabricated with an ink of 2.5 wt% particles loadings of 14 nm cobalt nanoparticles.[75] The film was spun at 1000 rpm for 2 minutes and then dried on a hot plate at 150^{o}C for four minutes to remove any remaining solvent.

The resulting film thickness was 3.5 μm.

The step-by-step fabrication process is illustrated below in Figure 6.7.

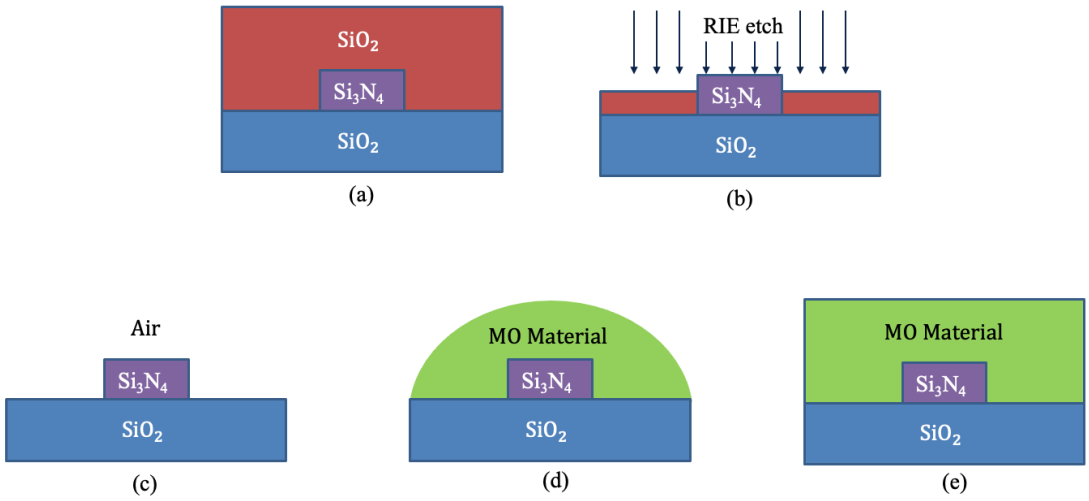

Figure 6.7: Step-by-step fabrication process of the MO modulator beginning with the whole chip (a), the RIE etch (b), the bare core device (c), the MO ink deposition (d) and the final device structure post spin-coating (e).

This fabrication method can be tailored to tune the performance of future modulators by choosing a baseline resonator with varying Q factors, changing the etch depth and core exposure of the device, and through material selection.

6.4 Modulator characterization

This device was characterized using standard fiber-to-chip-to-fiber butt coupling techniques. An Agilent 8164A tunable laser was guided through a polarization controller and coupled into the bus waveguide of the fully fabricated modulator device. The output signal from the through port of the resonator bus waveguide was coupled into a second optical fiber and connected to a fiber-coupled Newport multi-function optical meter.

The Q factor was measured by scanning the tunable laser across the resonance spectrum where the output power was recorded at each wavelength. From this

information the resonant wavelength and the FWHM of the resonance could be determined. The Q factor was calculated using (2.42).

For the magnetic response measurements, the same fiber and chip setup was used connecting the tunable laser to the optical power meter. A 10 mT permanent magnet was oriented along the resonator to elicit the change in output power at different wavelength positions. A schematic of this setup is shown in Figure 6.8.

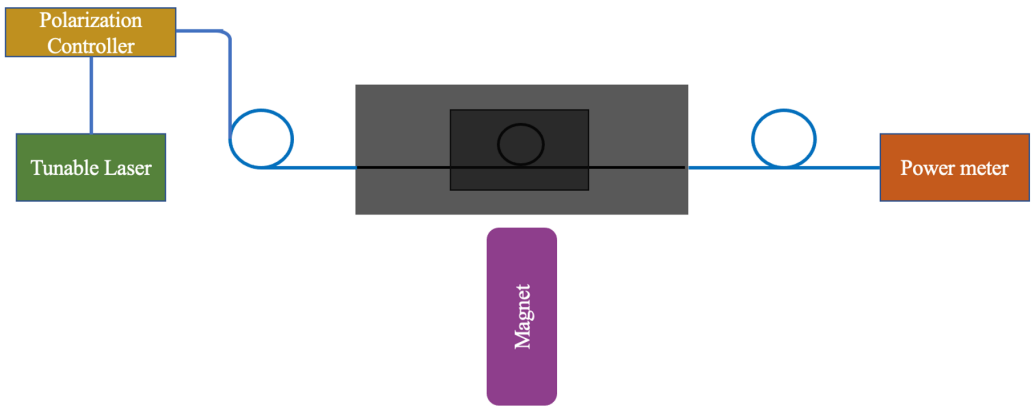

Figure 6.8: Schematic of the MO modulator characterization setup.

To measure the magneto-optic response, we scanned the tunable laser without an external magnetic field present, until it was positioned on the peak resonant wavelength and measured the output power in dBm (P_{dBm}), which is related to the power in mW (P_{mW}) by the equation[20]

$$P_{dBm} = 10 * log_{10}(P_{mW}/1mW). \tag{6.4}$$

We remeasured the power after applying our external magnetic field. The difference between the two values was taken to be the extinction ratio of the modulator. This measurement was repeated for a wavelength just off-resonance (shifted approximately 0.0002 nm), the FWHM of the resonance, and completely off-resonance. We repeated this measurement for two separate fully fabricated modulators with

resonance spectra of varying depth. These results are discussed in the following section.

6.5 Modulator extinction ratio measurements

The extinction ratios (ER) for a high-functioning and low-functioning modulator device were measured for various wavelength positions in response to a 10 mT static magnetic field. The results for the two modulators can be seen in Tables 6.1 and 6.2.

λ (nm)	0T B-field	10mT B-field	ER
1552.6367	-14.6 dBm	-12.7 dBm	1.9 dB
1552.6365	-13.8 dBm	-12.1 dBm	1.7 dB
1552.6357	-10.83 dBm	-9.72 dBm	1.11 dB
1552.6227	-5.82 dBm	-5.82 dBm	0 dB

Table 6.1: ER for the MO modulator using a low-performance Si_3N_4 resonator.

λ (nm)	0T B-field	10mT B-field	ER
1552.7011	-24.75 dBm	-20 dBm	4.75 dB
1552.7009	-22.24 dBm	-17.84 dBm	4.4 dB
1552.7004	-17.58 dBm	-14.9 dBm	2.68 dB
1552.6974	-12.09 dBm	-12.08 dBm	0.01 dB

Table 6.2: ER for the MO modulator using a high-performance Si_3N_4 resonator.

From these results, we have demonstrated an ER up to 4.75 dB with our magneto-optic modulator design. To better depict the ER trend with wavelength

position, the ERs are shown in Figure 6.9 for the different relative wavelength positions.

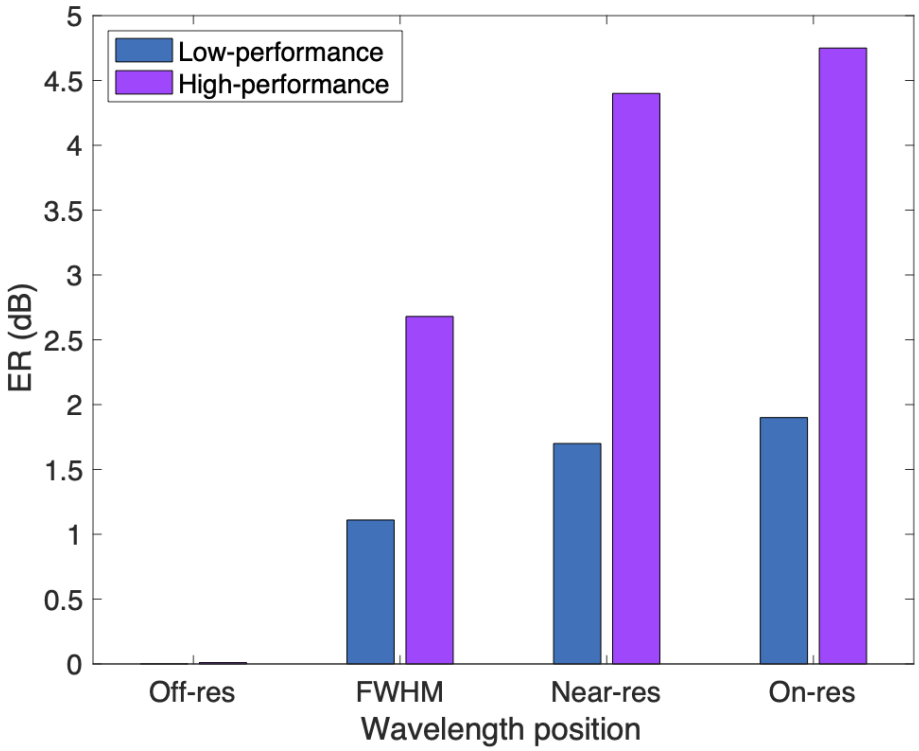

Figure 6.9: Extinction ratios for the varying wavelength position for high and low performance MO modulators.

From this we can see that the ER is reduced as we move the wavelength away from its peak resonance position; this is as we would expect. These results follow the same trend we would expect to see from our prediction of what should happen to the resonator spectra as we introduce an external magnetic field. From our depictions in Figure 6.4 we would expect that the ER when the wavelength is near the peak resonant wavelength would be greater than for wavelengths further from resonance. Both of these modulators successfully demonstrate this concept.

The variance in ER between these two modulators comes from the difference in the baseline output spectra of the resonator. One trade-off that we often see in resonator devices is that in order to achieve a high Q factor, the depth of the

resonant spectra must be small. This comes from the coupling constant of our device and the propensity for light to couple in an out of the resonator. Although both resonators showed the same trend with wavelength, we were able to achieve higher ER with the high-performance resonator because the depth of the resonant dip was greater than that of the low-performance modulator. From this contrast we can conclude that our modulator ER performance is dependent and limited by the depth of the device's resonance spectra.

6.6 Conclusions and outlook

Although the results highlighted in this work are not comprehensive, they do demonstrate our ability to successfully integrate magneto-optic polymers with Si_3N_4 photonic devices with variable performance demonstration. This has been a goal of researchers for more than ten years, and these results are very promising for successful continued research on integrated magneto-optic modulators with modulation speeds up to 1 GHz with low energy per bit rates.[92]

Further directions for this work include studying the effects that magnetic field strength, particle loadings and nanoparticle size of our magneto-optic polymer materials have on the performance of our modulators, and how the Q factor and material selection of the optical resonator contribute to their overall performance as magneto-optic modulators. Additionally, alternative device designs may optimize the magneto-optic response of such devices by increasing the interaction length of the magnetic field by orienting the field along the path of the resonators, or stretching the resonator to travel longer in a certain direction. This second approach is especially applicable for differential magnetometer detection systems that look to emphasize signals in certain axes over others.

APPENDIX A

MATLAB source code: Verdet constant calculations

Matlab source code for the verdet constant calculations developed and expanded on by various members of the Norwood, Peyghambarian and Pyun labs at the University of Arizona from 2016 to 2020.

```
%%%%%%%MATLAB CODE FOR FARADAY ROTATION AND ASSOCIATED DATA%%%%%%%%%
clc
pause on
diary on
format longE

%%%%%%%%%%%%%%TEXT BOXES WAITING TO BE ENABLED AND ...
    TESTED%%%%%%%%%%%%%%%%%
temp = inputdlg({'Enter Base File Name (Everything Except ...
    Voltage Designation)'},'basename');
[basename]=temp{:};

%------FILL IN FIELDS ...
    BELOW-----------------------------------------%
name = basename;
filepath = 'This PC';

Solenoid_Voltage = ['voltage'];
B = ['B field'];
```

```
17
18 Counts_per_measurement = 10;
19 L = ['path length'];
20
21 %-----------------------------START:DONT ...
       MODIFY---------------------------%
22 %-------------------------Parameter ...
       Setup---------------------------------%
23 prefix = name;
24 magfieldname = [name ' Magnetic Field Calibration'];
25 fileBase = name;
26 txtExtension = '.txt';
27 xlxextension = '.xlsx';
28 SampleName = name;
29
30 List_of_Files = dir([name,'*.txt']);
31 Number_of_Files=length(List_of_Files);
32
33 if Number_of_Files>1
34
35 txtname = [name ' Compiled.txt'];
36 xlsxname = [name ' Compiled.xlsx'];
37
38 A = zeros(1,1000);
39 diary(txtname)
40 for idx = 1 : length(StartingVoltage_Increment_EndingVoltage_mV)
41     filename1 = [prefix, ...
          num2str(StartingVoltage_Increment_EndingVoltage_mV(idx)), ...
          '.txt'];
42     delimiterIn = ',';
43     headerlinesIn = 1;
44     A = importdata(filename1,delimiterIn,headerlinesIn);
45     disp(A.data)
46     diary(txtname)
47 end
48
```

```
49 fileID = fopen(txtname);
50 data = textscan(fileID,'%f%f%f%f%f%f','Delimiter',' ...
       ','MultipleDelimsAsOne',1);
51 data   = [num2cell([data{2:end},data{1}])] ;
52 fclose(fileID);
53 xlswrite(xlsxname, data) ;
54 fileName = [xlsxname];
55
56 Signal_AC = xlsread(fileName,'F:F');
57 AUX3_DC = xlsread(fileName,'C:C');
58 Aux1 = xlsread(fileName,'B:B');
59 V = xlsread(fileName,'E:E');
60
61 %%%%%%%%%%%%%%%%%%%%%%%%ELSE IF FOR SINGLE ...
       FILES%%%%%%%%%%%%%%%%%%%%%%%%%%%%%%%%
62 elseif Number_of_Files≤1
63
64 txtname = [name '.txt'];
65 xlsxname = [name '.xlsx'];
66
67 buffer = fileread(txtname) ;
68 data   = textscan(buffer, '%s %f %f %f %f %f %f', 'delimiter', ...
       ',','headerlines',1);
69 data   = [data{1}, num2cell([data{2:end}])] ;
70 xlswrite(xlsxname, data) ;
71 fileName = [xlsxname];
72 Signal_AC = xlsread(fileName,'B:B');
73 AUX3_DC = xlsread(fileName,'E:E');
74 Aux1 = xlsread(fileName,'D:D');
75 V = xlsread(fileName,'G:G');
76
77 %%%%%%%%%%%%%%%%END IF LOOP FOR # of ...
       FILES%%%%%%%%%%%%%%%%%%%%%%%%%%%%%%%%%%%%
78 end
79 %%%%%%%%%%%%%%%%END IF LOOP FOR # of ...
       FILES%%%%%%%%%%%%%%%%%%%%%%%%%%%%%%%%%%%%
```

```
80
81  count = length(Signal_AC) / Counts_per_measurement;
82
83  Signal_AC = reshape(Signal_AC,Counts_per_measurement,[]);
84  AUX3_DC = reshape(AUX3_DC,Counts_per_measurement,[]);
85  Aux1 = reshape(Aux1,Counts_per_measurement,[]);
86
87  AVG_Signal_AC = mean(Signal_AC);
88  AVG_DC_Aux3 = mean(AUX3_DC);
89
90  STD_AC = std(Signal_AC);
91  STD_DC = std(AUX3_DC);
92
93  AVG_Signal_AC_ZeroFieldCorrected = AVG_Signal_AC - AVG_Signal_AC(1);
94
95  %------------End of Parameter ...
        Setup----------------------------------%
96
97  AVG_Theta_ZeroFieldCorrected = 180 / pi * ...
        AVG_Signal_AC_ZeroFieldCorrected ./ (-2 * 2 *2* 10 .* ...
        AVG_DC_Aux3);
98  AVG_Theta_ZeroFieldCorrected(1) = [];
99  p = polyfit(B,AVG_Theta_ZeroFieldCorrected,1);
100 PointbyPoint_AC_ZeroFieldCorrected = Signal_AC - AVG_Signal_AC(1);
101
102 PointbyPoint_Theta_ZeroFieldCorrected = 180 / pi * ...
        PointbyPoint_AC_ZeroFieldCorrected ./ (-2 *2 *2 *10 .* AUX3_DC);
103
104 PointbyPoint_Theta_ZeroFieldCorrected(1) = [];
105 q = polyfit(Solenoid_Voltage,B,1);
106 Mag_Calib = q(1);
107
108     scatter(Solenoid_Voltage,B,60,'Marker','o','Markerfacecolor','b')
109     plot(Solenoid_Voltage,B,'-k','LineWidth',2)
110     xlabel('Solenoid Voltage (V)','fontsize',15)
111     ylabel('Measured Field (mT)','fontsize',15)
```

```
112     title({'Mag. Field Calibration', sprintf('%d mT/V',Mag_Calib)})
113     grid on
114     saveas(gcf,magfieldname,'png')
115
116 B_m = Mag_Calib .* V;
117
118 B_m(1)=[];
119     subplot (3,2,2)
120     scatter(B_m,PointbyPoint_Theta_ZeroFieldCorrected,25, ...
            'Marker','o','Markerfacecolor','b')
121
122     ylabel('Rotation (degree)','fontsize',15)
123     title({'Rotation vs. Field (All Data)'})
124     grid on
125
126 Aux1(1)=[];
127
128    subplot (3,2,6)
129    scatter(B_m,Aux1,25,'Marker','o','Markerfacecolor','y')
130    xlabel('Magnetic Field (mT)','fontsize',15)
131    ylabel('Aux1 (V)','fontsize',15)
132    title({'Aux1 vs. Field (All Data)'})
133    grid on
134
135 AUX3_DC(1)=[];
136
137    subplot (3,2,3)
138    scatter(B_m,AUX3_DC,25,'Marker','o','Markerfacecolor','k')
139    hold on
140    ylabel('Aux3 (V)','fontsize',15)
141    title({'Aux3 vs. Field (All Data)'})
142    grid on
143
144 PointbyPoint_AC_ZeroFieldCorrected(1)=[];
145 Signal_AC(1)=[];
146
```

```
147     subplot (3,2,4)
148     scatter(B_m,PointbyPoint_AC_ZeroFieldCorrected,25, ...
            'Marker','o','Markerfacecolor','r')
149
150     ylabel('Signal (V)','fontsize',15)
151     title({'Signal vs. Field (All Data)'})
152     grid on
153
154 S2A3 = PointbyPoint_AC_ZeroFieldCorrected ./ AUX3_DC;
155 S2A3_non_ZeroFieldCorrected = Signal_AC ./ AUX3_DC;
156
157     subplot (3,2,5)
158     scatter(B_m,S2A3,25,'Marker','o','Markerfacecolor','g')
159
160     xlabel('Magnetic Field (mT)','fontsize',15)
161     ylabel('Signal/Aux3 (A.U.)','fontsize',15)
162     title({'Signal/Aux3 vs. Field (All Data)'})
163     grid on
164
165 Verdet_C =  p(1) * 10^3 / (L);
166
167 ThetaAVG_Calc = p(1) * B + p(2);
168
169
170      subplot(3,2,1)
171      scatter(B,AVG_Theta_ZeroFieldCorrected,60, ...
             'Marker','o','Markerfacecolor','r')
172      hold on
173      plot(B,ThetaAVG_Calc,'-k','LineWidth',2)
174      ylabel('Rotation (Degree)','fontsize',15)
175      title({'Rotation vs Field (Averaged)',  sprintf('V = %d ...
             deg/Tm',Verdet_C)});
176      grid on
177
178
179 suptitle(SampleName)
```

APPENDIX B

Magneto-optic modulator concept design

In this appendix we will discuss the preliminary concept design for a magneto-optic modulator fabricated from novel polymer-based magneto-optic materials and silicon disk resonators. The full justifications for this concept design as well as its limitations will be presented here for consideration.

We believe a silicon or silicon nitride microdisk resonator with a magneto-optic material cladding can operate as an amplitude modulator under the right conditions. The magnetic field interaction with the MO material will cause a rotation in the polarization of light in the resonator, increasing the absorption of the system and decreasing the Q factor of the resonator. By determining the relationship between the magnetic field and the change in Q factor, we have determined how well this system can modulate optical signals, and how to achieve a field strength strong enough to achieve this modulation.

B.1 Q factor and loss in optical resonators

The transmission spectrum of a disk resonator can be represented as a Lorentzian with a maximum at the resonant wavelength. The Lorentzian equation is given by

$$L = \frac{1}{\pi} \frac{1/2\Gamma}{(x - x_0)^2 + (1/2\Gamma)^2}, \tag{B.1}$$

where Γ is the width of the Lorentzian, and x_0 is the resonant wavelength. The resonant wavelength divided by the FWHM of the Lorentzian gives the Q factor of the resonator.[93] We have shown how a change in the width affects the transmission spectra of the resonator, as demonstrated below in Figure B.1. For these calculations we assumed an initial width varying from 1 to 25, and a centered wavelength of 1. These values are not representative of microresonators that would be used in experimental applications, they are merely placeholders used to show a general relationship trend. Additionally, we calculated Q factor or each Lorentzian, using the equation

$$Q = \frac{\lambda_{res}}{\Delta\lambda_{FWHM}}, \tag{B.2}$$

where λ_{res} is the resonant wavelength and $\Delta\lambda_{FWHM}$ is the full-width half-max of the resonance peak.[26] The relationship between the Lorentzian width and the Q factor is shown in Figure B.2.

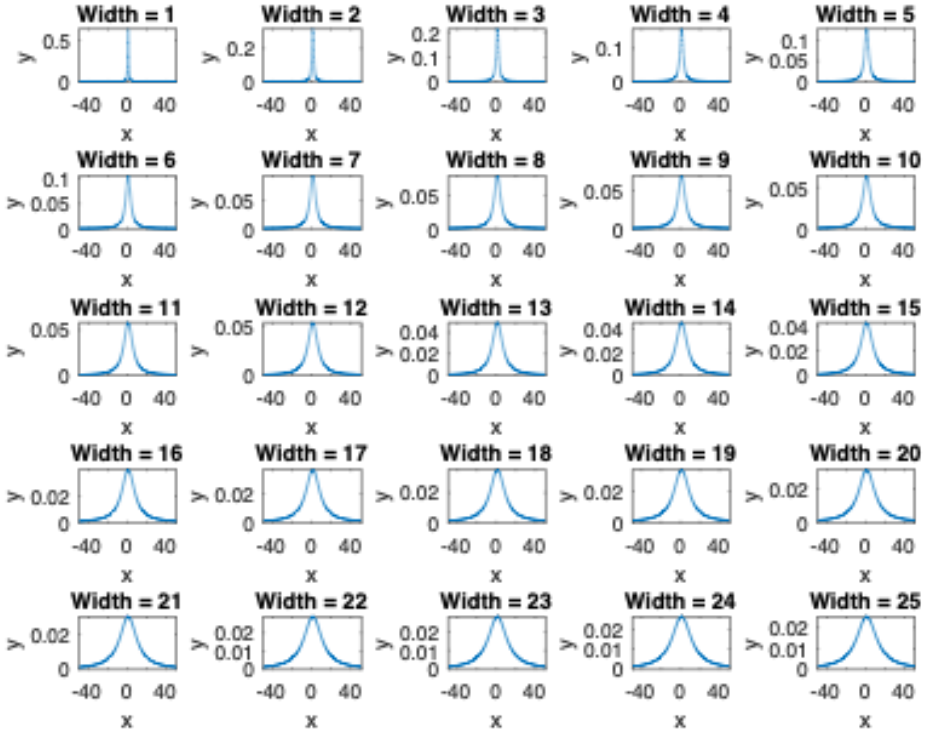

Figure B.1: A representation of disk modulator spectra with varying width, and subsequently, varying Q factors.

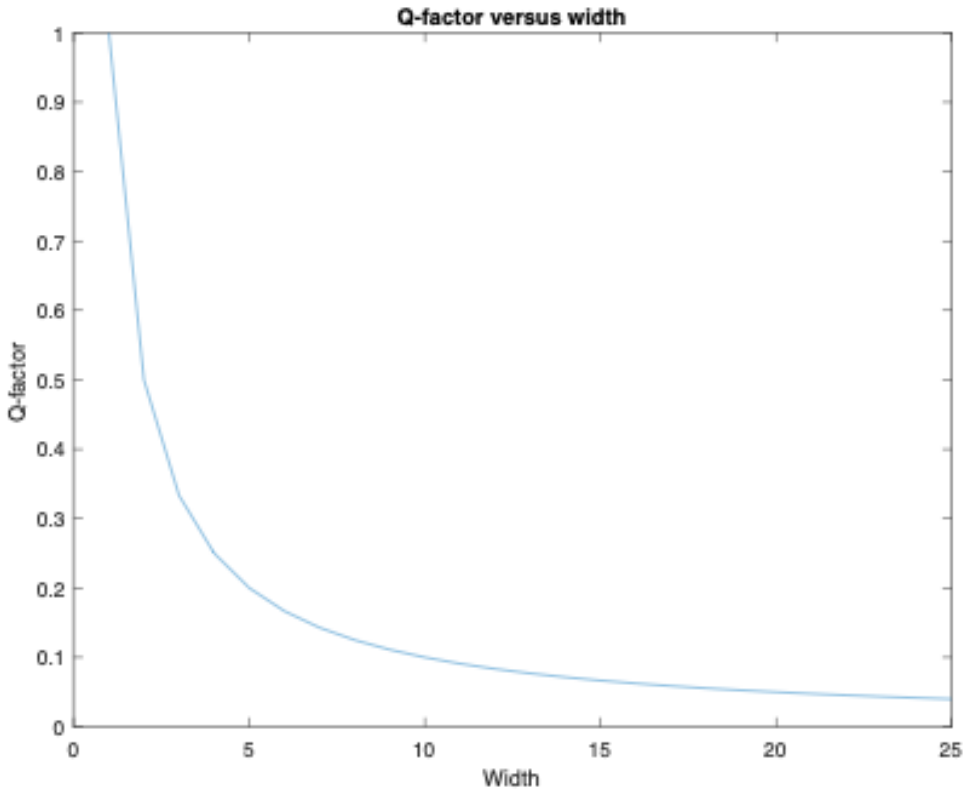

Figure B.2: The relationship between the Q factor of the resonator and the width of the spectrum Lorentzian.

The next course of action was to characterize the initial loss of our system. To do this, we assumed that the coupling constant of our resonator was proportional to the overall loss in our system. Using the equation

$$Q = \frac{2\pi R n_e}{\lambda_0 \kappa^2}, \tag{B.3}$$

where Q is the Q factor, R is the radius of the disk resonator, λ_0 is the resonant wavelength, n_e is the effective index, and κ is the coupling constant, we simply solved for κ to determine the initial system loss as a function of the Q factor. With this initial values of $n_e = 2.9250$,$\lambda_0 = 1550nm$, $R = 10\mu m$, and Q ranging from .04 to 1 we obtained the relationship depicted below in Figure B.3. We understand

that these values are incredibly low compared to a chip that would be used in a functional device, but again these are just initial parameters used to demonstrate the relationships.

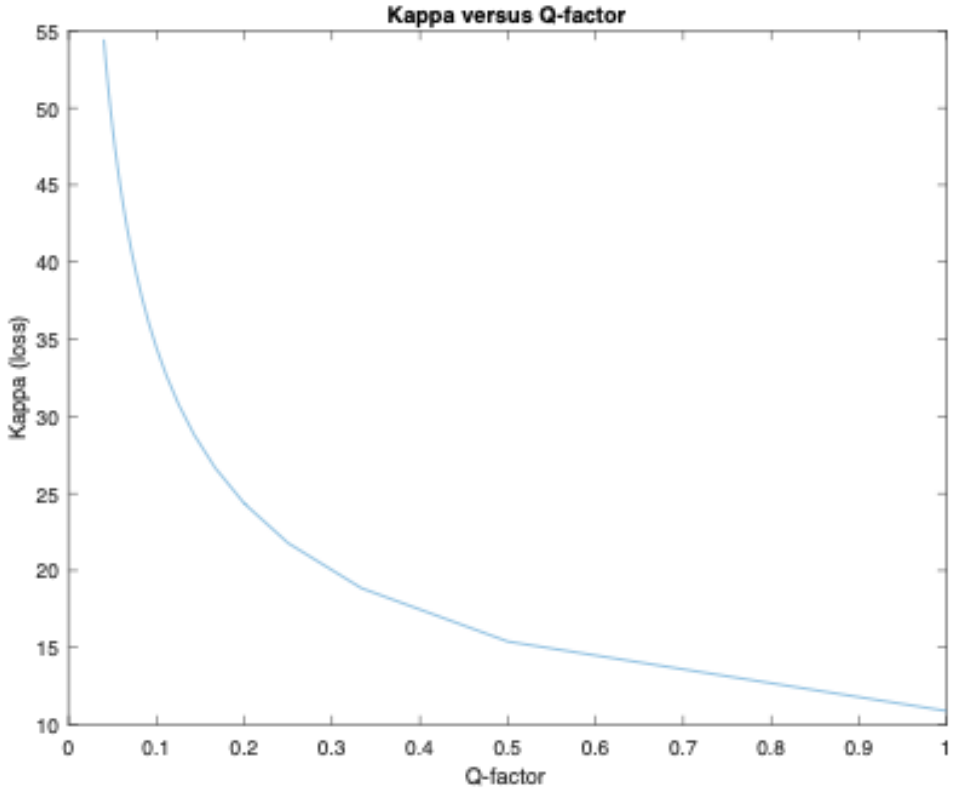

Figure B.3: The relationship between Q factor and the initial system loss.

The next step in our concept design, was to show how a change in the Q factor of the resonator would change the intensity output of our system. As the Q factor decreased, it was reasonable to assume that the transmission at a resonance wavelength would decrease. To show this, we noted the wavelength and intensity of the rightmost point of the FWHM on the highest Q factor Lorentzian. We then calculated the intensity value at that same wavelength for the next width-size Lorentzian, and so on. This concept is illustrated below in Figure B.4, and the ratio of the reduced and initial intensity as a function of subsequent Lorentzian width size is shown in

Figure B.5. We can see that there is an optimum relationship between the change in Q factor needed to see a reasonable change in the output intensity of the resonator for a given wavelength.

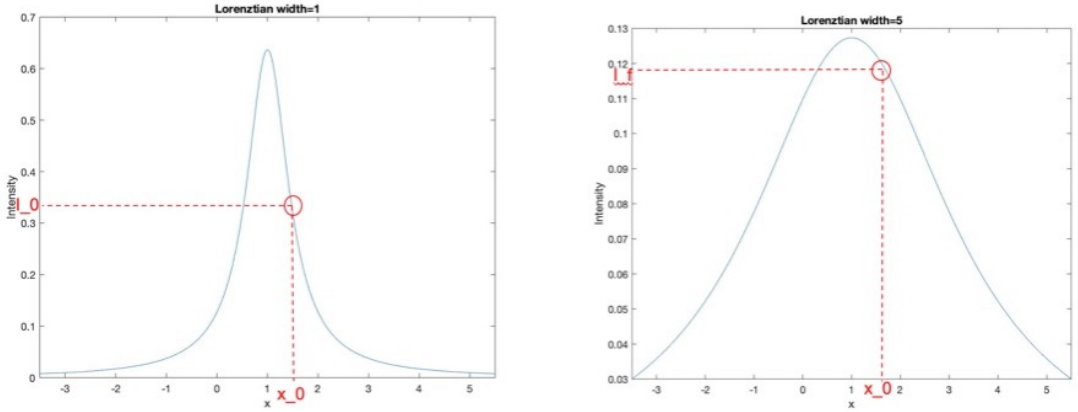

Figure B.4: The Process of determining the ratio of the final intensity and the initial intensity of a Lorentzian.

Once we understood the relationship between the Q factor and the output intensity, we then continued to determine these values for actual systems that we can measure experimentally and compare.

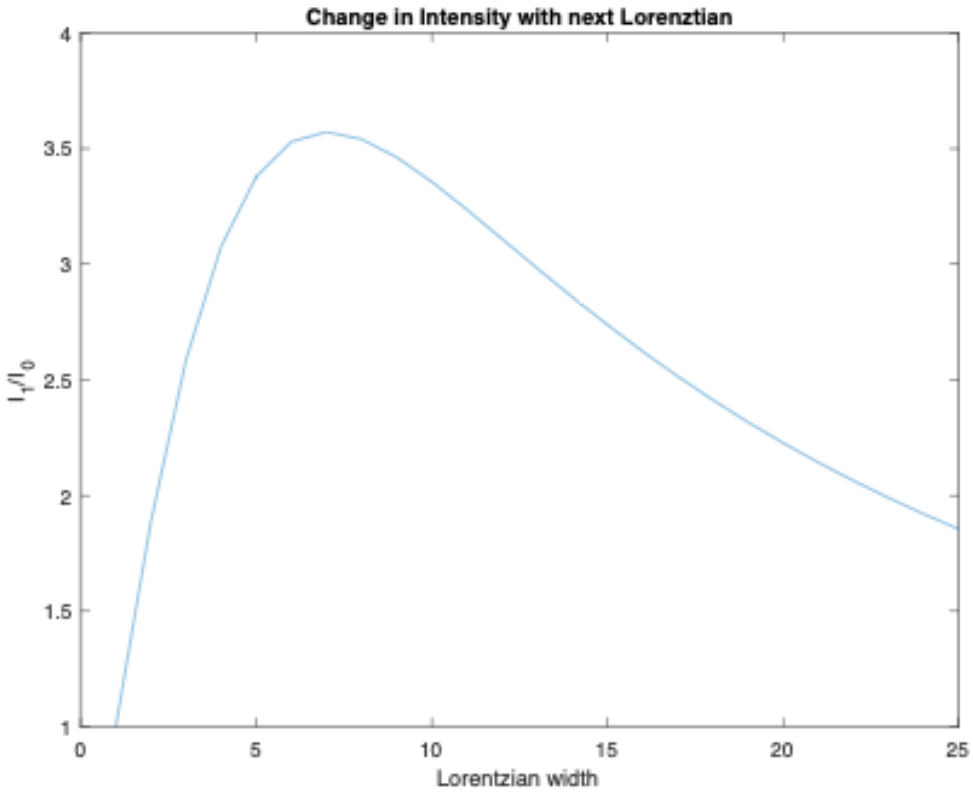

Figure B.5: The ratio of final to initial intensity for each subsequent Lorentzian width.

By using the same equation as we used in Figure B.3, we solved for κ, assuming real values of a typical silicon resonator. of $n_e = 2.9250$, λ_0=1550 nm, R=10 μm, and Q ranging from $10^4 - 10^7$. We determined that the loss of the system ranged between 0.1089 and 0.0034 for these values of Q. Figure B.6 shows this relationship.

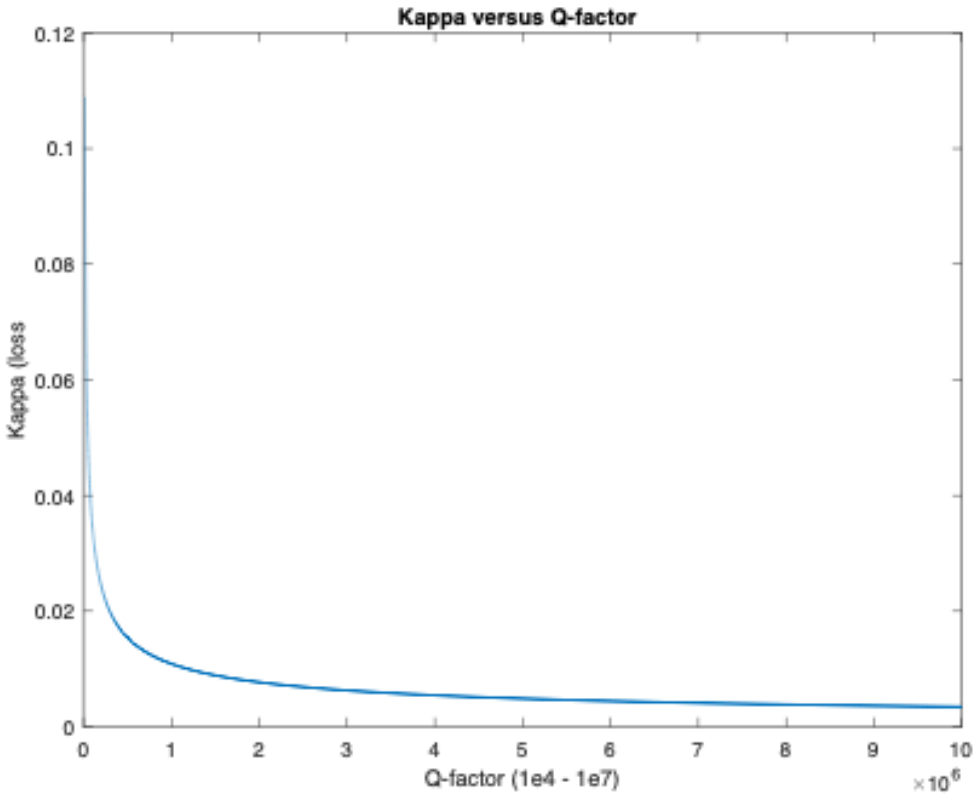

Figure B.6: The "loss" of a real microdisk system versus the Q factor.

Finally, once we understood the relationship between the Q factor and the initial system loss, we needed to determine how the magnetic field changed affected the loss, and subsequently the Q factor of a resonator.

B.2 Magnetic field induced loss on magneto-optic resonators

The next step was to define the relationship between the magnetic field and the polarization rotation of the mode propagating in the resonator. For this we assumed

the setup seen in Figure B.7 where the magnetic field was directed across the disk resonator in a single orientation. The Faraday effect stated that the relationship between the magnetic field and angle of polarization rotation is $\theta = vBd$, where v is the Verdet constant of the MO material, d is the interaction length, and B is the magnetic field.[61] For our discussion, we assume that the interaction length is proportional to the Q factor by the equation $d = Q(2R)\pi$. Thus the rotation of the light polarization can be written as $\theta = vBQ(2R)\pi$. We assumed a radius, R, equal to $10\mu m$, a Verdet constant of 8726 rad/Tm, and an initial Q factor of 10^5. The angle as a function of B within the range of 0 to .1 mT is depicted in Figure B.8.

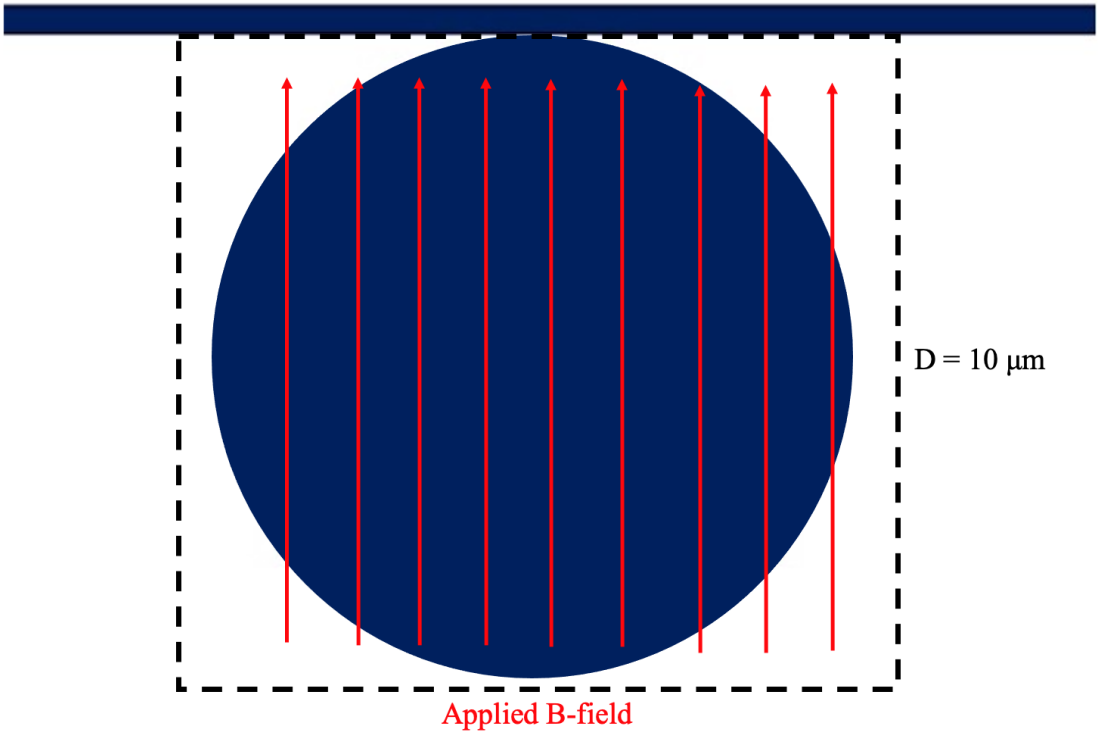

Figure B.7: Schematic of the magnetic field interaction with the disk resonator.

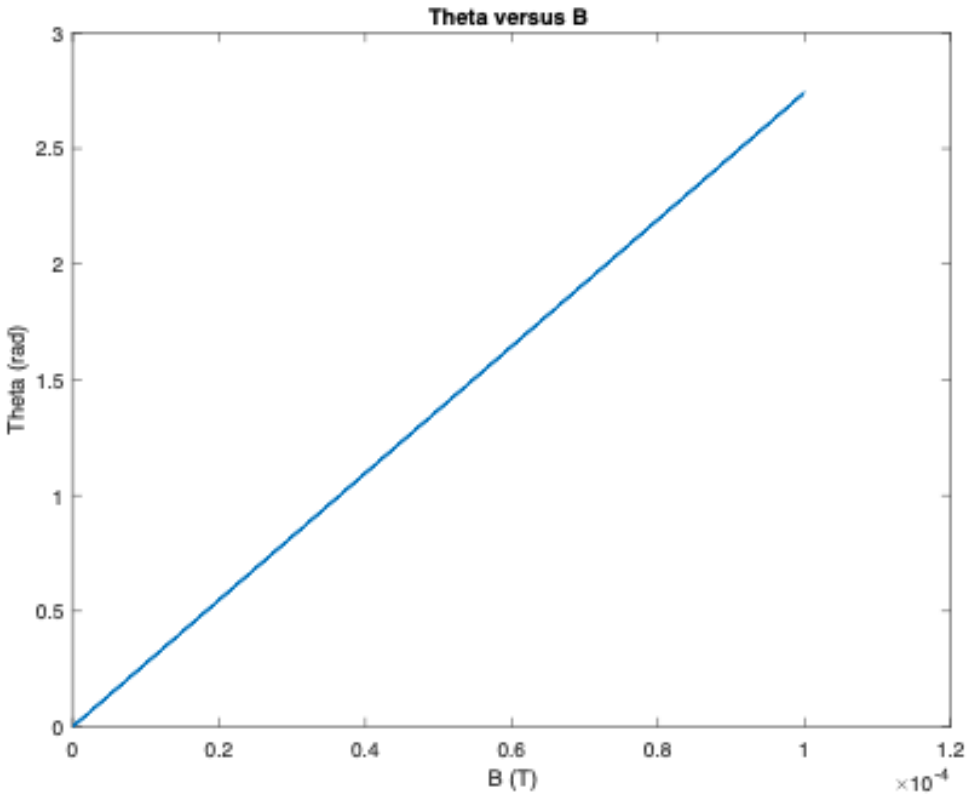

Figure B.8: The rotation of polarization as a function of magnetic field.

We also used these values, along with a variant of our previous equation, namely $Q_0 = \frac{2\pi R n_e}{\lambda_0 \kappa_0^2}$, to determine κ_0^2, or the initial loss of the system. This value was calculated to be 0.0019.

To define a relationship between the magnetic field-induced loss, κ_m^2, and the magnetic field, we used Malus's Law of polarization. We assumed that the loss was proportional to $sin^2\theta$.[94] We can see from Figure B.8, that when we are operating within the regime of microteslas, as we would be ideal, we can assume a small angle and further approximate $\kappa_m^2 = \theta^2$. Using the Faraday effect relationship describing the angle of rotation, we can write the loss as $\kappa_m^2 = (vBQ_0(2R)\pi)^2$. This relationship is shown below in Figure B.9.

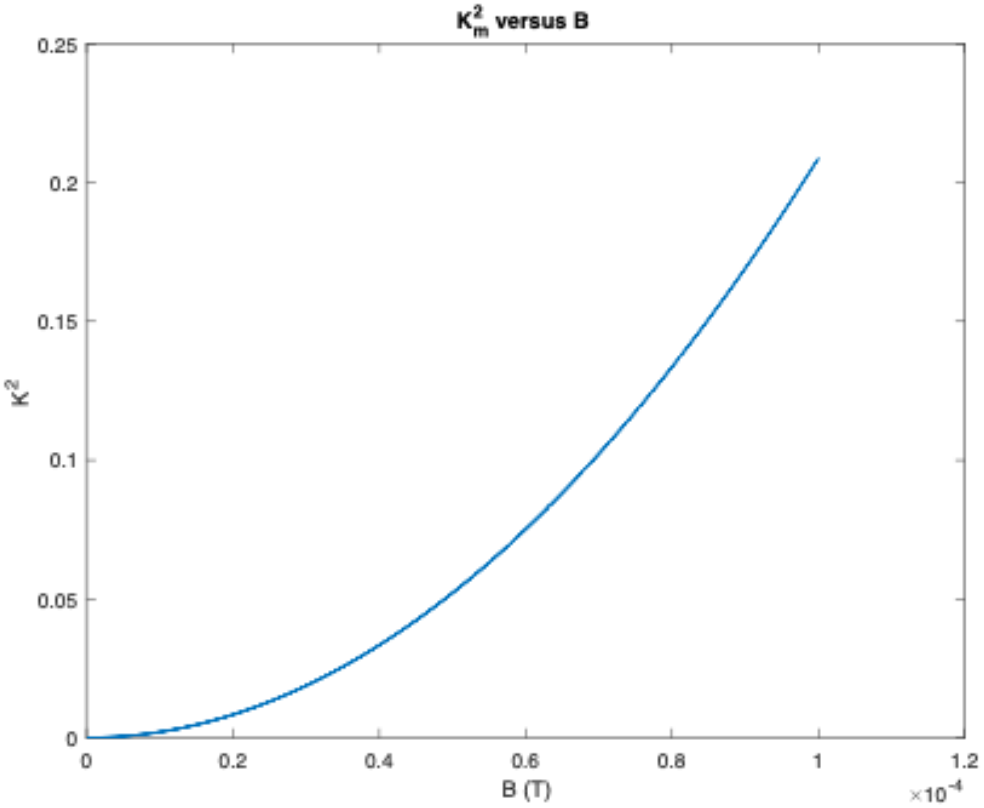

Figure B.9: The loss of the system as a function of the magnetic field.

Our final step is to further relate the Q factor of the system to the applied magnetic field. We begin with our initial equation relating Q factor and loss: $Q = \frac{2\pi R n_e}{\lambda_0 \kappa^2}$. However, we must account for both the initial loss of the system as well the magnetic field induced loss. Thus we can write the total system loss as $\kappa^2 = \kappa_0^2 + \kappa_m^2$. Thus our equation for Q becomes: $Q = \frac{2\pi R n_e}{\lambda_0(\kappa_0^2+\kappa_m^2)}$, where $\kappa_m^2 = (vBQ_0(2R)\pi)^2$. This relationship is depicted below in Figure B.10.

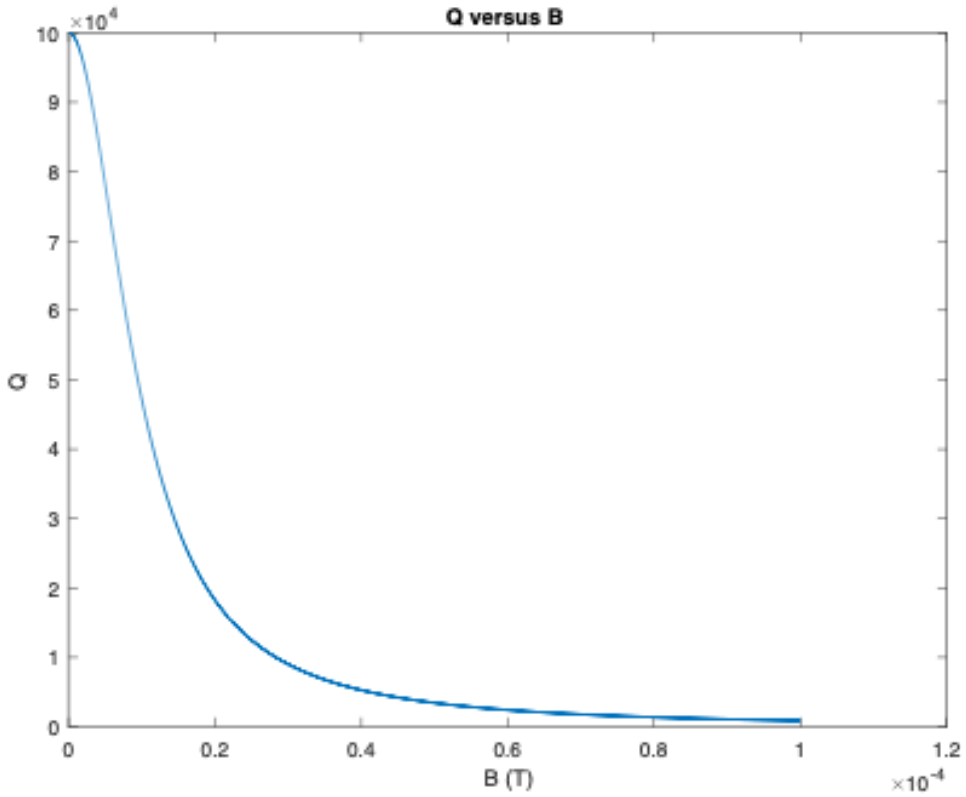

Figure B.10: Q factor of the system as a function of the magnetic field, B.

This magnetic field range offers a rotation exceeding 2.5 radians, which is well out of the limit for a small angle approximation. In order to keep our rotation at or below 0.5 radians, we will set an upper limit on the magnetic field to be about 20 μT. The rotation for this field range is found below in Figure B.11:

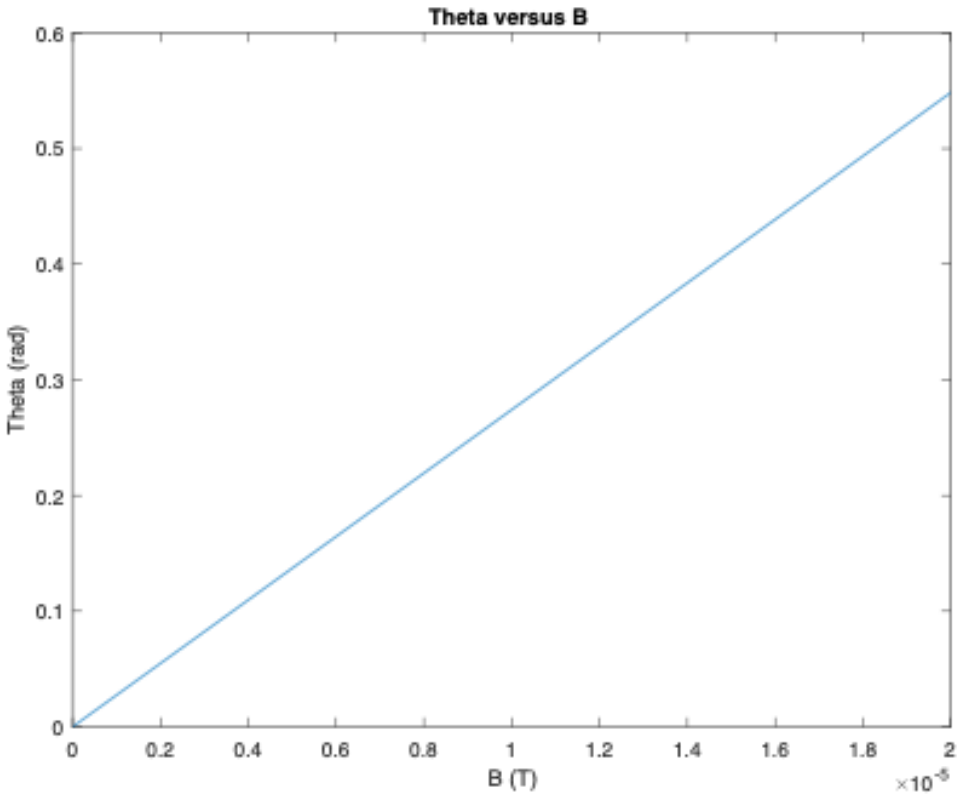

Figure B.11: Theta versus B for a field up to 20 μT.

From this range we can follow through with the previous analysis and determine our κ_m^2 and the change in Q factor for this field range. This data is presented in Figure B.12 and Figure B.13.

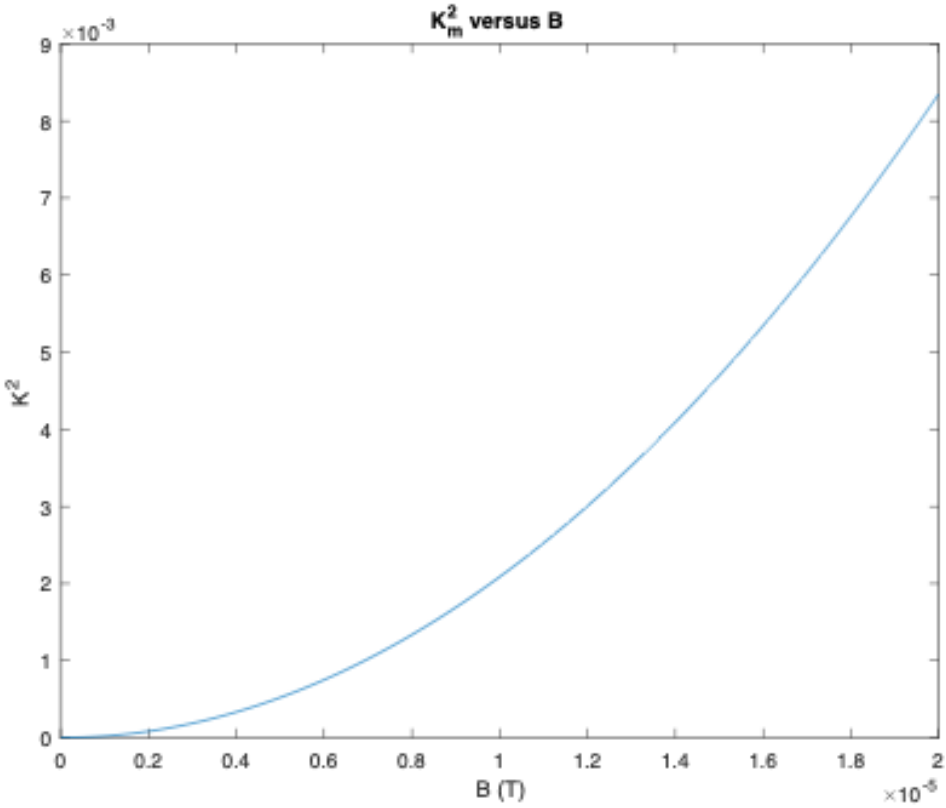

Figure B.12: κ_m^2 versus the magnetic field limited to 20 μT.

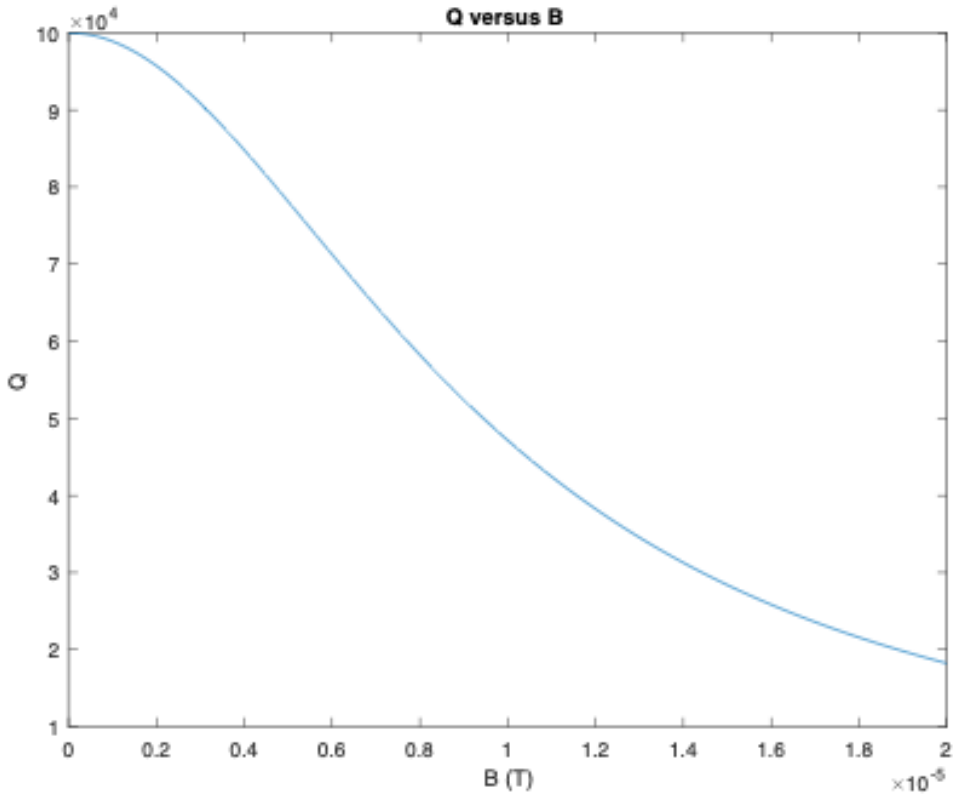

Figure B.13: The Change in Q factor with respect to a magnetic field up to 20 μT.

With use of Figures B.3 and B.5, we can see that the optimum output intensity ratio comes from a change in Q factor of about 1 order of magnitude. We can see that we have nearly achieved this result in Figure B.13 by applying a very small field. These results are promising.

The next step was to see how an increase in the initial Q factor affects the change in Q with magnetic field. We assumed that the initial Q factor was 1 million. The angle rotation for this Q is seen in Figure B.14. The value we get for κ_0^2 with these parameters is 0.000186, which is much lower than our previous value. Previously, within our chosen magnetic field range our two loss values were comparable, but in the scenario κ_0^2 is an order of magnitude higher than κ_m^2.

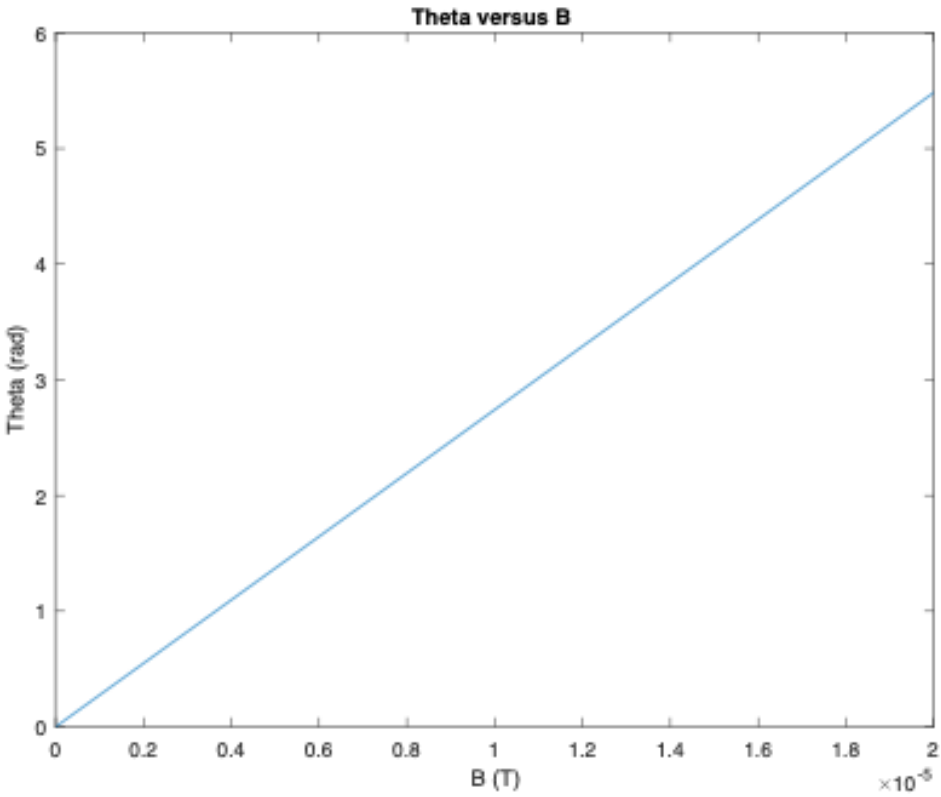

Figure B.14: The angle of rotation with B with an initial Q of 1 million.

Notice that as the initial Q factor is increased, the angle of rotation is also increased. To keep our analysis within the small angle approximation limit we need to further reduce our magnetic field to $2\mu T$. With this new field range, the relationships for κ_m^2 and resulting Q factor are shown in Figures B.15 and B.16, respectively.

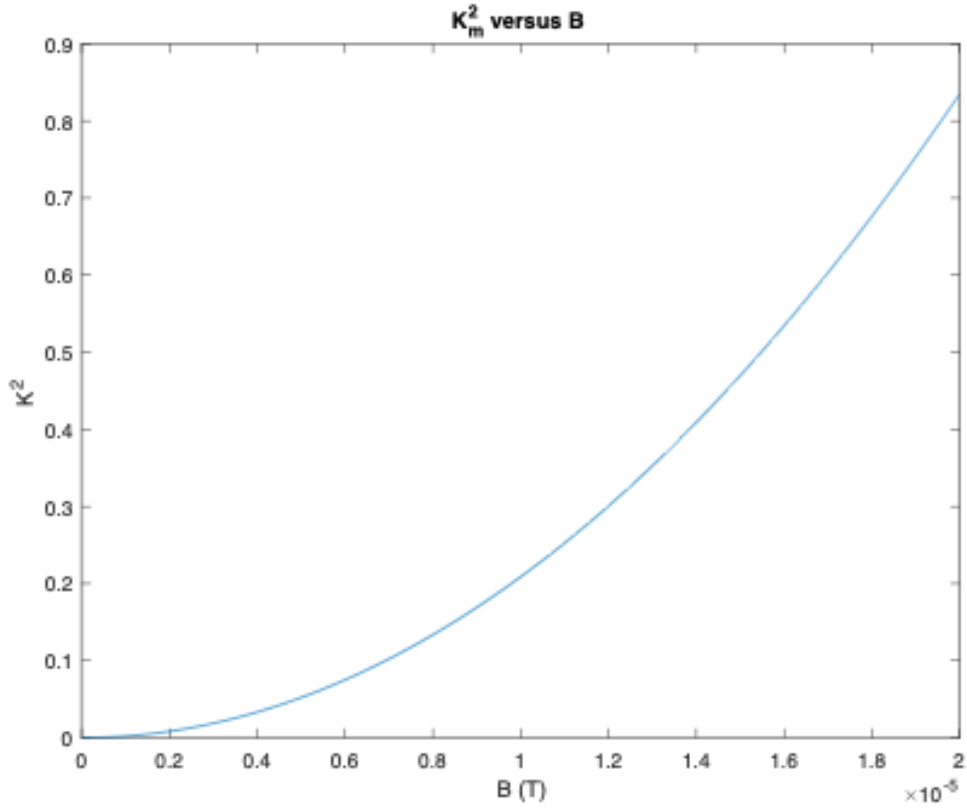

Figure B.15: κ_m^2 versus B for an initial Q of 1 million and fields up to $2\mu T$.

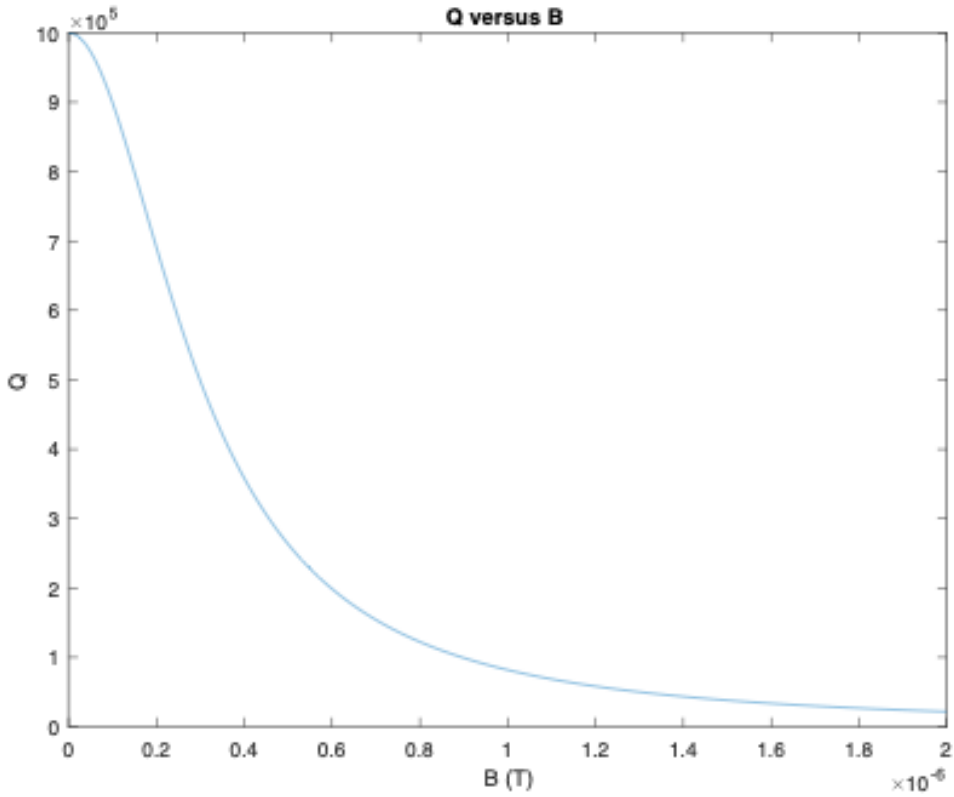

Figure B.16: Final Q factor with respect to B fields up to $2\mu T$ and an initial Q of 1 million.

We can see from this data that increasing the Q allows us to achieve higher contrast in Q factor for smaller magnetic fields.

B.3 Magnetic field simulations

Now that we have determined the theoretical functionality of our devices for certain initial parameters at a given magnetic field range, we continued on to on to simulate the practicality of achieving these magnetic fields with conventionally fabricated electrodes and how fast we could modulate our optical signals. The following

simulations were completed using COMSOL multiphysics.

For these simulations we proposed a $6\mu m$ x $12\mu m$ gold electrode would be used to generate the magnetic field. This design was suggested because these electrodes can be easily fabricated in-house at the University of Arizona, and it is a simple procedure to flip-chip bond the electrode on top of the resonator.

We began in COMSOL by depicting the strength of the static magnetic field produced by this electrode with a current of 10mA. The static magnetic fields are show below in Figures B.17 and B.18. From these images we can determine that the static field is strong enough to induce the changes in Q factor needed to sufficiently modulate the optical signal. Recall that our target magnetic field is $2\mu T$.

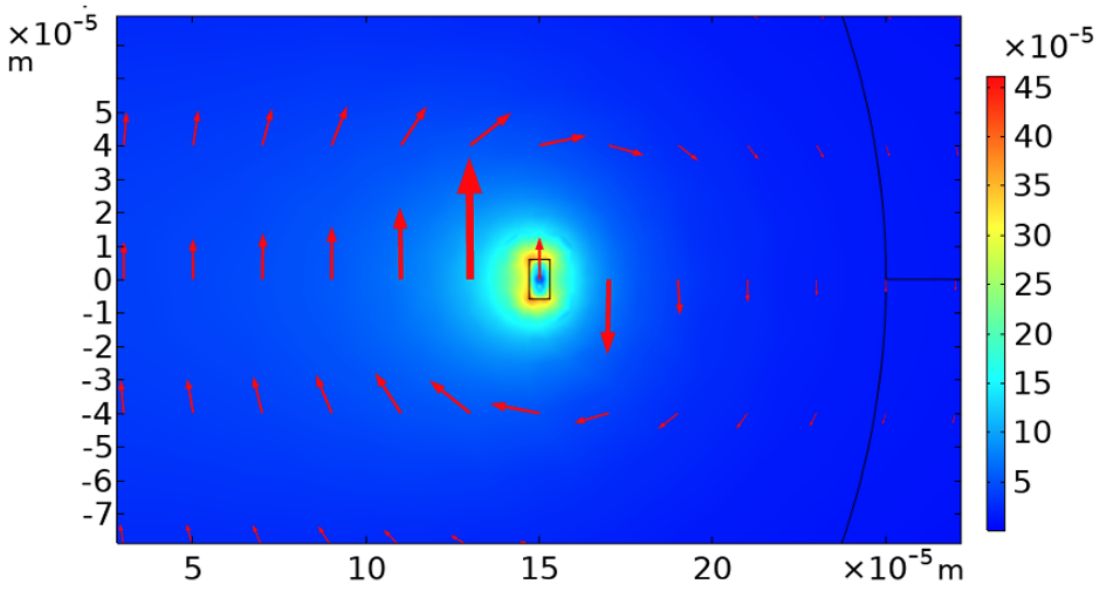

Figure B.17: Static magnetic field behavior of a $6\mu m$ x $12\mu m$ gold electrode.

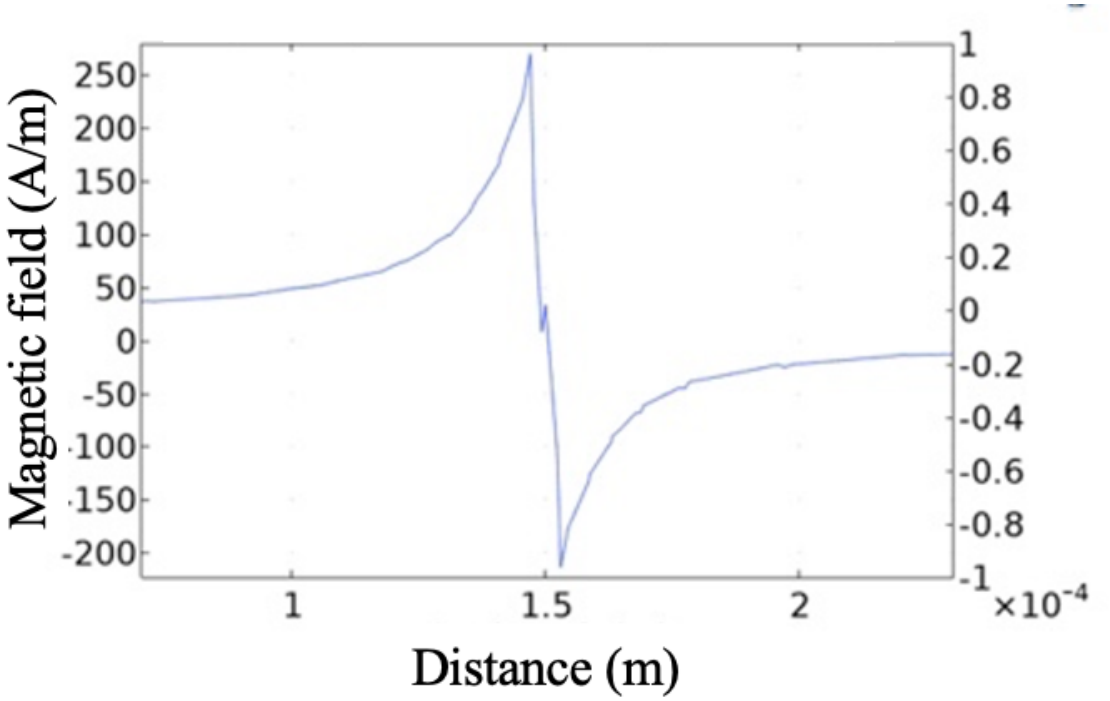

Figure B.18: Measured magnetic field of a $6\mu m$ x $12\mu m$ gold electrode operating at 10mA as a function of distance.

After determining the static field strength, we conducted further calculations to determine the validity of using these electrodes for high-speed modulation. For this we ran a frequency study of the inductance and the reactance at speeds up to 5 GHz, and the voltage necessary to reach 10mA up to 5 GHz. These values are depicted in Figures B.19.

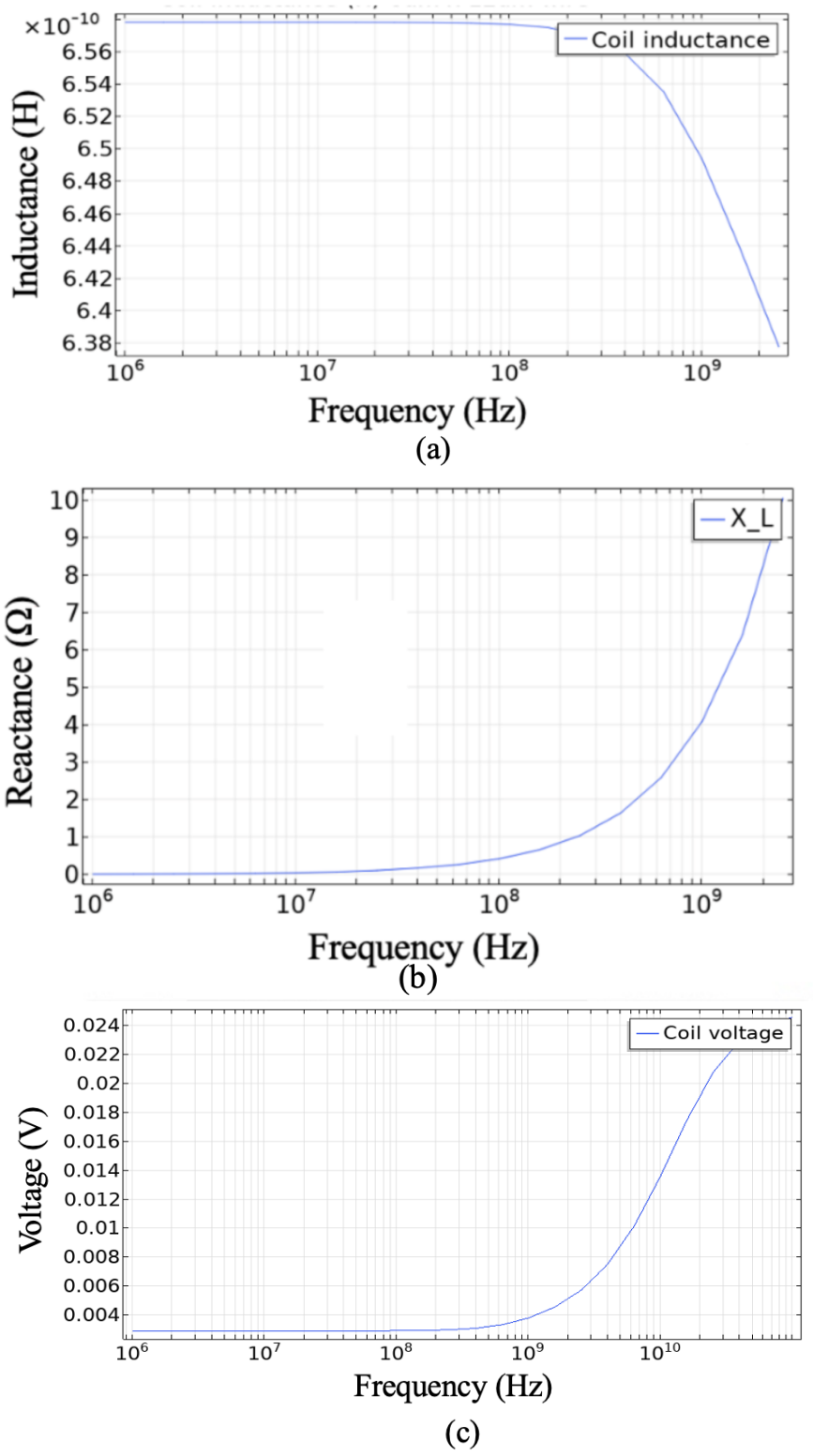

Figure B.19: Inductance (a), reactance (b) and voltage (c) for a $6\mu m$ x $12\mu m$ gold electrode up to 5 GHz.

With these values for the increasing operating frequency, we can calculate the current and the magnetic field that can actually be achieved with this electrode design.

The peak current of the wire operating at high frequencies is determined by the equation

$$I_0 = -\frac{V_0}{\sqrt{R^2 + (X_L^2 - X_C^2)^2}}, \tag{B.4}$$

where V_0 is the voltage, R is the resistance and X_L and X_C are the reactacnce of the inductance and the capacitance, respectively.[95] Since we were simulating a wire, we assumed that X_C was zero. Each of the remaining values was calculated in COMSOL for 100KHz, 1 MHz, 10 MHz, 100 MHz and 1 GHz. A baseline current value was used as a comparison and held at a constant values of 10mA.

The oscillating current as a function of time is determined by the equation

$$I(t) = I_0 sin(\omega t - \phi), \tag{B.5}$$

where ω is the frequency, and ϕ is a phase shift that we assumed to be zero.[95] These current values for the different frequencies are shown in Figure B.20

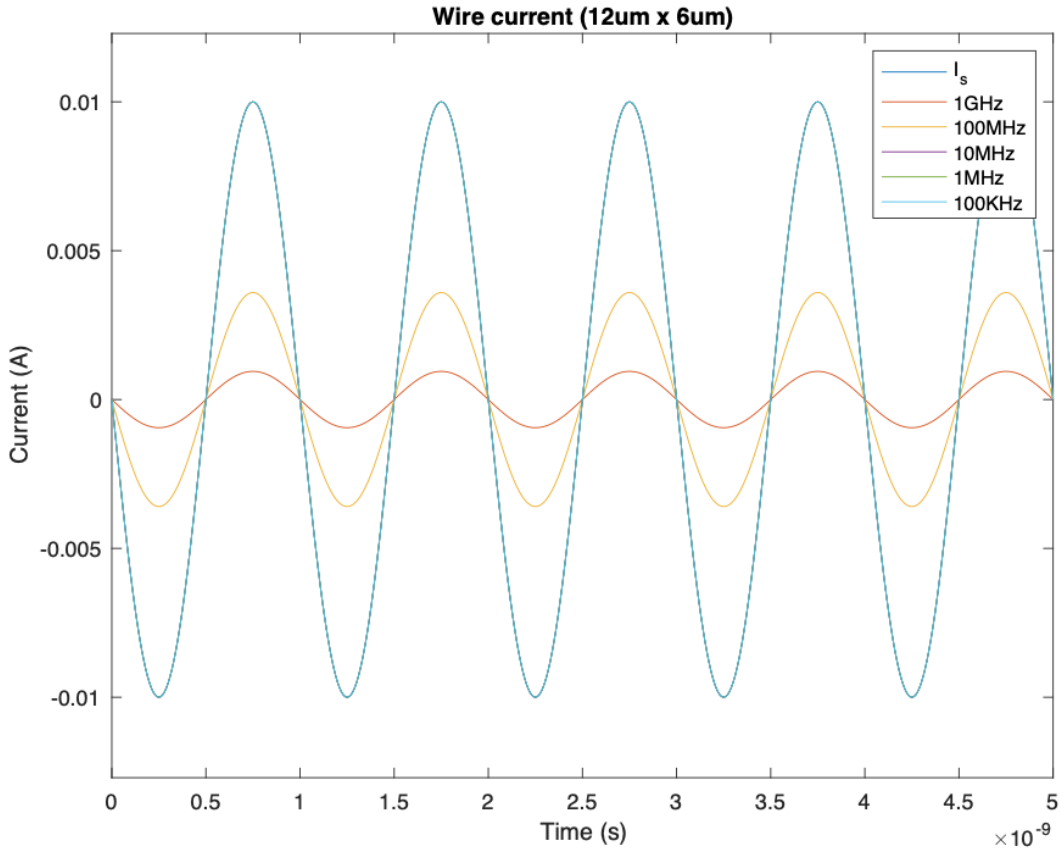

Figure B.20: The modulated current amplitude possible from our electrode at varying frequencies.

With a better understanding of how the current in our wire will behave, we can use that information to show the magnetic fields we can use to modulate our signal up to 1 GHz. For this we used the relationship

$$B = \frac{\mu_0 I(t)}{2\pi r}, \tag{B.6}$$

where μ_0 is the permeability constant r is the radial distance from the center of the wire.[62] Since we are assuming we can flip-chip bond these electrodes, we assumed that the separation between the disk resonator and the electrode would only be

about $3\mu m$, since that is roughly the thickness of our MO film. The total value of r for the magnetic field calculation was taken to be $6\mu m$ to account for the thickness of the wire. The resulting magnetic field derived from our current values from (B.5) are shown in Figure B.21.

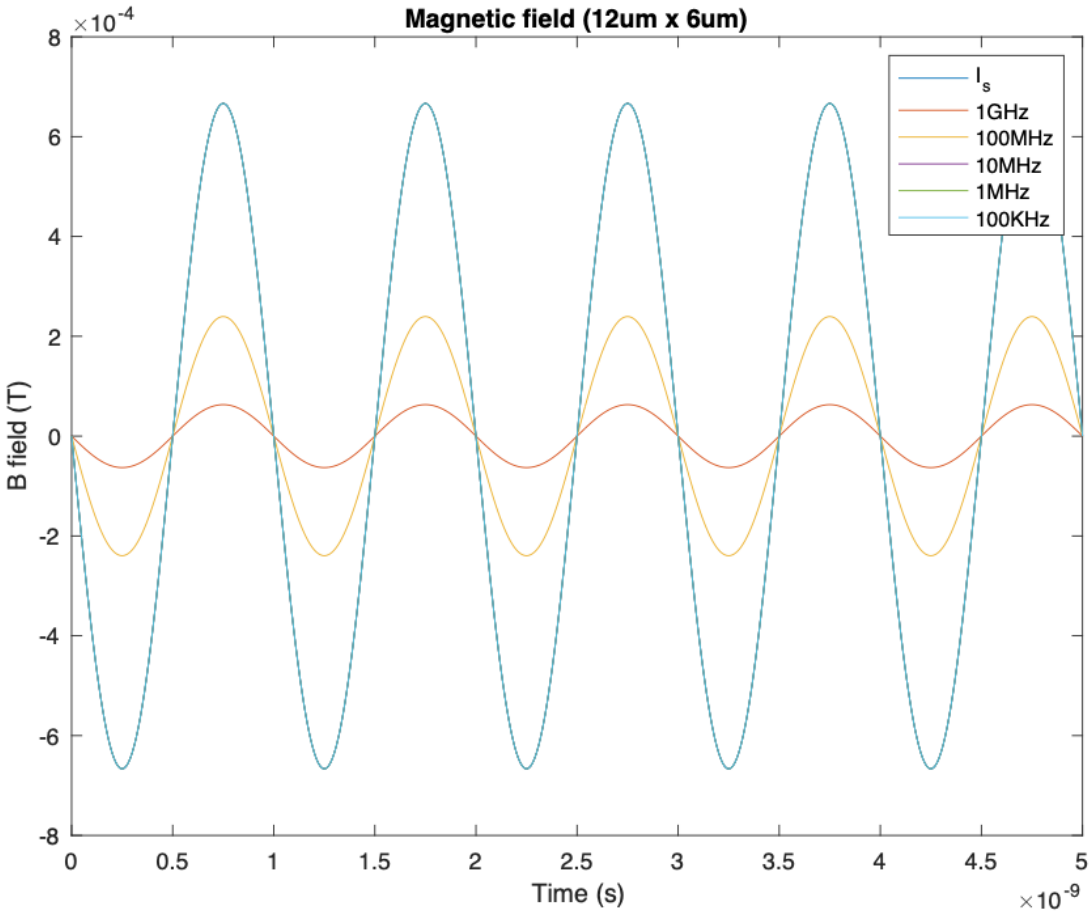

Figure B.21: The modulated magnetic field amplitude possible from our electrode at varying frequencies.

From these results we have confirmed that with ideal conditions we are able to achieve the desired magnetic field range of $2\mu T$ in order to provide sufficient signal modulation using this magneto-optic modulator design.

B.4 Considerations

Although these results are promising, there are a few assumptions that were made and should be considered in future analysis. These assumptions are as follows:

1. In our initial considerations, we did not take into account any potential wavelength shift with a change in Q factor. However, when working with real system it is likely that with a change in Q factor comes a change in the resonant wavelength. These changes would likely occur from potential shifts in absolute index changes, thought the exact relationship defining this resonance shift is currently unknown since this type of design has not been thoroughly studied. Although this was simple enough to ignore for these calculations, it should be accounted for when modeling real systems as best as possible.

2. In these calculations, we assumed that the full strength of the magnetic field produced from the wire would contribute to the Faraday rotation in the resonator, in reality this is not the case for two reasons: the first being the shape of the field strength from the wire, and the second being the shape of the resonator interacting with the magnetic field.

   The field produced from a current wire takes the form of a circle rotating around the wire as given by Ampere's Law:

$$\Delta \times \mathbf{H} = \frac{\partial \mathbf{D}}{\partial t} + \mathbf{J}, \tag{B.7}$$

   where $\frac{\partial \mathbf{D}}{\partial t}$ is zero for this scenario, $\mathbf{H}$ is the magnetic field and $\mathbf{J}$ is the current density of the wire.[62] There is symmetry of the field such that the field strength is constant for a given radial distance from the wire. This is demonstrated visually in Figure B.22. If the wire is centered in the middle of the resonator, then the field strength at the edges will be lower due to the larger radial distance from the current wire.

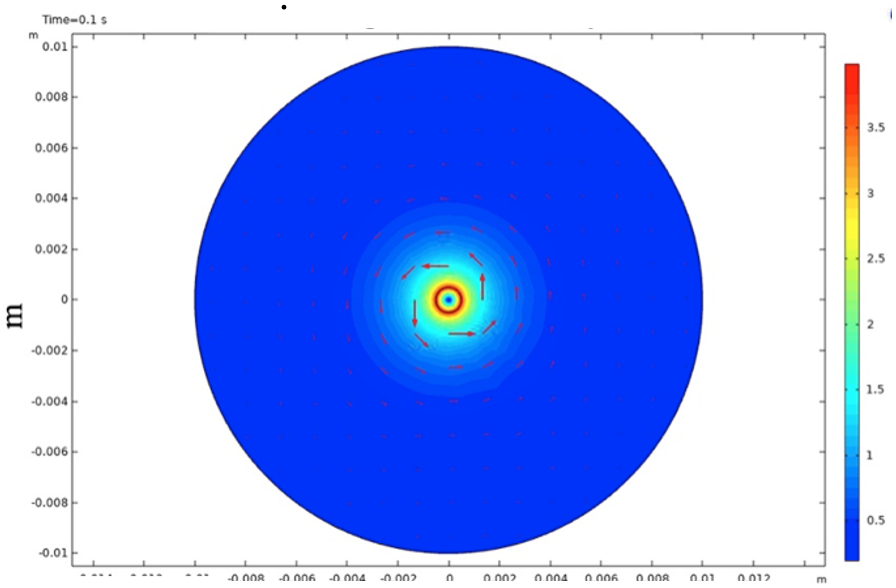

Figure B.22: Static magnetic field of a standard 25 μm wire.

Additionally, as stated previously, Faraday rotation is only induced by light that is propagating parallel or anti-parallel to a magnetic field. This means that as the light propagates along the ring, only at the section of the resonator where the light is propagating tangential to the magnetic field will it interact with the full strength of the field. When the light is 90^o from this point, it is not interacting with any of the magnetic field.

These two considerations can be accounted for on our calculations by integrating the contributing field along a circular path both in the path along the light propagation, and along the magnetic field strength. Since we did not do this in these initial calculations, our required magnetic field will be larger than what we have predicted here.

3. In our initial considerations, we assumed that the interaction length was proportional to the Q factor of the system. Although this is true, we are not aware of what the proportionality constant is. We assumed a 1:1 relationship – that a Q factor of 1 million means it travels the length of the circumference

1 million times. In reality it may be more or less than that. This relationship could be measured directly by measuring the time the light spends in the resonator, and working backwards from the speed of light to determine the length traveled in the resonator. We do not have means to measure this directly, but for future work this would be a meaningful contribution to the accuracy of these simulations.

4. We assumed that the loss in the system would vary as described by Malus's law, and that we could consider the loss to be proportional to $sin^2(\theta)$, but in reality this is not something that is known. To achieve more accurate estimates for how the loss of our system respond to an increase in the Faraday rotation, we would need to model that directly instead of using this loose estimate. Further simulations would need to be conducted to model the polarization of the light in the disk resonator in order to determine how the polarization affects the loss of the system. It is likely that even 45 degrees of rotation would not result in the total loss of light through the resonator, unless it was designed such that only one polarization state was supported in the device. Since most waveguides and resonators can support TE and TM polarization to some extent, it is unlikely we could create this condition in a real device.

5. This model assumes that whatever light is in the resonator is interacting with the MO material. In reality, the MO material will only be the cladding of the system, and therefore the interaction will be limited by the confinement factor of the resonator. We can simulate this system and determine the confinement factor and scale this calculation accordingly, but as it stands, we are overestimating the rotation we will achieve from this interaction.

6. We did not account for the self-consistency of the change in Q factor when applying a magnetic field. Out initial calculations gave us a value for the interaction length based on the initial Q factor of the system, which gave us a value for the loss, and subsequently the change in overall Q factor. Thus, as a magnetic field is applied and the Faraday effect causes a change in the Q

factor, that same change in Q reduces the effectiveness of the Faraday effect – and the cycle repeats. For now we can assume that this loop is negligible beyond a first order approximation, but it should be explored more directly when considering further investigations.

7. Although some of the current shortcomings of the calculations appear to show that we require much stronger fields that initially predicted, the voltage that we have currently simulated is incredibly low (on the order of 10^{-3} V). Operating the system on the order of 1V is not unreasonable for a respectable system and allows us to reach the fields strengths necessary to overcome these current oversights in our initial concept simulations.

REFERENCES

[1] Cisco. Cisco predicts more ip traffic in the next five years than in the history of the internet. `https://newsroom.cisco.com/press-release-content?articleId=1955935`, November 2018.

[2] Daryl Inniss and Roy Rubenstein. *Silicon Photonics: Fueling the Next Information Revolution*. Morgan Kaufmann, December 2016. Google-Books-ID: MxYoCgAAQBAJ.

[3] Sean Koehl, Ansheng Liu, and Mario Paniccia. Integrated Silicon Photonics:. pages 25–29.

[4] K. Hasharoni K. Hassan Y. Thonnart P. Tissier S. Desieres S. Olivier T. Tekin B. Szelag S.Bernabe, Q. Wilmart. Silicon photonics for terabit/s communication in data centers and exascale computers. 179:107928, May 2021.

[5] Leonid Tsybeskov, David J. Lockwood, and Masakazu Ichikawa. Silicon Photonics: CMOS Going Optical. *Proceedings of the IEEE*, 97(7):1161–1165, July 2009. Conference Name: Proceedings of the IEEE.

[6] Sasan Fathpour and Bahram Jalali. *Silicon Photonics for Telecommunications and Biomedicine*. CRC Press, December 2011. Google-Books-ID: kDsB_3L1C_0C.

[7] J. K. Doylend and S. Gupta. An overview of silicon photonics for LIDAR. In *Silicon Photonics XV*, volume 11285, page 112850J. International Society for Optics and Photonics, February 2020.

[8] Daniel J. Blumenthal, René Heideman, Douwe Geuzebroek, Arne Leinse, and Chris Roeloffzen. Silicon Nitride in Silicon Photonics. *Proceedings of the IEEE*, 106(12):2209–2231, December 2018. Conference Name: Proceedings of the IEEE.

[9] Jacob S Levy, Mark A Foster, Alexander L Gaeta, and Michal Lipson. Harmonic generation in silicon nitride ring resonators. *Optics Express*, 19:7, 2011.

[10] N. Park, C. Choi, T. Seong, and S. Park. Quantum confinement in amorphous silicon quantum dots embedded in silicon nitride. *Physical review letters*, 87, 2001.

[11] Goran Z. Mashanovich, Milan M. Milosevic, Milos Nedeljkovic, David Cox, Vittorio M.N. Passaro, Harold M.H. Chong, and Richard Soref. Mid-infrared silicon photonics for sensing applications. *MRS Online Proceedings Library*, 1437(1):7–16, December 2012.

[12] Spectral Library | USGS.gov, spectroscopy lab. `https://www.usgs.gov/labs/spec-lab/capabilities/spectral-library`.

[13] Miguel Levy, Olga V. Borovkova, Colin Sheidler, Brandon Blasiola, Dolendra Karki, François Jomard, Mikhail A. Kozhaev, Elena Popova, Niels Keller, and Vladimir I. Belotelov. Faraday rotation in iron garnet films beyond elemental substitutions. *Optica*, 6(5):642–646, May 2019. Publisher: Optical Society of America.

[14] Jia Ouyang, Ying Zhang, and Huahui He. Measurement of the Faraday effect of garnet film in alternating magnetic fields. *Journal of Applied Physics*, 75(10):6795–6797, May 1994. Publisher: American Institute of Physics.

[15] Juejun Hu, Lan Li, Hongtao Lin, Ping Zhang, Weidong Zhou, and Zhenqiang Ma. Flexible integrated photonics: where materials, mechanics and optics meet. *Optics Materials Express*, 3:19, 2013.

[16] Aleksandrs Marinins. *Polymer Components for Photonic Integrated Circuits*. PhD thesis, KTH School of Engineering Sciences, Stockholm sweeden, November 2017.

[17] Shao-Yun Fu. Cryogenic Properties of Polymer Materials. In Susheel Kalia and Shao-Yun Fu, editors, *Polymers at Cryogenic Temperatures*, pages 9–39. Springer, Berlin, Heidelberg, 2013.

[18] Chin-Lin Chen. *Foundations for guided-wave optics*. Wiley-Interscience, 2007.

[19] M. Jamal and Deen. *Silicon photonics fundamental and devices*. John Wiley and sons, 2012.

[20] B.A.E Saleh and M.C. Teich. *Fundamentals of photonics 2nd edition*. John Wiley and sons, 2007.

[21] Saman Jahani, Sangsik Kim, Jonathan Atkinson, Justin C. Wirth, Farid Kalhor, Abdullah Al Noman, Ward D. Newman, Prashant Shekhar, Kyunghun Han, Vien Van, Raymond G. DeCorby, Lukas Chrostowski, Minghao Qi, and Zubin Jacob. Controlling evanescent waves using silicon photonic all-dielectric metamaterials for dense integration. *Nature Communications*, 9(1):1893, May 2018. Number: 1 Publisher: Nature Publishing Group.

[22] B.I. Pantchev. Multimode strip waveguide formed by ion-electro-diffusion from solid state silver: Side diffusion reduction. *Optics Communications*, 60, 1986.

[23] De-Long Zhang. Near-stoichiometric ti : $Linbo_3$ strip waveguides fabricated by standard ti diffusion and post-vte. *IEEE Photonics Technology Letters*, 2009.

[24] P.K. Tien. Ilight waves in thin films and integrated optics. *Applied Optics*, 10, 1971.

[25] B. E. Little, S. T. Chu, H. A. Haus, J. Foresi, and J. Laine. Microring resonator channel dropping filters. *Journal of Lightwave Technology*, 15(6):998–1005, June 1997. Conference Name: Journal of Lightwave Technology.

[26] Dominik G. Rabus. *Integrated ring resonators: a compendium*. Springer, 2020.

[27] Toshiaka Suhara Hiroshi Nishihara, Masamitsu Haruna. *Optical Integrated Circuits 1st Edition*. McGraw Hill Professional, 1989.

[28] Andy Eu-Jin Lim. Review of silicon photonics foundry efforts. *IEEE Journal of Selected Topics in Quantum Electronics*, 20, 2014.

[29] J. T. M. Stevenson. The application of photolithography to the fabrication of microcircuits. *Journal of Physics E: Scientific Instruments*, 19, 1986.

[30] Melissa A. Smith. Design, simulation, and fabrication of three-dimensional microsystem components using grayscale photolithography. *Journal of Micro/-Nanolithography, MEMS, and MOEMS*, 18, 2019.

[31] Stephen J. Pearton. Dry etching of electronic oxides, polymers, and semiconductors. *Plasma Processes and Polymers*, 2, 2005.

[32] Kerry J. Vahala. Optical microcavities. *Nature*, 424, 2003.

[33] Juejun Hu Tomoyuki Izuhara Michel Jurgen Lionel Kimerling 5. Vivek Raghunathan, Winnie N.Ye. Athermal operation of silicon waveguides: spectral, second order and footprint dependencies. *Optics express*, 18, 2010.

[34] Nist - chemistry webbook srd-69. `https://webbook.nist.gov/chemistry/name-ser/`.

[35] Niranjan Sahu. Fundamental understanding and modeling of spin coating process: A review. *Indian Journal of Physics*, 83, 2009.

[36] Graham Fischer. Silicon crystal growth and wafer technologies. *Proceedings of the IEEE*, 100, 2012.

[37] AIM Photonics. AIM photonics foundry PDK, August 2020.

[38] Cen Xia, Neng Bai, Ibrahim Ozdur, Xiang Zhou, and Guifang Li. Supermodes for optical transmission. *Optics Express*, 18:12, 2011.

[39] Hagen Renner. Supermodes of optical fibre couplers. *Optics Communications*, 94(6):574–588, December 1992.

[40] IR Flex. Chalcogenide Glass Fibers | IRFlex Corporation. `https://irflex.com/products/irf-s-series/`.

[41] Aleksandrs Marinins. Coupling Efficiency and Alignment Sensitivity of Single Mode Optical Fibers. Master's thesis, University of central Florida, 1979.

[42] Stewart E. Miller and Ivan P. 1930 Kaminow. *Optical fiber telecommunications II*. Academic Press, Boston, 1988. Section: xx, 995 pages : illustrations ; 24 cm.

[43] Le Verre Fluoré. IFG Single mode. `https://leverrefluore.com/products/passive-fibers/ifg-single-mode/`.

[44] Dongfeng Liu Robert Pafchek David Gardner Paul Foy Mohammed Saad Doug Jenkins Alex Cable Reza Salem, Zack Jiang and Peter Fendel. Mid-infrared supercontinuum generation spanning 1.8 octaves using step-index indium fluoride fiber pumped by a femtosecond fiber laser near 2 μm. *Optics express*, 2015.

[45] Leo Young. *Advances in Microwaves: Volume 1*. Academic Press, January 2016. Google-Books-ID: Qr83BQAAQBAJ.

[46] Yu Li, Yu Zhang, Lei Zhang, and Andrew W. Poon. Silicon and hybrid silicon photonic devices for intra-datacenter applications: state of the art and perspectives [Invited]. *Photonics Research*, 3(5):B10–B27, October 2015. Publisher: Optical Society of America.

[47] K. Padmaraju and K. Bergman. Resolving the thermal challenges for silicon microring resonator devices. *Nanophotonics*, 2014.

[48] Martin A. Green and Mark J. Keevers. Optical properties of intrinsic silicon at 300 K. *Progress in Photovoltaics: Research and Applications*, 3(3):189–192, 1995. _eprint: https://onlinelibrary.wiley.com/doi/pdf/10.1002/pip.4670030303.

[49] Paulina Dobrowolska, Aleksandra Krajewska, Magdalena Gajda-Raczka, Bartosz Bartosewicz, Piotr Nyga, and Bartłomiej J. Jankiewicz. Application of Turkevich Method for Gold Nanoparticles Synthesis to Fabrication of SiO2@Au and TiO2@Au Core-Shell Nanostructures. *Materials*, 8(6):2849–2862, May 2015.

[50] Soha Namnabat, Kyung-Jo Kim, Adam Jones, Roland Himmelhuber, Christopher T. DeRose, Douglas C. Trotter, Andrew L. Starbuck, Andrew Pomerene, Anthony L. Lentine, and Robert A. Norwood. Athermal silicon optical add-drop multiplexers based on thermo-optic coefficient tuning of sol-gel material. *Optics Express*, 25(18):21471–21482, September 2017. Publisher: Optical Society of America.

[51] Amir Arbabi and Lynford L. Goddard. Measurements of the refractive indices and thermo-optic coefficients of Si_3N_4 and SiO_x using microring resonances. *Optics Letters*, 38(19):3878–3881, October 2013. Publisher: Optical Society of America.

[52] Chemical Rubber Company. *CRC Handbook of chemistry and physics*. CRC Press, 1978.

[53] Air (properties of). a-to-z guide to thermodynamics, heat and mass transfer, and fluids engineering. `https://doi.org/10.1615/atoz.a.air_properties_of`.

[54] Hwan Soo Dow, Woo Sik Kim, and Jung Woo Lee. Thermal and electrical properties of silicon nitride substrates. *AIP Advances*, 7(9):095022, September 2017. Publisher: American Institute of Physics.

[55] Robert Hull and INSPEC. *Properties of crystalline silicon*. EMIS datareviews series ; no. 20. INSPEC, the Institution of Electrical Engineers, London, 1999.

[56] Charles Kittel. *Thermal physics*. WHFreeman, San Francisco, 2d ed. edition, 1980.

[57] Ning-Ning Feng, Po Dong, Dazeng Feng, Wei Qian, Hong Liang, Daniel C. Lee, Jonathan B. Luff, Anjali Agarwal, Tom Banwell, Ron Menendez, Paul Toliver, Ted K. Woodward, and Mehdi Asghari. Thermally-efficient reconfigurable narrowband RF-photonic filter. *Optics Express*, 18(24):24648, November 2010.

[58] G. Gilardi, W. Yao, H. Rabbani Haghighi, X. J. M. Leijtens, M. K. Smit, and M. J. Wale. Deep Trenches for Thermal Crosstalk Reduction in InP-Based Photonic Integrated Circuits. *Journal of Lightwave Technology*, 32(24):4864–4870, December 2014. Conference Name: Journal of Lightwave Technology.

[59] Daniel Pérez, Ivana Gasulla, Lee Crudgington, David J. Thomson, Ali Z. Khokhar, Ke Li, Wei Cao, Goran Z. Mashanovich, and José Capmany. Multipurpose silicon photonics signal processor core. *Nature Communications*, 8(1):636, September 2017. Number: 1 Publisher: Nature Publishing Group.

[60] Shelbi L. Jenkins, Sasaan A. Showghi, and Robert A. Norwood. Optical tuning of si_3n_4 ring resonators using an external short visible wavelength laser source. *OSA Continuum*, 4(5), 2020.

[61] P. S. Pershan. Magneto-Optical Effects. *Journal of Applied Physics*, 38:1482–1490, March 1967.

[62] Masud Mansuripur. *Field, Force, Energy and Momentum in Classical Electrodynamics (Revised Edition)*. BENTHAM SCIENCE PUBLISHERS, August 2017.

[63] Emil Wolf. *Introduction to the Theory of Coherence and Polarization of Light*. Cambridge U. Press, oct 2007.

[64] Herbert S. Bennett and Edward A. Stern. Faraday Effect in Solids. *Physical Review*, 137(2A):A448–A461, January 1965.

[65] Harvey Ellio Francis Arthur Jenkins. *Fundamentals of Optics, 4th edition*. McGraw-Hill College, 1976.

[66] Ondřej Slezák, Ryo Yasuhara, Antonio Lucianetti, and Tomáš Mocek. Temperature-wavelength dependence of terbium gallium garnet ceramics Verdet constant. *Optical Materials Express*, 6(11):3683–3691, November 2016. Publisher: Optical Society of America.

[67] Paul A. Williams, A. H. Rose, G. W. Day, T. E. Milner, and M. N. Deeter. Temperature dependence of the Verdet constant in several diamagnetic glasses. *Applied Optics*, 30(10):1176–1178, April 1991. Publisher: Optical Society of America.

[68] K. Turvey. Determination of Verdet constant from combined ac and dc measurements. *Review of Scientific Instruments*, 64(6):1561–1568, June 1993. Publisher: American Institute of Physics.

[69] E. L. de Souza, H. Boudinov, and R. R. B. Correia. Multiple position sensitive photodetector for optical differential detection. *Sensors and Actuators A: Physical*, 195:56–59, June 2013.

[70] Newport. Model 2007 & 2017 User's Manual Nirvana Auto-Balanced Photoreceivers.

[71] P.S. Pershan. Magneto-Optical Effects. *Journal of Applied Physics*, 38(3), 1967.

[72] A. B. Villaverde, D. A. Donatti, and D. G. Bozinis. Terbium gallium garnet Verdet constant measurements with pulsed magnetic field. *Journal of Physics C: Solid State Physics*, 11(12):L495–L498, June 1978. Publisher: IOP Publishing.

[73] Masoud Mollaee, Xiushan Zhu, Shelbi Jenkins, Elena Zong, Jie andTemyanko, Robert Norwood, Arturo Chavez-Pirson, Li Michael, David Zelmon, and N. Peyghambarian. Magneto-optical properties of highly dy^{+3}doped multi-component glasses. *Optics Express*, 28(8), 2020.

[74] N. G. Pavlopoulos, K. S. Kang, L. N. Holmen, N. P. Lyons, F. Akhoundi, K. J. Carothers, S. L. Jenkins, T. Lee, T. M. Kochenderfer, A. Phan, D. Phan, M. E. Mackay, I. B. Shim, K. Char, N. Peyghambarian, L. J. LaComb, R. A. Norwood, and J. Pyun. Polymer and magnetic nanoparticle composites with tunable magneto-optical activity: role of nanoparticle dispersion for high verdet constant materials. *Journal of Materials Chemistry C*, 8(16):5417–5425, April 2020. Publisher: The Royal Society of Chemistry.

[75] Kyle J. Carothers, Nicholas P. Lyons, Nicholas G. Pavlopoulos, Kyung-Seok Kang, Tobias M. Kochenderfer, Anthony Phan, Lindsey N. Holmen, Shelbi L. Jenkins, In-Bo Shim, Robert A. Norwood, and Jeffrey Pyun. Polymer-Coated Magnetic Nanoparticles as Ultrahigh Verdet Constant Materials: Correlation of Nanoparticle Size with Magnetic and Magneto-Optical Properties. *Chemistry of Materials*, June 2021. Publisher: American Chemical Society.

[76] Ferry Iskandar. Nanoparticle processing for optical applications – A review. *Advanced Powder Technology*, 20(4):283–292, July 2009.

[77] P. C. Fannin, A. Slawska-Waniewska, P. Didukh, A. T. Giannitsis, and S. W. Charles. Dynamic properties of a system of cobalt nanoparticles. *The European Physical Journal - Applied Physics*, 17(1):3–9, January 2002. Publisher: EDP Sciences.

[78] M. Z. Ahsan, F. A. Khan, and M. A. Islam. Frequency and Temperature Dependent Dielectric and Magnetic Properties of Manganese Doped Cobalt Ferrite Nanoparticles. *Journal of Electronic Materials*, 48(12):7721–7729, December 2019.

[79] T Reed, G Mashanovich, Y Gardes, and J Thomson. Silicon optical modulators. *nature photonics*, 4:10, 2010.

[80] Yong Zhao, Yong Zhang, Hai-feng Hu, Yang Yang, Ming Lei, and Shu-na Wang. High-sensitive Mach-Zehnder interferometers based on no-core optical fiber with large lateral offset. *Sensors and Actuators A: Physical*, 281:9–14, October 2018.

[81] Delphine Marris-Morini, Xavier Le Roux, Daniel Pascal, Laurent Vivien, Eric Cassan, Jean Marc Fédéli, Jean François Damlencourt, David Bouville, José Palomo, and Suzanne Laval. High speed all-silicon optical modulator. *Journal of Luminescence*, 121(2):387–390, December 2006.

[82] H. Yu, M. Pantouvaki, J. Van Campenhout, K. Komorowska, P. Dumon, P. Verheyen, G. Lepage, P. Absil, D. Korn, D. Hillerkuss, J. Leuthold, R. Baets, and W. Bogaerts. Silicon carrier-depletion-based Mach-Zehnder and ring modulators with different doping patterns for telecommunication and optical interconnect. In *2012 14th International Conference on Transparent Optical Networks (ICTON)*, pages 1–5, July 2012. ISSN: 2161-2064.

[83] Richard A. Soref and Brian R. Bennett. Electrooptical effects in silicon. *IEEE Journal of Quantum Electronics*, 23:123–129, January 1987.

[84] M. Nedeljkovic, R. Soref, and G. Mashanovich. Free-carrier electrorefraction and electroabsorption modulation predictions for silicon over the 1–14-μm infrared wavelength range. *IEEE Photonics Journal*, 3, 2011.

[85] Andrew P. Knights Graham T. Reed. *Silicon Photonics An Introduction*. John Wiley Sons, 2004.

[86] F. Y. Gardes, G. T. Reed, N. G. Emerson, and C. E. Png. A sub-micron depletion-type photonic modulator in Silicon On Insulator. *Optics Express*, 13(22):8845–8854, October 2005. Publisher: Optical Society of America.

[87] Jialei Liu, Guangming Xu, Fenggang Liu, Iwan Kityk, Xinhou Liu, and Zhen Zhen. Recent advances in polymer electro-optic modulators. *RSC Advances*, 5(21):15784–15794, 2015.

[88] Qianfan Xu, Bradley Schmidt, Sameer Pradhan, and Michal Lipson. Micrometre-scale silicon electro-optic modulator. *Nature*, 435(7040):325–327, May 2005. Bandiera_abtest: a Cg_type: Nature Research Journals Number: 7040 Primary_atype: Research Publisher: Nature Publishing Group.

[89] E. L. Wooten, K. M. Kissa, A. Yi-Yan, E. J. Murphy, D. A. Lafaw, P. F. Hallemeier, D. Maack, D. V. Attanasio, D. J. Fritz, G. J. McBrien, and D. E. Bossi. A review of lithium niobate modulators for fiber-optic communications systems. *IEEE Journal of Selected Topics in Quantum Electronics*, 6(1):69–82, January 2000. Conference Name: IEEE Journal of Selected Topics in Quantum Electronics.

[90] Christopher T. Phare, Yoon-Ho Daniel Lee, Jaime Cardenas, and Michal Lipson. Graphene electro-optic modulator with 30 GHz bandwidth. *Nature Photonics*, 9(8):511–514, August 2015. Number: 8 Publisher: Nature Publishing Group.

[91] Ansheng Liu, Richard Jones, Ling Liao, Dean Samara-Rubio, Doron Rubin, Oded Cohen, Remus Nicolaescu, and Mario Paniccia. A high-speed silicon optical modulator based on a metal–oxide–semiconductor capacitor. *Nature*,

427(6975):615–618, February 2004. Number: 6975 Publisher: Nature Publishing Group.

[92] Shelbi L. Jenkins, Sasaan A. Showghi, and Robert A. Norwood. Magneto-optic modulator fabricated using polymer-coated magnetic nanoparticles with 4.75db extinction ratio. OSA Advanced Photonics Congress - Novel Optical Materials and Applications (NOMA), Qubec, Canada, 2021. OSA.

[93] N. Balakrishna and Chin Diew Lai. Univariate Distributions. In Chin Diew Lai and N. Balakrishnan, editors, *Continuous Bivariate Distributions: Second Edition*, pages 1–32. Springer, New York, NY, 2009.

[94] Martin Monteiro. The polarization of light and malus' law using smartphones. *The Physics Teacher*, 55(5), 2017.

[95] Mit - visualizing e&m. `https://web.mit.edu/viz/EM/visualizations/notes/`.

Index